ADVANCED ENERGY MATERIALS
www.advenergymat.de

Well-Defined Nanostructures for Electrochemical Energy Conversion and Storage

Rui Xu, Lei Du, David Adekoya, Gaixia Zhang, Shanqing Zhang, Shuhui Sun,* and Yong Lei**

Electrochemical energy conversion and storage play crucial roles in meeting the increasing demand for renewable, portable, and affordable power supplies for society. The rapid development of nanostructured materials provides an alternative route by virtue of their unique and promising effects emerging at nanoscale. In addition to finding advanced materials, structure design and engineering of electrodes improves the electrochemical performance and the resultant commercial competitivity. Regarding the structural engineering, controlling the geometrical parameters (i.e., size, shape, hetero-architecture, and spatial arrangement) of nanostructures and thus forming well-defined nanostructure (WDN) electrodes have been the central aspects of investigations and practical applications. This review discusses the fundamental aspects and concept of WDNs for energy conversion and storage, with a strong emphasis on illuminating the relationship between the structural characteristics and the resultant electrochemical superiorities. Key strategies for actualizing well-defined features in nanostructures are summarized. Electrocatalysis and photoelectrocatalysis (for energy conversion) as well as metal-ion batteries and supercapacitors (for energy storage) are selected to illustrate the superiorities of WDNs in electrochemical reactions and charge carrier transportation. Finally, conclusions and perspectives regarding future research, development, and applications of WDNs are discussed.

1. Introduction

Utilizing renewable energy and remitting traditional fossil fuel-related environmental problems become crucial for realizing a worldwide sustainable energy future.[1] For this purpose, electrochemical conversion and storage technologies for so-called "clean energy" (e.g., fuel cells, electrolyzers, photoelectrolyzers, metal–air batteries, metal-ion batteries, and supercapacitors) have been playing central roles.[2,3] In order to compete with existing energy supply systems mainly based on fossil fuels, the performance of the clean energy (conversion and storage) devices/systems has to be significantly improved. The electrochemical energy conversion and storage usually involves many intricate chemical reactions and physical interactions at the surface and inside of electrodes/electrolytes, and the kinetics and transport behaviors of different carriers (e.g., electrons, holes, ions, molecules) are closely associated with the materials selected for electrodes as well as the structures of electrodes. To this point, material design and structure design for electrodes have been the research focuses for improving the electrochemical performance of energy conversion and storage, which both have gained high attention from academia and industry.

Along with researches for finding advanced electrode materials, much recent research efforts have been made for electrode structure design and engineering, especially when traditional macro-scale structured electrodes are showing limitations of achieving satisfying performance for energy conversion and storage. Among these efforts, electrode nanostructuring has been demonstrated as a promising way for realizing high-performance electrochemical energy conversion and storage, which attributes the distinct features of nanostructured materials differing from their bulk material counterparts. The high surface-to-volume ratios of nanostructures give large electrochemical surface areas with much more exposed atoms and hence improve the performance per unit electrode area and/or

Dr. R. Xu, Prof. Y. Lei
Fachgebiet Angewandte Nanophysik
Institut für Physik & IMN MacroNano
Technische Universität Ilmenau
Ilmenau 98693, Germany
E-mail: yong.lei@tu-ilmenau.de

The ORCID identification number(s) for the author(s) of this article can be found under https://doi.org/10.1002/aenm.202001537.

DOI: 10.1002/aenm.202001537

Dr. L. Du, Dr. G. Zhang, Prof. S. Sun
Institut National de la Recherche Scientifique-Énergie
Matériaux et Télécommunications
Varennes QC J3 X 1S2, Canada
E-mail: shuhui@emt.inrs.ca

Dr. D. Adekoya, Prof. S. Zhang
Centre for Clean Environment and Energy
Environmental Futures Research Institute
School of Environment and Science
Griffith University
Gold Coast, Queensland 4222, Australia
E-mail: s.zhang@griffith.edu.au

material mass. Besides, the nanostructured electrode can provide fast and much-shortened transportation pathways of carriers and facilitate the electrochemical reaction kinetics.

In the researches of using nanostructures for energy conversion and storage, controlling four important structural parameters of electrodes have been the central aspects of investigations: size and shape of nanostructures, hetero-architectures by combining different nano-units, and spatial arrangements of arrayed nano-units. A high level of controllability of size and shape provides capabilities of property tuning such as altering band gap, guiding carrier transportation, and modulating chemical potential. Obtaining hetero-architectures and adjusting spatial arrangements of nano-units can facilitate performance optimization by achieving combined functions of multiple nano-units, directional transportations of carriers in electrode and electrolyte, and nanoconfinement effect. Therefore, realizing well-defined nanostructures (WDNs) with high controlling of these four geometric parameters shall be the key for fully understanding the electrochemical processes of energy conversion and storage, and hence for modulating these processes to optimize the device performance.

In recent years, intensive investigations have been made for the WDNs, and a large number of WDNs were fabricated and have been widely applied as electrodes for different types of energy conversion and storage devices, especially for promoting the performance of energy conversion and storage. There have been excellent reviews discussing the advances of nanomaterials or nanostructures in energy applications,[4–10] but few of them touched the topic of WDNs. Therefore, a comprehensive review of WDNs for energy conversion and storage is urgent and timely. In Section 2 of this review, the fundamental aspects of WDNs are given and their superiorities for energy conversion and storage are demonstrated in detail. In Section 3, we review the critical progresses of the controllable fabrications of WDNs. In Sections 4 and 5, we identify how the WDNs benefit electrocatalysis and photoelectrocatalysis devices, as well as batteries and supercapacitors, which are the two mainstreams of clean energy applications (conversion and storage). Finally, we provide our conclusion and perspectives on future research and development of WDNs for energy conversion and storage.

2. Fundamentals of Well-Defined Nanostructures and Their Superiorities in Electrochemical Energy Conversion and Storage

2.1. Fundamentals of WDNs

Despite tremendous decent achievements in the fields of electrochemical energy conversion and storage, reaching device performance idealized for industrial applications is still a long way off, primarily due to the lack of appropriate material and structure systems. It is well known that the chemical and physical property of a nanostructure is predominantly determined by its composition and dimension. Rather than by searching for a brand-new composition, modulating chemical and physical property by changing structural dimension is attracting more and more attention with the development of nano-science

(Eddie) Shanqing Zhang obtained his Ph.D. in 2001 at Griffith University, Australia. Basing on functional nanomaterials, he has invented and developed a series of nanotechnologies for energy conversion and storage. He was awarded the Australia Research Council Future Fellowship for 2009–2013 and promoted as a full professor and theme leader of energy storage at the Centre for Clean Environment and Energy, Griffith University. Currently, His research focuses on the design of nanomaterials and functional polymers for energy conversion and storage devices, including lithium-ion, sodium-ion, and potassium-ion batteries, and supercapacitors.

Shuhui Sun is a full professor at the Institut National de la Recherche Scientifique (INRS), Center for Energy, Materials, and Telecommunications, Canada. His current research interests focus on multifunctional nanomaterials for energy conversion and storage applications, including PEM fuel cells (low-Pt and non-noble metal catalysts), metal-ion (Li^+, Na^+, Zn^{2+}) batteries, rechargeable Zn–air batteries, and flexible all-solid-state metal–air batteries. He is also interested in the nanostructured photo- and electro-catalysts for H_2 production, CO_2 reduction, and water treatment.

Yong Lei is a Professor at the Technical University of Ilmenau in Germany. He received his Ph.D. from the Chinese Academy of Sciences in 2001. He worked at the Karlsruhe Institute of Technology as an Alexander von Humboldt Fellow and the University of Muenster as a junior professor. In 2011, he joined the Technical University of Ilmenau as a chair professor and leader of the group of applied nano-physics. His research focuses on template-based nanostructures and their energy-related and optoelectronic applications.

and nanotechnology. Excitingly, as the feature size and/or dimension of a material downsizing and approaching nanometer-sized scale (i.e., nanostructured material), the intrinsic properties (e.g., electrical conductivity, catalytic activity, electromagnetic absorption and scattering, wettability) of the material turn out to be obviously changed relative to those of its bulk equivalent. To date, nanostructures have obtained a great deal of prominence in the applications of electrochemical energy conversion and storage due to their tunable chemical and physical characteristics and hence achieving improved performance.

Nanostructures can be generally termed as a family of matters featured by at least one or more dimensions within a size range of 1–1000 nm. So far, large amounts of nanostructures have been fabricated that are principally classified into four categories as 0D, 1D, 2D, and 3D nanostructures (schematically illustrated in **Figure 1**a), all of which could have structure-induced diversities of basic properties. Taking the electron movability as an example, electrons could be immobilized in a dimensionless space for a 0D nanostructure, while it becomes movable along the axis within a 1D nanostructure. Likewise, electrons in 2D and 3D nanostructures can move in a plane or a space, respectively. The surface-to-volume ratios of nanostructures are increased with the size decreasing (Figure 1b, by taking 1D nanostructure as an example), and relatively more atoms (and/or molecules) are thus exposed on the structure surface. Due to the interrupt disruption of crystalline lattices, these surface atoms are incompletely bonded, hence providing more freedom of modifying the surface-related material properties. In addition, the geometrical shape variation (Figure 1c) is also capable of exerting significant influence upon the chemical and physical properties of a nanostructure. Notwithstanding the highly expanded property of a nanostructure by adjusting its size and shape, the possibility for property tunability is still limited, especially considering the diverse requirements in a broad variety of practical applications. Hence, two ingenious solutions have been proposed to further widen the tunable scope of chemical and physical properties. The first solution is to combine different distinct nano-units to form hetero-architectures (Figure 1d), such as core/shell, sandwich, multi-segment structures.[11] Note that, each nano-unit of the hetero-architectures could be adjusted independently to complement with other units so that the combined nano-units can work together to achieve new effects and benefits that might be inaccessible by their single counterparts. Moreover, for almost all applications of nanostructures in energy conversion and storage, millions of nanostructures shall be integrated or patterned into a large-scale macroscopic area so as to be used as the electrode of a functional device. Considering this issue, another solution to widen the property tunability of nanostructures is to control the spatial arrangement of the arrayed nanostructures (Figure 1e). A high degree of controlling the spatial arrangement regarding such as the alignment directions and spacing of arrayed nano-units shall be beneficial to using especially the collective inter-unit coupling to enhance the overall performance of the nanostructure ensemble for energy conversion and storage.

To make nanostructures fully qualified as excellent electrodes for energy conversion and storage and hence satisfying the industry-standard requirements of device applications, it shall be mandatory for realizing WDNs, namely nanostructures with

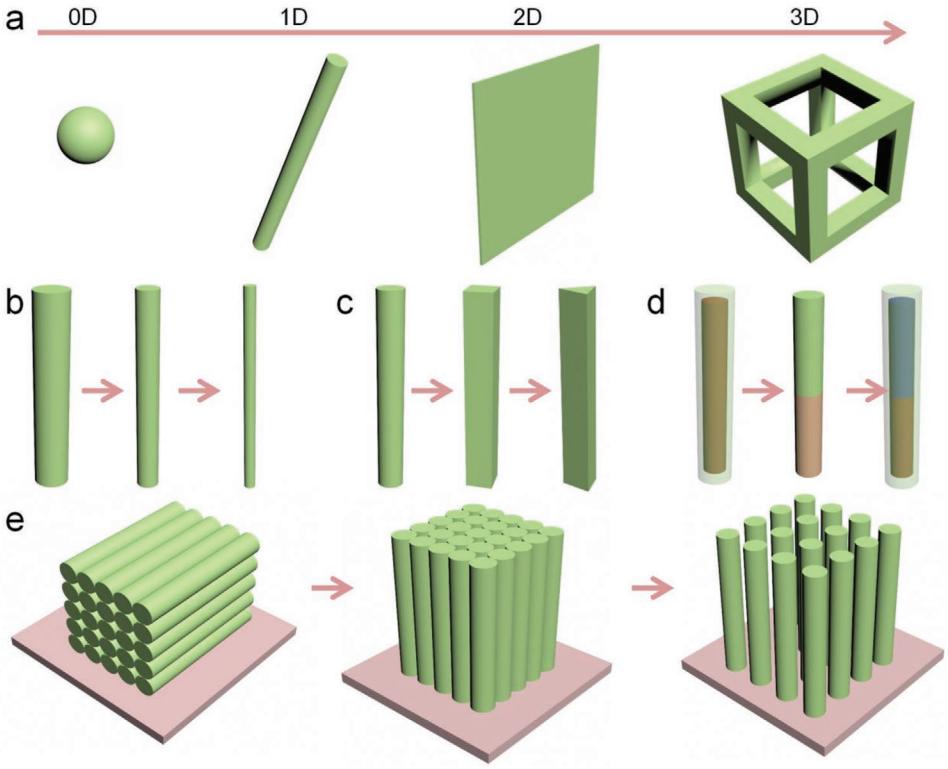

Figure 1. a) Schematic nanostructures with different dimensions: 0D–3D. Representative 1D nanostructures with different b) sizes, c) shapes, and d) hetero-architectures, and e) their spatial arrangements (alignment directions and spacing).

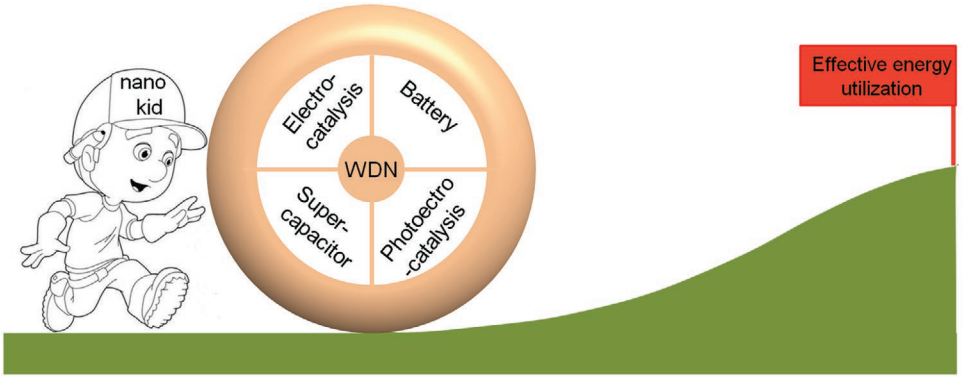

Figure 2. Schematic illustration of effective energy utilization using WDN-based electrocatalysis, photoelectrocatalysis, battery, and supercapacitor.

precisely controllable geometries of the above-mentioned four key structural parameters: size and shape of nanostructures, hetero-architectures by combining different nano-units, as well as spatial arrangements of arrayed nano-units as an ensemble. By achieving such WDNs with complete aspects of structural controllability, comprehensive understanding of the intricate electrochemical processes involved in the energy conversion and storage, and hence to modulate these processes becomes feasible, which could provide a versatile platform for optimizing the performance of electrochemical energy conversion and storage.

2.2. Superiorities of WDNs in Electrochemical Energy Conversion and Storage

By virtue of the highly controllable structures and hence the tunable chemical and physical property, WDN-integrated devices have shown high promise in boosting electrochemical energy conversion and storage. To exploit the capability of WDNs to the full for property tuning, it is imperative to investigate in detail the microscopic operation involved in electrochemical reaction, especially to gain an in-depth understanding of the relation of the electrochemical microscopic operation and reaction to the nanoscale features of WDN electrodes.

Currently, there are diverse systems concerning electrochemical energy conversion and storage, such as electrocatalysis and photoelectrocatalysis for energy conversion, and supercapacitors and batteries for energy conversion (**Figure 2**). Although these systems differ from one another, they do share some common fundamental physical and chemical processes. Given that photoelectrocatalytic water splitting covers many fundamental operations of carriers including photon absorption, electron/hole/ion/molecule transportation, and chemical reaction, while only some of these operations are involved in other systems, herein we select photoelectrocatalytic water splitting as an example to illustrate the cycle of carriers in an electrochemical reaction. As portrayed in **Figure 3**, the cycle of carriers in photoelectrocatalytic water splitting typically includes five procedures: i) incident light propogates and is absorbed by the electrode, and generating electron–hole pairs; ii) photo-induced pairs are separated rapidly, and electrons and holes migrate to the surface of photocathode and photoanode, respectively; iii) carriers (i.e., H^+, OH^-, gas molecules) diffuse/drift in the electrolyte; iv) chemical reactions between carriers at the electrode/electrolyte interface; v) charge carriers (holes and electrons) drift to the conductive substrate of photocathode and photoanode, respectively. These procedures can be roughly divided into two aspects: carrier transportation (e.g., procedures i, ii, iii, v) and chemical reaction (e.g., procedures i and iv). It is predictable

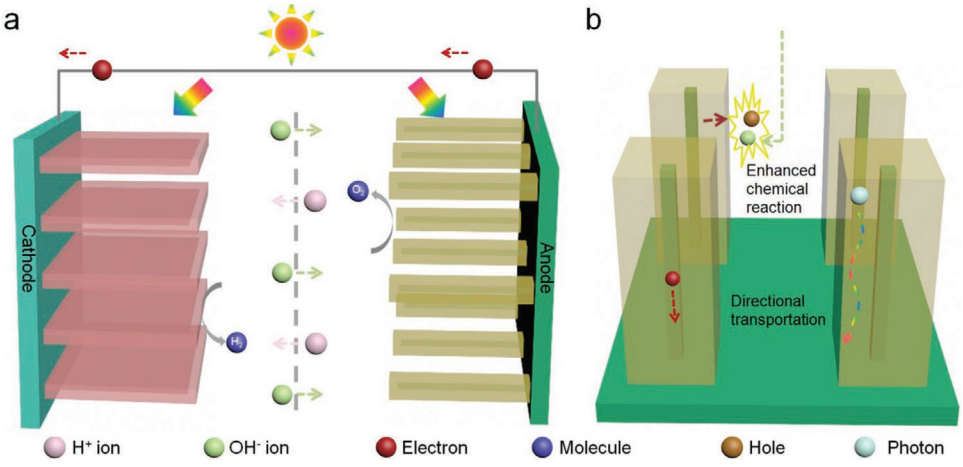

Figure 3. a) Schematic illustration of photoelectrocatalytic water splitting using WDN electrodes. b) WDN photoanode with advantageous characteristics.

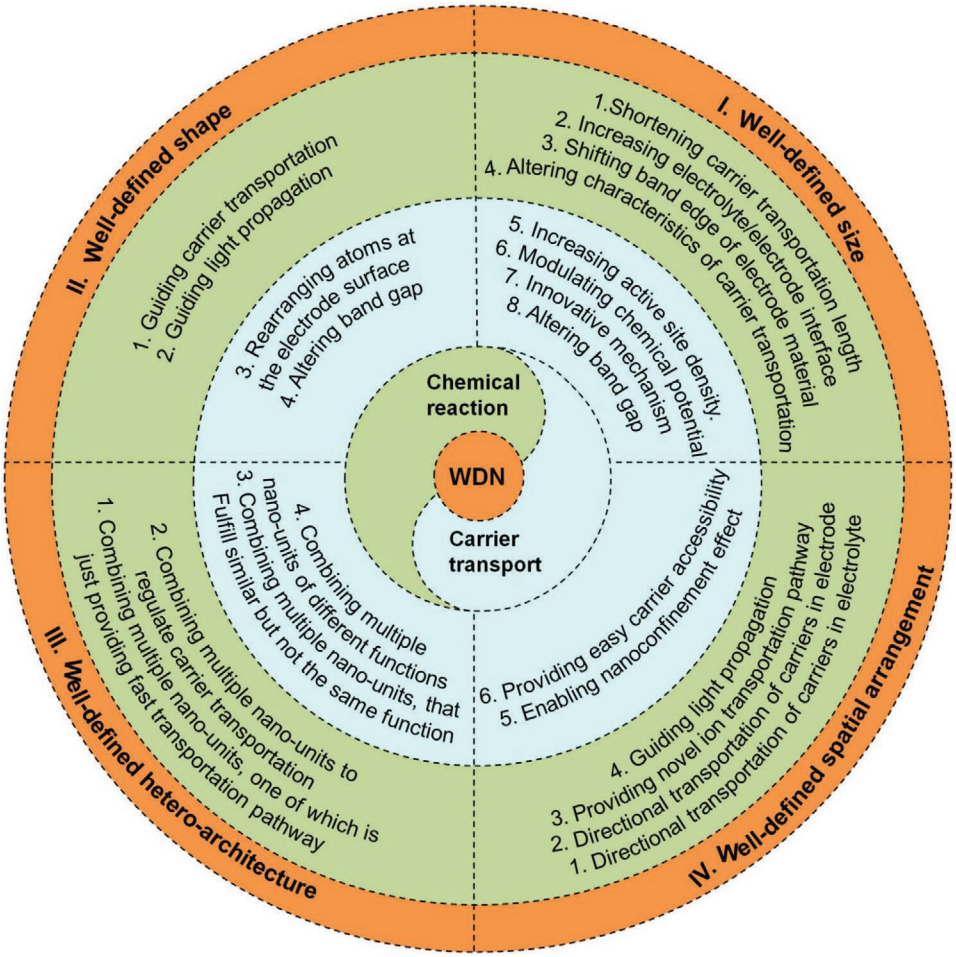

Figure 4. Superiorities of WDNs with tunable geometries (size, shape, hetero-architecture, spatial arrangement) in reducing the resistance of carrier transportation and chemical reaction for electrochemical energy conversion and storage.

that suppressing (no matter partly or totally) the resistances of carrier transportation and chemical reaction will decrease the kinetic limitation for electrochemical energy conversion and storage.

As compared with energy conversion and storage devices using conventional bulk materials, WDN-based counterparts draw great attention due to their advantageous physical and chemical properties, especially the capability to reduce the kinetic limitation that determines the value of WDNs in improving energy conversion and storage. In this regard, **Figure 4** summarizes superiorities of WDNs with highly tunable geometries (size, shape, hetero-architecture, and spatial arrangement) in reducing the resistance of carrier transportation and chemical reaction, as detailed as follows.

2.2.1. Superiority of Tunable Size of WDN Unit

For Carrier Transportation:

1) Shortening carrier transportation length in electrode. Given that the diffusion time of a carrier (e.g., ion and electron) in nanostructures can be described by $t = L^2/2D$, where L is the feature size of nanostructure and D the diffusion constant for carries, smaller size will significantly reduce the transportation time and resistance in the electrode.[12,13]
2) Increasing electrolyte/electrode interface. Taking a nanocube electrode as an example, cutting the side length into n segments will result in the amplification of the overall surface area by a factor of n. Therefore, large surfaces of electrodes are in favor of carrier exchange between the electrode and the electrolyte.
3) Shifting band edge of electrode material. Downsizing nanostructures tends to shift conduction band to be more reducing and valence band to be more oxidizing,[14] which is expected to benefit the separation of photogenerated electron–hole pairs in electrode as well as to fasten charge carrier exchange at the electrode/electrolyte interface. Tuning electronic structure provides another benefit for electrocatalysis, that is, the well-modulated adsorption strength of carriers. Very weak adsorption will result in serious difficulty of reaction because of inadequate adsorption of active reactants. On the other hand, when the adsorption is too strong, the adsorbed product is difficult to remove which will occupy the active sites and hinder the following reactions. Therefore, an optimized adsorption strength of carriers realized by tuning electronic structure is highly important.
4) Altering characteristics of carrier transportation in electrode (e.g., electrical conductivity, recombination lifetime,

diffusion length). For example, nanostructures of smaller sizes demonstrate decreased electrical conductivity due to elastic scattering of electrons with more grain boundaries.[15,16] Another representative example is the size-dependent Auger recombination in ZnO nanocrystal that shrinking in size can accelerate Auger recombination and dramatically decrease electron–hole lifetime from over 1 ns to about 80 ps.[17]

For Chemical Reaction:

5) Increasing active site density. Decreasing nanostructure size results in a relatively larger surface-to-volume ratio, and hence more atoms are exposed to the ambiance with more dangling bonds. These unsaturated bonds provide a large amount of active sites to promote chemical reaction extensively and rapidly.
6) Modulating chemical potential. Tuning dimensions of a structure to nanometer-sized range could be used to modify chemical potentials for charge carriers which leads to alteration of thermodynamics and facilitates the chemical reaction.[18,19]
7) Innovative mechanism for energy conversion and storage. For example, besides enhancing light absorption by generating more electron–hole pairs within a semiconductor electrode, hot electrons arising from plasmonic resonance can facilitate decomposition of water molecules, which offers an alternative way for promoting solar energy conversion.[20] Different from the classical mechanism (e.g., ion insertion/deinsertion or alloying), the formation and decomposition of Li_2O as well as the reduction and oxidation of metal nanoparticles can give rise to reliable long-term operation and superior capacity in battery electrode of transition-metal oxide nanoparticles.[21]
8) Altering band gap for light absorption. When the feature size of a nanostructure decreases to approach the range of Bohr radius, quantum confinement effect takes place, leading to an obvious variation of the band gap value.[22] For example, the band gap of Ge is alterable from about 0.7 eV to more than 2 eV by reducing the size to 2–3 nm. This phenomenon is also applicable to many other materials such as oxides,[23] selenides,[24] and sulfide.[25]

2.2.2. Superiority of Tunable Shape of WDN Unit

For Carrier Transport:

1) Enhancing local electric fields to guide carrier transportation. Electric simulation demonstrates that a metallic nanometer-sized tip could provide tenfold higher electric field compared with that of its quasi-planer counterpart. The locally strong electric fields lead to locally high concentrations of ions and resultant reactant (e.g., CO_2) surrounding the active sites of the catalytic electrode surface. Consequently, the problem of slow kinetics during electrochemical reduction, arising from the low ionic concentration in the electrolyte, can be addressed.[26]
2) Guiding light propagation. Engineering nanostructure shape results in alteration of light trapping capability by introducing distinctive optical effects such as scattering, reflection, and plasmonic resonance.[27,28] For instance, computational simulation reveals that the light absorption of silicon solar cells can be altered by engineering the shape of nanostructures on the front surface. The absorption efficiencies of cone, hexangular pyramid, rectangular pyramid, and triangular pyramid should increase in sequence.[29]

For Chemical Reaction:

3) Rearranging atoms at the electrode surface. For example, Huang et al. observed that directional exposure of crystallographic plane (e.g., high-index facets) of the electrode through the shape regulation of tetrahexahedral particles (e.g., Pt, Pd, Rh, Ni, Co, and their combination) led to dramatically enhanced electro-oxidation of formic acid and accordingly the current density at a fixed potential can be increased by a factor of 20.[30]
4) Altering band gap of electrode for light absorption. In addition to the nanostructure size, the shape may play roles in determining the electrode's band gap as well because of the inhomogeneous distribution of electronic state over the entire surface.[24,31]

2.2.3. Superiority of Tunable Hetero-Architecture of WDN Unit

For Carrier Transport:

1) Combining multiple nano-units, one of which is just providing fast transportation pathways. For example, for core–shell hetero-architecture nanowires, the inner cores act directly as a current collector that is connected to the outer shells of active material, providing a fast and much shorter transportation pathway of carriers and hence alleviate the ohmic potential loss that usually exists in the conventional design of planar electrode/current collector connection.
2) Combining multiple nano-units to regulate carrier transportation. For instance, engineering band bending of electrode materials by forming heterojunctions (e.g., P-N junction, Schottky junction) is able to regulate directional transportation pathways and navigate charge carriers in the electrode.

For Chemical Reaction:

3) Combining multiple nano-units that fulfill similar but not the same function. In other words, each nano-unit is capable of completing electrochemical energy conversion and storage independently without additional assistance, and different nano-units complement one another to enhance the overall performance. For example, multiple photocatalysts with different band gaps can be integrated into hetero-architectures to extend the light absorption spectrum.
4) Combining multiple nano-units with different functions. To be specific, one nano-unit dominates over the electrochemical reaction, and others play auxiliary roles to enhance the ultimate performance, rather than participating into the chemical reaction directly. To name a few, both coating a passivation layer over the electrode surface to reduce surface recombination and depositing electrocatalysts to reduce the kinetic limitation in chemical reaction are reliable ways for promotion of photoelectrocatalytic water splitting.

2.2.4. Superiority of Tunable Spatial Arrangement of WDN Ensemble

For Carrier Transport:

1) Directional transportation of carriers in electrolyte. Interval space defined by regular nanostructure arrays provides a directional channel which facilitates carrier transportation from the electrolyte to reach the electrode surface, and vice versa.

2) Directional transportation of carriers in electrode. A directional pathway from the active site of electrode surface to the inner conductive substrate regulated by arrayed nanostructures of electrode could be built for swift carrier transportation.
3) Providing novel ion transportation pathway. For example, the establishment of inter-digital nanostructure electrodes may suppress the ohmic potential loss in conventional planar electrode batteries with long-distance ion transportation.
4) Guiding light propagation. As light is impinging upon WDNs that are periodically arranged on the order of the light wavelength, light propagation pathways can be spatially modulated due to optical diffraction effect, consequently leading to extra light harvesting.[32,33]

For Chemical Reaction:

5) Enabling nano-confinement effect. Nano-cavities between neighboring nanostructures and/or hollow nano-space provide unique confined spatial environments for carriers, which lead to enhanced interaction between carriers and electrode surface and thus are desirable for sufficient chemical reaction.[34]
6) Providing easy carrier accessibility. Uniform channels established by regularly arranged WDNs offer easy electrolyte accessibility for the electrode and fasten carrier exchange at the electrolyte/electrode interface, which is helpful for making a full usage of active sites at the electrode surface in chemical reaction.

It is concluded that WDN electrodes can promote electrochemical energy conversion and storage by directionally guiding carrier transportation as well as facilitating chemical reactions that are reaped from well-defined geometries. Notably, the utilization of WDNs also gain access to other advantages, for example, enhancing long-term operational stability because the interval space between neighboring arrayed nanostructures can serve as a buffer zone to accommodate mechanical strain arising from volume expansion and contraction during ion-insertion/deinsertion or temperature variation.

3. Fabrication of Well-Defined Nanostructures

As introduced in Section 2, WDNs are capable of serving as functional electrodes to promote energy conversion and storage efficiency by regulating the carrier transportation and the chemical reactions, and the overall device performance can be extensively tuned and optimized by adjusting the geometries of WDNs (i.e., size, shape, hetero-architecture, and spatial arrangement). For actualizing well-defined geometries into nanostructures, seven important techniques have been pursued including: I) photo/particle based lithography, II) scanning probe lithography, III) nanoimprinting lithography, IV) self-assembly, V) solution-phase deposition, VI) vapor-phase deposition, and VII) template-mediated growth. Techniques I–VI are schematically illustrated in **Figure 5**, while technique VII is shown in **Figure 6**. In this section, we will detail these techniques point-by-point.

3.1. Photo/Particle-Based Lithography

The exposure for lithography has two typical approaches: using photons and particles. Regarding the lithography using photons (i.e., photolithography), various kinds of electromagnetic radiation such as ultraviolet, deep ultraviolet, extreme ultraviolet, and X-ray are exploited. Subsequently, the desired patterns decorated on a photomask are transferred onto a layer of photoresist chemicals by altering the molecular structures and subsequently the underlying substrate aided by diverse etching techniques. Also, particles such as electrons and ions are capable of changing the molecular structures of the resist chemicals to fulfill nanostructuring upon the target materials.

3.1.1. Lithography Using Photons

With the requirement of device miniaturization, especially for the integrated circuits in the semiconductor industry, many photolithographic techniques have been developed during the past several decades. The primary mission of photolithography is copying a specific pattern of a photomask onto a photoresist chemical layer and, subsequently, a substrate with the help of diverse etching techniques. According to the chemical reaction of the photoresist under radiation, the photolithographic techniques can be classified into positive and negative lithography. Taking the positive one as an example, Figure 5a details the pattern transferring process, typically involving six sequential steps: 1) the target substrate is coated by a thin layer of photoresist chemical; 2) the substrate is partially exposed to electromagnetic radiation with the presence of a photomask located between the substrate and the radiation source; 3) the molecular structures of the photoresist chemicals at the exposure area are changed, which consequently results in an alteration of the solubility of the exposed chemicals relative to that without exposure; 4) after completing exposure, the denatured photoresist chemicals are selectively dissolved by immersing into a solvent; 5) upon the bare area of the substrate, etching (e.g., wet-chemical etching or dry etching) is performed, successfully transferring the pattern of the photomask onto the surface of substrate; 6) the substrate is finally dipped into a solution and the remaining photoresist chemicals are completely dissolved away. Almost all photolithographic techniques share this fundamental operation cycle. In practical production such as some complex patterns, the whole fabrication process may go through many photolithographic cycles. With this technique, the as-obtained patterns can be downsized into a few tens of nanometers, enabling nanostructures to gain access to well-defined geometries in terms of shape, size, and arrangement. Indeed, photolithography is a powerful and widely adopted method for nanostructure fabrication in a variety of applications, both for basic scientific research and for industrially massive production.[35,36] However, the photolithographic technique is still facing a few challenges. First, the fabrication of the photomask is relatively expensive and time-consuming. Another shortcoming is the harsh requirement for the extreme cleanliness of the operational environment. Furthermore, this technique is effective only for 2D planar substrates, and not suited for nanostructuring upon non-flat 3D ones. Finally, the

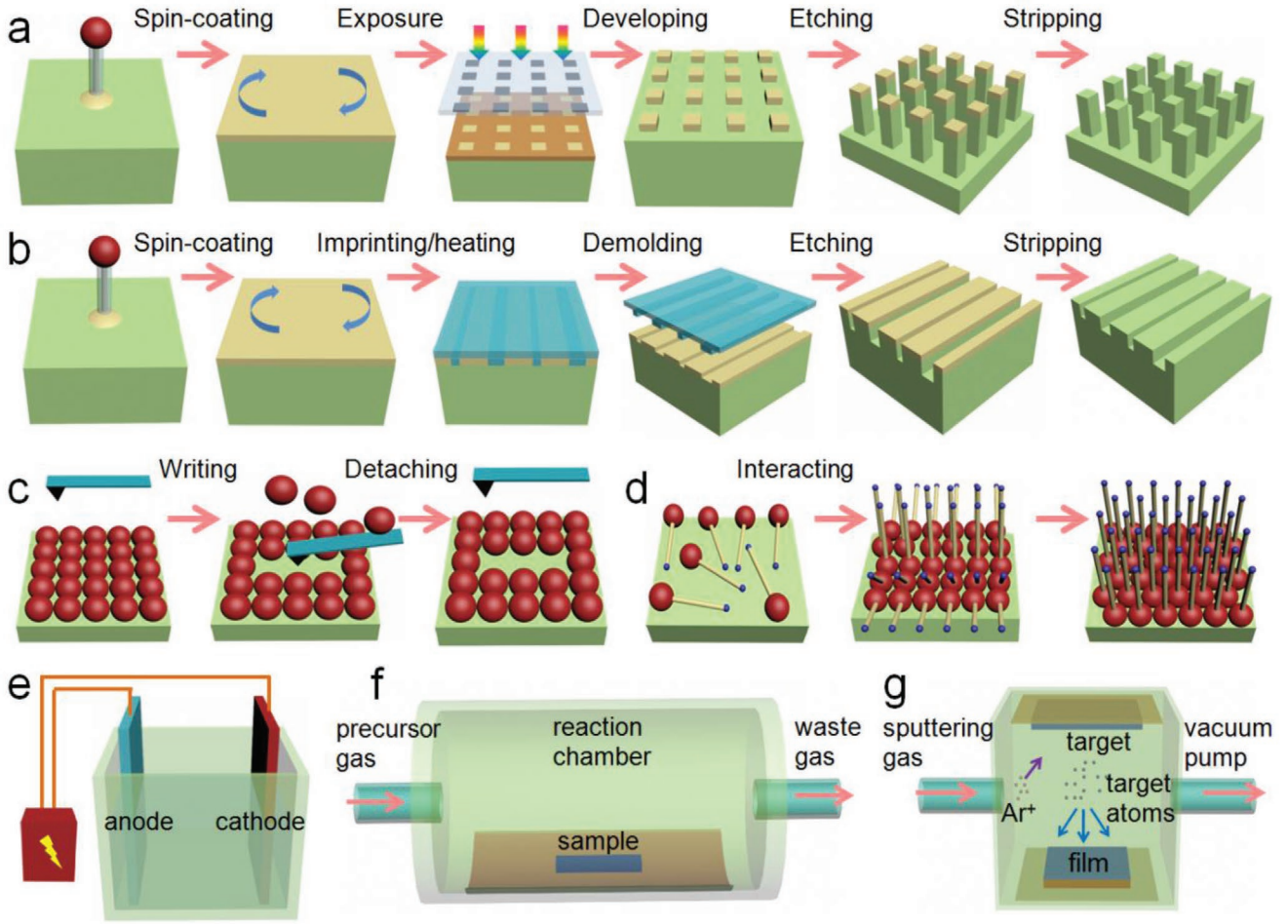

Figure 5. Schematic illustration of WDN fabrication using a) photo/particle-based lithography, b) nanoimprinting lithography, c) scanning probe lithography, d) self-assembly, e) solution-phase (electrochemical) deposition, f) chemical vapor deposition, and g) physical vapor deposition (sputtering).

ultimate challenge of all photolithographic techniques is the limited resolution (i.e., the minimum feature size) due to the physical diffraction limit.

3.1.2. Lithography Using Particles

In addition to photons, energetic electrons and ions can be exploited for denaturing the resist chemicals to construct nanostructures. In light of the short de Broglie wavelengths (i.e., less than 0.1 nm), the physical diffraction effect is significantly suppressed with the utilization of these particles as compared with that in photolithography, which results in enormous decreasing of the minimum feature size and thus is appealing to a lot of high-resolution nanostructure fabrication. For example, lithography based on a focused electron beam (EBL) can construct nanostructures with sub-10 nm resolution.[37] EBL systems focus a beam of electrons and scan it over the surface of a substrate according to a customer-designed route. In principle, nanostructures with arbitrary shapes are obtainable. Besides the high resolution and excellent shape controllability, another advantage of EBL is that nanostructures can be directly written on substrates, leading to maskless lithography. However, EBL is very time-consuming due to the serial operation, greatly limiting its throughput in massive production. For improving the lithographic speed, the scientific community developed an approach in which an array of particle beams is used to perform multiple exposures simultaneously rather than sequentially. In view of the desirable high resolution and excellent shape controllability as well as the disadvantageous low yield, EBL is more adopted to construct small quantity of nanostructures for basic scientific research.[38]

Note that, etching techniques play crucial roles in the lithographic techniques for realizing WDNs. According to whether the etchant is in solution or gas, etching techniques are generally sorted as wet chemical etching and dry etching. Often, wet chemical etching is considered as the first option in view of its low cost and operational simplicity. The wet chemical etching of materials from a substrate can be performed either isotropically or anisotropically. Usually, the majority of wet chemical etching processes are characterized by isotropism. Given that the whole substrate is exposed to the etchant, the materials that are not to be etched should be protected with a protective capping. The isotropic etching in the immersive operation results in a unique characteristic where the as-etched concaves in the monocrystalline substrate present sloped sidewalls. As for polycrystalline

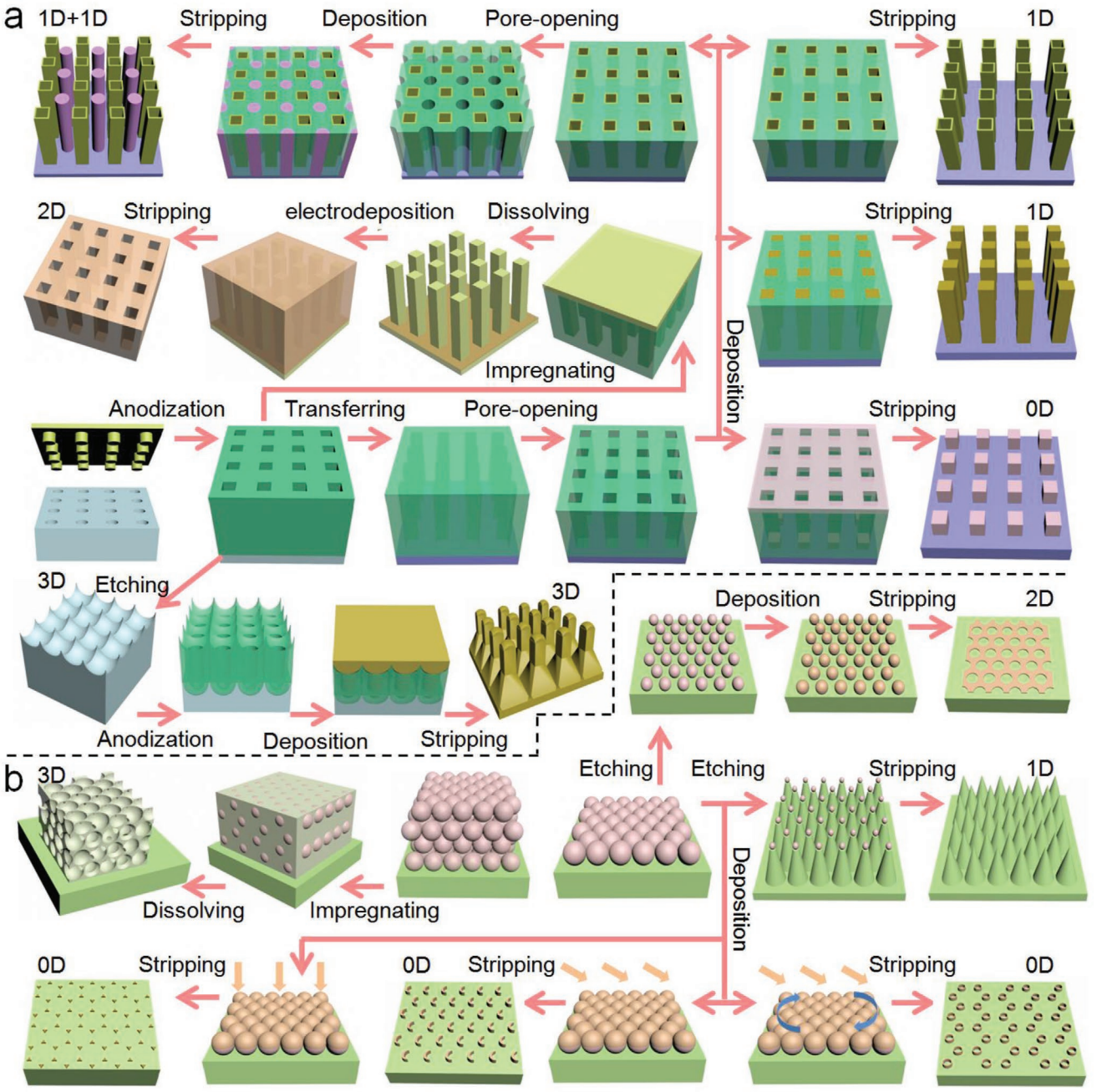

Figure 6. Template-mediated growth. a) Schematic illustration for fabricating 0D nanoparticles, 1D nanowires and nanotubes and their combinations, 2D nanomeshes, 3D nanotowers using AAO templates. b) Schematic process for fabricating 0D nanoparticles, 1D nanowires, 2D nanomeshes, and 3D inverse opals using PS templates.

materials, chemical etching is preferentially carried out at the grain boundaries and crystallographic defects which have been used for engineering metallic surfaces.[39] In addition, wet chemical etching exhibits prominent selectivity between different materials, which leads to operational convenience since chemical reaction will end automatically when the etchant touches another material.[40] Dry etching is a process in which material at specific locations is removed from a substrate by exposing the material to energetic ions normally with the assistance of a mask. Unlike the majority of wet chemical etching techniques, the dry etching techniques exhibit directional and anisotropic etching. Two typical techniques are widely used to perform dry etching: ion beam etching and reactive ion etching. In an ion beam etching process, energetic argon ions are used to strike material out from the substrate surface which is perpendicular or tilted to the ion beam. Because of the perpendicular incidence, the abrasion on vertical walls is minimal, resulting in high anisotropism. Almost all materials can be etched using this method.[41,42] However, the utilization scope of this method is limited due to its low selectivity in materials. Regarding the reactive ion etching, plasma

is generated by an electromagnetic field and then high energy ions from the chemically reactive plasma are used to react with the substrate. The reactive ion etching provides precise etching parameters such as selectivity, etching rate, and uniformity, which can be easily adjusted by modulating the properties of the etching ions. Importantly, both isotropic and anisotropic etching profiles are obtainable in the process of the reactive ion etching which is thus serving as one of the most important etching techniques in device manufacturing.[43,44]

3.2. Scanning Probe Lithography

Scanning probe lithography (SPL) refers to lithographic techniques that exploit the local interaction between a scanning probe and the surface of a substrate to directly deposit or sculpture materials at a local domain.[45] SPL achieves mask-free operation as well and is often exploited as an alternative lithographic technique for basic scientific research (Figure 5c). This technique was first proposed with the invention of scanning probe microscope[46] and has grown rapidly with the development of other analytical facilities: atomic force microscope, scanning electrochemical microscope, and so on. Within these configurations, the locally physical interactions vary from each other and can be generally divided into four types: mechanical, electrical, optical, and thermal.

Due to the fundamentally operational originality, the scanning probe lithography is significantly different from the aforementioned lithographic techniques. For example, the photolithography and EBL are based on far-field operation with the distance between the radiation/electron source and the target pattern far larger than the pattern size. For the sake of the large distance, both techniques have to deal with the physical diffraction limit. Moreover, the long distance also leads to beam diffusion; therefore, more efforts should be taken to optimize beam emission quality and the pathway which inevitably increases facility cost. In stark contrast, the SPL technique is serving in the near-field zone which thus bypass the problems of beam diffusion and diffraction limit and potentially enables ultimately high (e.g., at the atomic scale) resolution.[47] In principle, SPL is capable of gaining arbitrary patterns in spite of the concomitant time-consuming operation.

3.3. Nanoimprinting Lithography

For solving the low-resolution limitation in photolithography as well as the time-consuming problem existing in EBL and SPL, Chou et al. invented the nanoimprinting lithography (NIL) so as to achieve high resolution in a fast and high-throughput way in 1995.[48] Different from traditional lithographic techniques in which patterns are obtained by changing the molecular structures of resist chemicals with photons or particles, NIL depends on mechanical deformation in the resist and thus reaches higher resolution by circumventing the light diffraction effect. Actually, the resolution of NIL is mainly determined by the minimum feature size of the imprinting mold, which is manufacturable with sub-10 nm features over large scales. So far, a lot of NIL techniques have been developed such as thermal NIL (TNIL) and UV-based NIL (UVNIL).[49]

Figure 5b depicts the nanostructuring process using TNIL. First, the target substrate is covered by a layer of thermoplastic polymer (serving as imprinting resist) normally through a standard spin-coating procedure. Thereafter, an imprinting mold decorated with pre-set patterns is used to transfer the features of the topological patterns into the polymer layer through mechanical imprinting under a specific pressure. After heating up to a specific temperature which corresponds to the initiation of the glass transition for the polymer, the topological architectures obtained from the imprinting mold is solidified. After cooling down to room temperature, the mold is peeled off from the substrate. With the topological polymer as mask, selective etching is performed to further transfer the pattern onto the underlying substrate. While for a UVNIL process, a UV-curable photopolymer is adopted as the resist chemical instead of the thermoplastic polymer. After bringing the imprinting mold and the resist layer into contact, UV light cures the resist chemical, and a pattern is replicated into the resist layer and subsequently to the underneath substrate by selective etching. Each NIL technique has distinct advantages, for example, TNIL is desirable for cost reduction due to the cheap mold even with opaque materials; UV–NIL can be performed at room temperature under low pressure. Aiming to further advance nanostructuring, many other NIL techniques have been investigated, including laser assisted direct NIL, electrical field-assisted NIL, just to name a few. It is worth pointing out that the topological structures with nanometer feature size can be readily transferred onto diverse substrates ranging from silicon wafers to flexible polymers and carbons.[50–52] In view of various advantages such as high throughput, prominent resolution, and extensive substrate-material choice, NIL holds high potentials for nanostructure fabrication.

3.4. Self-Assembly

Self-assembly, a process in which spontaneous assembly of particles occurs, gains tremendous interest as an alternative approach for constructing nanostructure arrays. The idea of self-assembly is inspired by naturally thermodynamic or kinetic processes, for example, the folding of polypeptide chains into functional proteins, the formation of DNA double helix, and directionally interfacial aggregation. As for different processes, various chemical and physical interactions between nanoparticle individuals are produced, driven by the external stimuli in the forms of such as magnetic field, electrical field, inertial force, and hydrodynamic force. With the assistance of the driving stimuli, nanoparticle individuals aggregate in a spontaneous way, achieving nanostructures at a stable equilibrium state (Figure 5d). So far, a variety of self-assembly strategies have been proposed, including such as molecular, physical, and chemical self-assemblies. These strategies have been utilized to construct diverse nanostructures over scales ranging from nanometer to micrometer or even wafer scale. Aided by the self-assembly techniques, a series of nanostructures have been fabricated consisting of different constituents ranging from nanoparticles,[53] nanowires,[54] nanofilms,[55] to complex nanostructures,[56] and their compositional materials vary from semiconductors to metals and alloys as well as supramolecular polymer and biological macromolecules. In general, the spontaneous

self-assembly provides a versatile platform for fabricating nanostructures featuring diverse shapes and materials in a rapid, low-cost, and high-yield way.

3.5. Solution-Phase Deposition

Solution-phase deposition typically includes two strategies: electrochemical deposition and electroless deposition which both are carried out in aqueous electrolytes. These two deposition strategies are characterized by two major advantages: producing nanostructure with complex shapes and capability of scaling down to a few nanometers or up to large sizes, which together entitle solution-based deposition to serve as a fruitful platform for fabricating nanostructures with different dimensions and diverse compositions.

Electrochemical deposition offers important advantages and enormous possibilities for nanostructure fabrication. In a standard process, electrochemical reactions of ions in an aqueous electrolyte are triggered with the power of electric current, and the desired materials are subsequently deposited on conductive substrates (Figure 5e). Many materials with electric conductivity can be efficiently synthesized by choosing appropriate electrolytes and controlling deposition factors in terms of deposition voltage, current, temperature, and electrolyte concentration. It is noteworthy that the as-deposited materials usually exist in the form of amorphous or polycrystalline states, which is not desirable for practical device utilization. Therefore, advantageous treatment of thermal annealing is often followed after electrochemical deposition to enhance the material performance by improving their crystallinity. On the other hand, electroless deposition refers to a process in which chemical reactions occur automatically in an aqueous solution without the drive of external electric power. Compared with electrochemical deposition, electroless deposition has high freedom of broad material choice. Since the process does not need electric energy, the materials that can be deposited is not only limited to conductors but also for non-conductive materials. As a result, a variety of materials (e.g., sulfides, oxides, and metals) have been fabricated routinely using this strategy.[57–59]

3.6. Vapor-Phase Deposition

There are two main strategies in the scope of vapor-phase deposition: chemical vapor deposition (CVD) and physical vapor deposition (PVD), in which precursors are required to produce desired materials on substrates through chemical (e.g., reaction and decomposition) or physical (e.g., thermal vaporization or sputtering) process, respectively.

CVD refers to a chemical process of one or more precursors which can be used for fabricating solid powders of particles or coating films over the substrate surface (Figure 5f). The substrate temperature plays a critical role and greatly influences the initiation and path of different reactions. In addition to the substrate temperature, the physical and chemical properties of the deposited materials can also be controlled by modulating other experimental factors such as substrate material, gas flow, gas pressure, and precursor composition. Categorized by the growth mechanism, CVD generally involves three forms, namely, vapor-liquid-solid (VLS), vapor-solid-solid (VSS), and vapor–solid (VS). In particular, photons, electrons, and ions can be introduced to activate more reactions, for example, in plasma-enhanced CVD and laser-induced CVD. With the progress of nanotechnology, the CVD technique is developing rapidly and playing more and more crucial roles in the fabrication of functional nanostructures. To date, a wide range of solid-state nanomaterials has been successfully fabricated with CVD, including dielectrics,[60] metals,[61] oxides,[62] carbon,[63] and semiconductors[64] which function as passivation layers, protective coatings, heat-resistant coatings, conductive layers, and active materials.

Atomic layer deposition (ALD) could be considered as a special type of CVD techniques. ALD is capable of growing angstrom-scale pinhole-free high-quality thin films of different materials. For a typical material-deposition cycle of ALD, four sequential steps are included: 1) after a first precursor gas is introduced into a reaction chamber, a resultant monolayer is chemisorbed onto the surface of a substrate; 2) the remnant precursor is then purged away by inert gas (e.g., nitrogen gas) after the monolayer of the first precursor covers the entire surface; 3) a second gaseous precursor is introduced and chemisorbed on the monolayer of the first precursor, and meanwhile, chemical reactions occur in which the two types of precursors are transformed into the desired material; 4) likewise, the excess second precursor gas and the formed by-products in chemical reactions are purged away. Film growth can be carried out by repeating this cycle for as many times as necessary. By virtue of the successive and self-terminated chemical reactions between gaseous precursors on the substrate surface, ALD enables precise control over the film thickness. In addition, because active sites are uniformly distributed over the whole surface, chemical reactions take place uniformly over the whole surface even if the surface is not flat and of 3D complex profile, which beneficially results in a reliable thickness uniformity and conformality of the as-deposited film.[65,66] ALD has been utilized for synthesizing a broad range of thin-film materials such as metal,[67] oxides,[68–69] sulfides,[70] carbides,[71] and nitrides.[72]

In a PVD process, the source material goes through a phase change from a solid phase to a vapor phase by physical approaches (e.g., sputtering, heating by laser, or electron beams), and then consolidates back to the solid phase at the substrate surface (Figure 5g). Unlike CVD, PVD does not produce gaseous by-products and is thus more environmentally friendly. PVD exhibits several other advantages; for example, it is suitable for the synthesis of a broader range of materials, ranging from almost all inorganic materials to some kinds of organic materials.[73,74] Hence, PVD has been exploited a lot for nanostructure fabrication. Nevertheless, comparing to ALD, PVD is usually more expensive for the sake of the high-vacuum operation requirement (10^{-6} torr), lower output, and lower selectivity of nanostructure shape.

3.7. Template-Mediated Growth

Template-mediated growth (Figure 6) refers to the techniques whereby templates are utilized to guide the synthesis of nanostructures or the sculpturing of bulk materials into desired

nanostructures. The purpose of utilizing a template is to replicate the geometrical features (e.g., size, shape, arrangement) of the template so that the as-fabricated nanostructures have almost the same geometries as those of the template. Two typical types of templates, namely, porous anodic aluminum oxide (AAO) templates and polystyrene (PS) sphere templates have been tremendously exploited to serve as masks of etching and evaporation as well as molds of replication.[75,76] These two templates possess distinctive characteristics. First, AAO templates and PS templates enable nanostructures with different feature sizes, spanning the wide ranges of 5–1000 nm and 50 nm–5 μm, respectively. Second, many different shapes can be replicated from two templates into nanostructures: PS templates are characterized by 2D monolayer of closely-packed sphere arrays or 3D crystal-like closely-packed spheres while AAO templates offer parallelly arrayed nanopores with high structural controllability (size, shape, and spacing). By virtue of these advantages in geometrical controlling, a large amount of nanostructures can be derived from these two templates, which therefore endow them with promising potentials for nanostructure fabrication and practical device application.

3.7.1. Porous AAO Templates

Since Masuda et al. improved the long-range pore-arrangement regularity of AAO template by a two-step anodization,[77] such template has been widely used for fabricating different nanostructure arrays. AAO templates involve numerous parallel-arrayed pores in which each pore unit is geometrically characterized by pore diameter, pore length, wall thickness, and interpore distance. All pore features can be easily adjusted during anodic anodization and after-treatment such as anodization electrolyte, anodization voltage, anodization time, and pore-widening time.[78] To further enhance the technical effects restricted by time-consuming operation and array defects, a pretexturing technique in which an imprinting stamp decorated with highly ordered convexes was then used to engineer an Al-foil surface by mechanical deformation to guide pore evolution at pre-set nanodent sites during anodization.[79] As a result, the anodization time can be significantly shortened because the first-step anodization for forming periodic nanodents is skipped, and the as-anodized pore arrays turn out to be free of defects over a large area inherited form the perfect arrangement of the convexes on the imprinting stamp. Recently, Wen et al. developed binary pore AAO templates consisting of typically two subsets of pores (denoted as A-pores and B-pores).[80] Intriguingly, two subsets of pores possess independent geometrical controllability for each subset, for example, A-pores can be enlarged from 150 ± 8 to 272 ± 7 nm in size, and B-pores are enlargeable from 63 ± 7 to 255 ± 7 nm. Each set of pores can be used separately or collectively for nanostructure fabrication, thus providing more geometrical options and controllable possibilities.

Because of the extensive compatibility of the AAO template-based growth with numerous material synthesis techniques, different materials can be grown into nanostructures such as insulators,[81] metals,[82] alloys,[83] semiconductor,[84,85] and organics,[86] and a large variety of nanostructures have been prepared including 0D nanoparticles,[87,88] 1D nanotubes,[89] 1D nanowires,[90] 2D nanomeshes,[91] and 3D nanotowers[65,92] (Figure 6a). Notably, by manipulating the sequence of material synthesis and cooperating with etching techniques, the nanostructure arrays replicated from AAO templates gain more space for structural or compositional controlling, for example, several compositions or shapes can be combined into one nanostructure unit.[93,94] Moreover, binary-pore AAO templates further provide a versatile platform for the systematic combination of components with different geometries and compositions, which enable one to investigate intimate interaction between different components in a precise way.[80]

3.7.2. PS Templates

PS spheres can aggregate into 2D- and 3D-ordered arrays by self-assembly under certain conditions to act as templates. The PS spheres are of a uniform size (i.e., diameter) ranging from tens of nanometers to a few micrometers. In addition, thermal annealing or plasma etching can be performed to further modulate the sphere size and inter-sphere space, leading to PS templates with highly tunable size.

The 2D PS template consists of a monolayer of monodispersed PS spheres that exist in a form of hexagonally close-packed array on a substrate. The monolayer PS templates, prepared on the planar surface of a substrate by self-assembly at water/air interface,[95] spin-coating,[96] and drop-casting,[97] offer a versatile platform for surface patterning. In conjunction with numerous material-synthesis approaches, highly ordered nanostructure arrays can be easily obtained which are characterized by different shapes and broad size ranges (Figure 6b). For example, by taking advantage of PVD, honey-comb arrayed nanodots of various materials are obtainable through perpendicular evaporation onto the PS template:[98,99] if the material evaporation is performed with an angle with respect to the PS template, arrays of crescent-like nanostructures are synthesized;[100] performing evaporation, as the PS template is rotated at a certain rate, leads to arrayed nanorings;[101] if one performs dry etching to shrink PS size before PVD, 2D nanomeshes with tunable pore sizes can be deposited and exploited after removing the PS spheres.[102] In addition to 0D nanoparticles and 2D nanomeshes, highly ordered 1D nanostructures such as Si nanowires are obtainable by combining PS templates and a dry-etching process in which the arrangement of PS spheres defines the spatial configuration of the nanowire array on the Si-wafer surface.[103]

3D PS templates consist of many layers of PS spheres that can be closely packed in face-centered cubic assembles on a substrate. Because of the 3D spatial configuration, the crystal-like PS template is particularly suitable for constructing 3D nanostructures.[104–106] The fabrication process for replicating 3D nanostructure counterparts usually includes typically three sequential procedures: engineering PS spheres in 3D closely packed arrays; filling the desired material into the inter-sphere gap; removing the PS template by thermal or chemical treatments (Figure 6b). Because of many advantages such as simple operation, low cost, short time, and high yield, the template-mediated growth can serve as an excellent platform for nanostructure fabrication.

As indicated in Section 3, an enormous variety of WDNs can be fabricated with controllable structural parameters. The above-mentioned seven fabrication techniques are all capable of structural tuning, but each has their superiorities for controlling the four key geometrical parameters of WDNs (size, shape, hetero-architecture, and spatial arrangement): a) techniques I, II, III, IV, and VII are highly appealing for size controlling; b) techniques I, II, III, and VII show excellent shape controllability; c) techniques V and VI have high degree of controlling freedom over the hetero-architecture formation; while d) techniques I, II, III, and VII represent the main work-horses for tuning spatial arrangement. It can be envisaged that combining two or more of such techniques could supply more platforms for WDN fabrication. For example, with the assistance of templates, vapor-phase deposition can give birth to 0D–3D WDNs with extensively tunable geometries. In particular, the size, shape, and spatial arrangement of WDNs can be tuned by altering the corresponding features of AAO templates, while hetero-architectures of WDNs are easily controllable by editing the growth sequence of vapor-phase deposition for different materials.

Based on the above-mentioned cutting-edge fabrication strategies, intensive investigations have been performed for WDNs to improve the performance of electrochemical energy applications, including electrocatalysis, photoelectrocatalysis, batteries, and supercapacitors, with the details being highlighted in the following two chapters.

4. Well-Defined Nanostructures for Electrocatalysis and Photoelectrocatalysis

Electrocatalysis and photoelectrocatalysis are among the most important processes in many renewable energy conversion and storage devices. An ideal prospect for sustainable energy-based society could be renewable energy, such as solar, hydraulic, wind and tide energy, which can be used to generate electric energy, which will be further converted and stored as chemical energy in electrolyzers and charging metal–air batteries. Moreover, the solar energy can also be directly converted into fuels and chemicals via photo(electro)catalysis, and the stored chemical energy can be converted into electric energy by fuel cells and discharging metal–air batteries.[107–116] To this point, electrocatalysis and photoelectrocatalysis play important roles in these processes, while the WDNs are essential in determining and improving the performance of the catalysts. In this chapter, various 0D, 1D, 2D, and 3D WDNs in terms of controllable size, shape, hetero-architecture, and spatial arrangement used for electrocatalytic and photoelectrocatalytic applications will be systematically discussed.

4.1. Electrocatalytic and Photoelectrocatalytic Reactions for Energy Conversion and Storage

Basically, the electrocatalysis and photoelectrocatalysis can link three main conversion cycles between mass and energy, that is, water, carbon, and nitrogen cycles. These cycles play important roles in the ecosystem as well as the energy conversion and storage applications (**Figure 7**).[117–124] For electrocatalysis applications, in H_2/O_2 fuel cells, the anodic hydrogen oxidation and cathodic oxygen reduction reactions (HOR and ORR) generate water and electric energy; while in water splitting electrolyzers, water is split into hydrogen (via hydrogen evolution reaction, HER) and oxygen (via oxygen evolution reaction, OER) as the products, at the consumption of electric energy. Moreover, the fuel cell and electrolyzer devices can be integrated into a single unit, namely regenerative fuel cells, which hold promising potential in space applications. The carbon-containing organic molecules, such as formic acid, methanol, ethanol, dimethyl ether, can be directly used as fuels at the anode for the fuel cells, generating carbon dioxide, water, and electric energy. Inversely, the carbon dioxide can be reduced (via carbon dioxide reduction reaction, CO_2RR) in electrolyzers and form value-added chemicals and fuels, such as CO, methane, methanol, ethanol. The biomass-derived chemical intermediates, such as glycerol, furan, 5-hydroxymethyl-2-furfural, can also be converted into value-added fine chemicals by electrocatalytic methods. As for the nitrogen cycle, the nitrogen fixation to ammonia (via nitrogen reduction reaction, NRR) can be carried out by the electrolyzers under ambient conditions, and the obtained ammonia is an energy carrier that can be employed in the direct ammonia fuel cells. Particularly, the rechargeable metal–air batteries, also named as metal–air fuel cells in some cases, can be established based on ORR/OER (discharge/charge) processes. The photoelectrocatalysis applications can be established based on electrocatalysis applications involving high-performance photoresponse components in the catalysts, which provide photogenerated electrons and holes and accelerates the redox reaction kinetics. In these promising applications (e.g., fuel cells, electrolyzers, photoelectrolyzers, and metal-air batteries), the performance of the device is highly dependent on the electrocatalytic and photoelectrocatalytic reactions. Therefore, the rational design and synthesis of catalysts and electrodes with WDNs are essential to promote both the electrocatalytic and photoelectrocatalytic reactions.

As shown in Figure 7, a typical electrocatalytic or photoelectrocatalytic reaction of the targeted reactant usually follows five steps, including i) the diffusion of the reactants from the bulk electrolyte to the catalyst surface, ii) the reactant adsorption (might involve activation process in some cases) on the active sites, iii) the core electrocatalytic or photoelectrocatalytic reaction of the adsorbed reactant into the adsorbed product (redox reactions without or with illumination), iv) the desorption of the product from the active sites, and v) the diffusion of the desorbed product from catalyst surfaces into the bulk electrolyte. Based on the Sabatier principle, steps ii) adsorption and iv) desorption should be exactly on the active sites, and should be neither too weak nor too strong. If the adsorption is too weak, the catalyst active sites will fail to bind with the reactant; if the adsorption is too strong, the products will be difficult to desorb and recover the active sites. Ideally, both the adsorption and desorption processes should be fast. Ideally, it is preferred that the reaction rate of step (iii) is fast so that the overall electrocatalytic and photoelectrocatalytic reaction is accelerated, the turnover frequency (TOF) is high, and the intrinsic activity is high. This requires highly efficient catalysts, and, particularly, photoresponsive catalysts with excellent light absorption capability

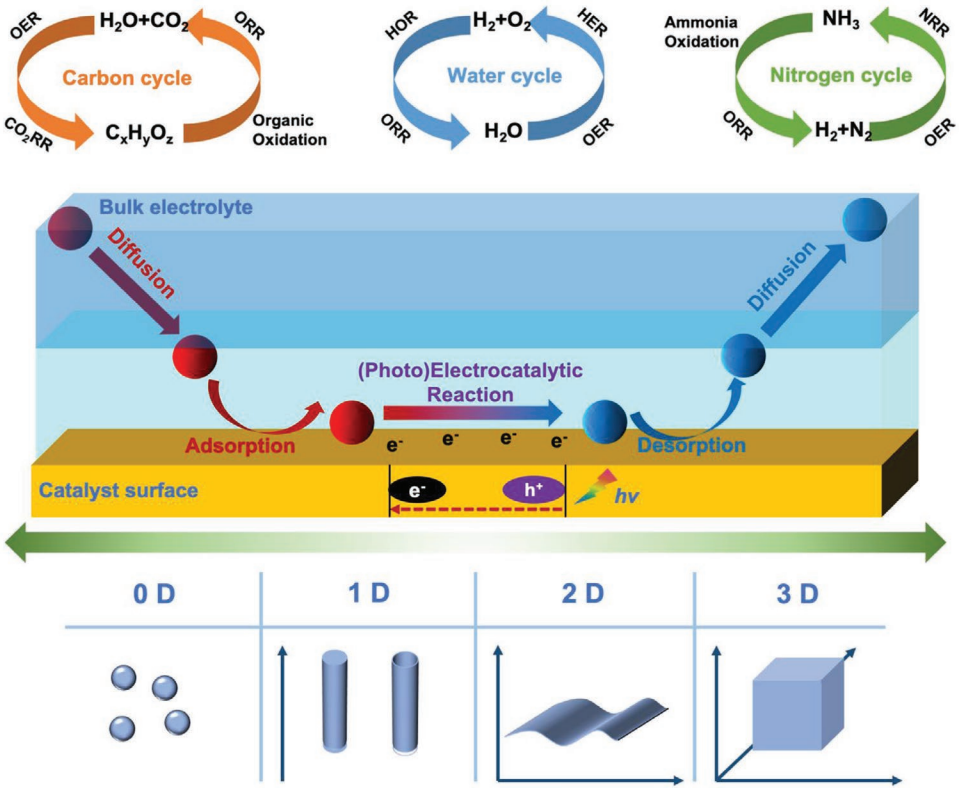

Figure 7. Schematic of electrocatalytic and photoelectrocatalytic reactions on the catalyst–electrolyte interfaces. The carbon, water, and nitrogen cycles can be linked by electrocatalysis and photoelectrocatalysis. The typical electrocatalytic or photoelectrocatalytic reaction contains five steps, including diffusion of reactants onto catalyst surface, adsorption, electrocatalytic and/or photoelectrocatalytic redox reaction, desorption of product, and diffusion into the bulk electrolyte. The catalysts and electrodes can be designed as 0D, 1D, 2D, or 3D WDNs to promote the rate of each step.

for PEC. Besides, in both electrocatalysis and photoelectrocatalysis, the performance of the catalyst/device is usually determined by the current density with respect to the catalyst mass or surface area. In this regard, a large number of active sites per unit catalyst mass and/or electrode surface area (i.e., high active site density), which can be exposed to the reaction interfaces, is highly desired. It should be noted that even though the steps (ii)(iv) are fast enough, the mass transfer could limit the overall catalytic reaction performance if steps (i) and (v) are relatively slow. Based on the above discussion, the electrocatalytic and photoelectrocatalytic performance is primarily influenced by the properties (e.g., intrinsic activity, active site density, mass transportation channels, and illumination absorption capability) of surfaces and structures of the catalysts and electrodes.

The rational design of electrocatalysts and photoelectrocatalysts with WDNs play an essential role in i) enhancing the intrinsic activity and active site density, ii) building more mass transportation channels, and iii) promoting the light absorption and the production of photogenerated electrons and holes. Building the WDNs from 0D to 3D, that is, controlling the size, shape, hetero-architectures, and spatial arrangement, can efficiently tune the surficial atom arrangement, modify the electronic structure of the active sites and surface strain by alloying, construct unique core–shell structure, etc., which are important strategies to enhance the intrinsic activity of the catalysts. To have more exposed active sites (i.e., increasing the active site density), various strategies, such as decreasing the 0D particle size and constructing well-defined architectures and spatial arrangement including high length-to-diameter ratio 1D nanofiber arrays, large surface area 2D materials, and 3D hollow nanoframes, have been developed. The 1D nanofiber array and hierarchically porous well-defined 3D architecture can provide more channels for mass transportation. For photoresponsive materials, the WDNs from 0D to 3D, in terms of size, shape, architecture, and spatial arrangement, are important to enhance the light response capability and production rate of photogenerated electron–hole pairs (**Table 1**).

In the following, we will summarize the important and representative advances for the WDNs, from 0D to 3D, in enhancing the performance of electrocatalytic and photoelectrocatalytic reactions. In the first four parts, we will primarily discuss the electrocatalytic process in terms of 0D, 1D, 2D, and 3D WDNs. In the end, we will particularly demonstrate the WDNs in photoelectrocatalytic applications.

4.2. 0D WDNs for Electrocatalysis

In electrocatalysis, 0D nanoparticles are the most commonly studied and used catalysts in the research labs and commercial applications. In early investigations regarding fuel cells and water splitting applications, the Pt bulk materials were found to be highly active as electrocatalysts. However, due to the low active site density on the smooth Pt foils, the current density of these devices was very low; meanwhile, a large amount of Pt was needed at the electrodes. With further studies, using Pt

Table 1. The primary benefits and possible limitations of WDNs in different dimensionality for electrocatalytic and/or PEC reaction.

Dimensionality	Benefits	Possible limitations
0D	Promoted strain and ligand effects[125]	Active site density to be improved[126]
	Precisely tuned electronic structure[127]	
	The higher surface area by nanometerization[128]	Instability[129,130]
	Facile synthetic procedures[131]	
1D	High length-to-diameter ratio[132]	Low contact resistances[133]
	Optimized geometric and electronic structure[134]	
	Opened channels for mass transfer[135]	Challenging synthesis[136,137]
	Improved conductivity[132]	
2D	High surface-to-volume ratio[138]	Stacking and aggregation[139]
	High conductivity[140]	
	High active site density[138]	Limited mass transfer[141,142]
	Strong affinity to nanoparticles[143,144]	
3D	High surface-to-volume ratio[145]	Complicated synthetic procedures[146]
	High active site density[145]	
	Opened channels for mass transfer[147]	Undesired structure degradation[148]
	Unique electronic structure[149]	

particles with small sizes became an efficient strategy because it not only significantly improves the current per electrode area but also decreases the Pt amount needed in the electrodes. Currently, the 0D Pt particles in the nanoscale (i.e., a few nanometers in diameters) loaded on appropriate support materials have been widely used as the catalysts in electrocatalysis.[150] A tremendous amount of effort has been devoted to constructing the well-defined 0D nanostructures with controllable size, shape, and composition to achieve the desired electrocatalytic performance (activity, stability, and selectivity).

The surface of the nanoparticles mainly hosts active sites. It has been well understood that different facets of the nanoparticle crystals demonstrate different electrocatalytic activity. For example, in sulfuric acid, Pt (110) facet presents the highest ORR activity, while the Pt (111) facet has the lowest ORR activity because the sulfuric groups strongly adsorb on Pt (111) facets and block the active sites.[151] However, in perchloric acid, the ORR activity of Pt (111) and Pt (110) are similar, much higher than that of Pt (100) facet.[152] Therefore, the rational design of the WDNs of 0D nanoparticles is a promising approach to improve the electrocatalytic activity. The referential facets of Pt nanoparticles are usually related to their shape and morphology, for example, Pt cubes are enclosed by Pt (100) facets, and Pt octahedra are enclosed by Pt (111) facets.[153] Therefore, the shape control of the electrocatalysts is important.

In 1997, EI-Sayed et al.[154] employed sodium polyacrylate as the capping agent and hydrogen as the reductant to synthesize Pt nanocrystals with different shapes, including cubes, octahedra, and truncated cubes. To our knowledge, this is the first report using the chemical capping agents to control the shape of Pt nanocrystals by a wet chemical method. Following that strategy, many works have been reported in the controlled synthesis of Pt nanocrystals with specific shapes. The most studied 0D WDN of these Pt nanocrystals is enclosed by low-index facets such as Pt (100), Pt (111), and Pt (110). On the other hand, the high-index facets can host much more under-coordinated sites than the low-index facets, and are believed to promote the appropriate adsorption of reactants and the electrocatalytic redox kinetics.

A few novel strategies have been developed to achieve high-index Pt nanocrystals. For example, S. G. Sun group employed an electrochemical square-wave potential method to control the high-index facet formation.[155] Starting from the Pt nanospheres (without special well-defined facets) deposited on the glassy carbon electrode, the electrochemical square-wave potential successfully realized the evolution of high-index Pt facets, forming a tetrahexahedral (THH) shape enclosed by 24 high-index facets including Pt (730), Pt (210), and Pt (520) planes (**Figure 8**a). Particularly, the yield rate of the high-index THH Pt nanocrystals is higher than 90%, demonstrating that this electrochemical square-wave potential method is promising in controlling the well-defined 0D nanostructures of Pt nanocrystal. The high-index facets in the THH Pt nanocrystals have abundant steps and dangling bonds, thus demonstrating significantly enhanced intrinsic activity toward the electrocatalytic oxidation of organic molecules such as formic acid and ethanol. As shown in Figure 8a, the potential for formic acid oxidation at 0.5 mA cm^{-2} is enhanced by 60 mV compared with Pt nanospheres and Pt/C catalysts; while the potential for ethanol oxidation at 0.2 mA cm^{-2} shifts negatively by 80 mV, indicating the much-enhanced activity.

The electrochemical square-wave potential method is powerful in controlling the high-index facet formation because Pt can be etched at the high applied potential and redeposited at the low applied potential. Therefore, the square-wave protocol can well control the shape, for example, preferential exposure facets, of the Pt nanocrystals. By tuning the upper and lower potential limits of the square wave as well as the period of polarization, unique morphologies other than THH are expected. For example, the convex hexoctahedron (HOH) and trapezohedron (TPH) can be obtained by modulating the square-wave potential limits.[156] As shown in Figure 8b, the HOH nanostructure bridges the shape evolution from well-defined THH nanostructure to TPH nanostructure, in which the upper and lower potential limits play an important role. It is concluded that increasing the lower potential limit predicates the decreased growth rate of Pt nanocrystals, while increasing the upper potential limit means the increased etching rate of Pt atoms in solutions.

The above-mentioned well-defined 0D nanostructures are all in the convex shapes. Interestingly, concave shapes can also be fabricated and well-tuned. Figure 8c demonstrates the synthesis of concave PtCo nanopolyhedrons on the reduced graphene oxide. In this work, the reduced graphene oxide support is crucial for shape control. The high-index facets of the concave PtCo nanopolyhedron catalyst showed enhanced activity toward both the formic acid oxidation and ORR.[157] To be specific, the formic acid oxidation current density on concave PtCo

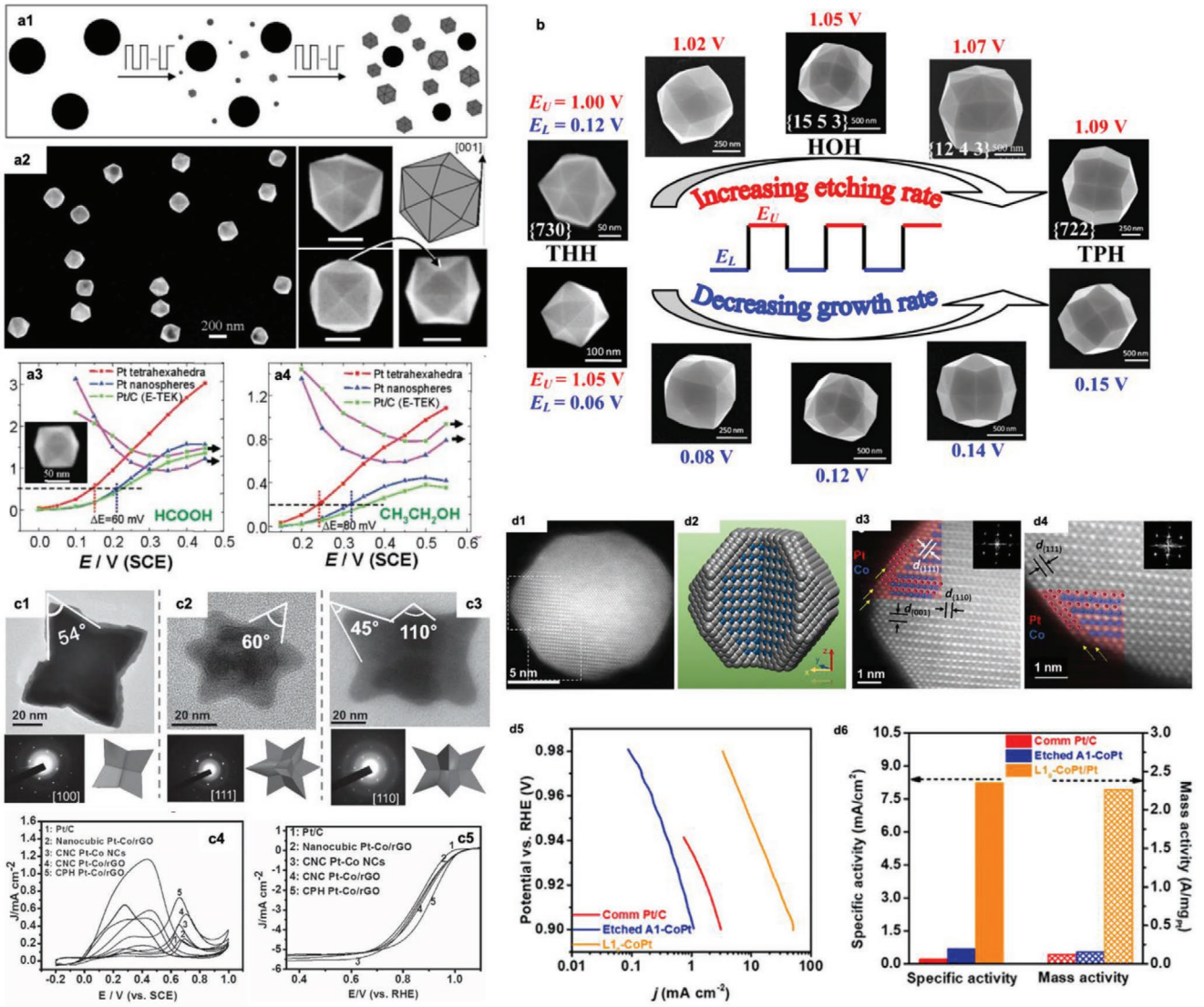

Figure 8. a1) Scheme of THH Pt NCs formation from the Pt nanospheres under the electrochemical square-wave potential method; a2) the shape of THH Pt NCs and the views along different orientations; a3,a4) the activity toward formic acid oxidation and ethanol oxidation reactions.[155] b) The evolution of Pt NC shapes from THH to TPH via HOH by tuning the parameters of the electrochemical square-wave potential method.[156] c1–c3) TEM images, corresponding SAED patterns, and structure illustrations of the PtCo concave nanopolyhedrons along with the (100), (111) and (110) directions; c4,c5) the activity for formic acid oxidation and ORR.[157] d1–d4) Shape, schematic, and atom arrangement of the $L1_0$-CoPt@Pt Core@Shell catalyst (the darker atoms are Pt, and the lighter atoms are Co; for the colored zoon, the silver-colored atoms are Pt, and the blue-colored atoms are Co); d5,d6) the specific and mass activity toward ORR.[158] (a) Reproduced with permission.[155] Copyright 2007, the American Association for the Advancement of Science. (b) Reproduced with permission.[156] Copyright 2013, American Chemical Society. (c) Reproduced with permission.[157] Copyright 2015, Wiley-VCH. (d) Reproduced with permission.[158] Copyright 2019, Elsevier.

polyhedrons for the 1st and 2nd peaks are 3.5 and 3.0 times higher than those of the Pt/C catalyst, respectively. The concave PtCo polyhedrons also show excellent activity for ORR, with a specific activity of 1.53 mA cm^{-2} at 0.9 V, which is 6.7 times higher than that of the Pt/C (0.23 mA cm^{-2}). It should be emphasized that the 0D Pt nanoparticles with high-index facets have shown great promises in different electrocatalytic reactions as demonstrated above, including formic acid oxidation, ethanol oxidation, and ORR,[155,157] highlighting the importance of the well-defined 0D nanostructures for electrocatalysis. It should be mentioned that in electrocatalysis, the combination of WDNs in different dimensions is also important, taking the advantages of synergistic effects from different components. For example, other than the shape control in ref. [157], the 2D reduced graphene oxide can also be used as support materials for Pt nanoparticles due to the large surface area and the strong affinity to catalyst particles.

Considering the high cost and limited resources of Pt-group-metal (PGM) catalysts, the development of low-PGM electrocatalysts is highly desired. To this end, by alloying Pt with the cheap secondary transition metals (e.g., Fe, Co, Ni, etc.), the Pt amount used in the electrode can be significantly decreased.

Besides, the electronic structure of the active Pt atoms can be modified, and the Pt strain can be well-tuned by the secondary metals to control the surface energy on Pt's interactions with oxygenated species, leading to greatly enhanced activity.[159] In some cases, the secondary metals can also alternate the electrocatalytic reaction mechanisms, for example, promoting the oxidation and removal of poisoning intermediates during the organic molecule oxidation process.[119] Learning from the shape control of Pt nanocrystals discussed above, the Pt-based alloy nanoparticles with special facets are also favorable to enhance the activity. For example, for ORR, the Pt_3Ni (111) demonstrated 10-fold higher activity than Pt (111) facet and 90-fold higher activity than that of the state-of-the-art Pt/C catalyst.[160]

As discussed in Section 4.1, the electrocatalytic reaction takes place on the catalyst surface; therefore, the surface atoms are more related to the electrocatalytic reactions. For Pt nanoparticles, except for the very few surface layers, the bulk Pt atoms have no contribution to the active surficial active sites. Even for the Pt-based alloy nanoparticles, in which the Pt and secondary metal atoms are uniformly distributed, most Pt atoms are in the bulk phase. Importantly, the secondary metals are usually unstable under corrosive electrocatalytic environments, leading to decreased stability. For example, the Fe, Co, and Ni atoms are easily dissolved in the acidic solutions. In this regard, the surficial Pt-rich PtM@Pt core@shell nanostructures are very promising. The Pt-rich shells can provide a large number of active sites and also protect the secondary metal from leaching under harsh environments; meanwhile, the M-rich PtM core can tune the electronic structure and stress of surficial Pt atoms and enhance the catalyst activity.[161] As an ultimate core@shell structure, the Pt single layer catalyst prepared by the underpotential deposition method shows great promise toward highly active and stable electrocatalysis.[162]

Both the PtM alloying nanoparticles and the traditional core@shell nanostructure contain randomly distributed metal atoms inside the bulk and on the surfaces. Correspondingly, designing highly ordered 0D nanostructures is another promising strategy to improve the intrinsic activity. By pyrolyzing the PtM alloying nanoparticles, the conventional facet-centered cubic (fcc) structural PtM nanoparticles can be converted into a highly ordered intermetallic compound, further promoting the surficial electrocatalytic reaction kinetics. For example, starting from PtCo alloying nanoparticles, the highly ordered intermetallic PtCo alloys and highly ordered PtCo@Pt core@shell nanostructures, consisting of the tetragonal PtCo core and Pt shell, can be obtained (Figure 8d) after the multi-step annealing and acidic leaching.[158] Such highly ordered intermetallic particles with well-defined 0D nanostructure present significantly suppressed Co loss and enhanced ORR intrinsic activity. As shown in Figure 8d, the highly ordered PtCo@Pt catalyst (i.e., $L1_0$-CoPt/Pt) demonstrated a specific activity of 8.26 mA cm^{-2} and a mass activity of 2.26 A mg^{-1}_{Pt}, which are 38 and 19 times, respectively, higher than those of the Pt/C catalyst. Even in the practical fuel cells, the mass activity of $L1_0$-CoPt/Pt can reach 0.56 A mg_{Pt}^{-1}, exceeding the DOE 2020 fuel cell target (i.e., 0.44 A mg_{Pt}^{-1}). By building the highly ordered intermetallic nanostructures, the intrinsic activity of Pt-free metal-based catalysts can be remarkably improved. For example, the trimetallic PdCuFe catalysts, which are much cheaper than Pt-based catalysts, demonstrated Pt-like ORR activity after converting into the highly ordered 0D WDNs.[163] Although the highly ordered intermetallic compound is preferred due to its well-defined 0D nanostructure and considerable electrocatalytic activity, it should be noted that the synthesis of these catalysts usually requires high-temperature annealing, which, however, leads to the aggregation of metal nanoparticles, that is, big particle size and thus low surface area. The confined strategies during annealing will help limit the excessive growth of intermetallic nanoparticles.

To further decrease Pt usage, the development of the well-defined single Pt atom catalysts emerged as a "hot" research topic in recent years. If only considering the Pt atom and its local coordination, such a moiety can be regarded as the 0D nanostructure. As shown in **Figure 9**a, the Pt single atoms on the onion-like carbon nanospheres demonstrate much better HER mass activity concerning the much less Pt loading than the conventional Pt/C catalyst, indicating excellent Pt utilization for the single atom strategy.[164] Through the unique ALD technique, the synthesis of single Pt atoms on the supports can be precisely controlled at the atomic level. In ref. [165], Sun et al. reported the ALD synthesis of Pt single atoms on graphene support, and the Pt loading and deposition density on graphene can be well controlled by adjusting the ALD deposition cycles. Impressively, such Pt single-atom catalyst shows remarkably improved activity toward methanol oxidation by about ten times compared to the commercial Pt/C nanoparticle catalyst (Figure 9b). The noble metal catalysts with well-defined single-atom nanostructures have shown great promise in different electrocatalytic reactions in HER, methanol oxidation, ORR, and fuel cells.[166] Besides, the single Ru atom catalyst shows excellent activity for NRR, that is, ambient ammonia synthesis (Figure 9c).[167]

In the single-atom catalysts, the well-defined local coordination structure not only decreases the noble metal usage but also tunes the electronic structure, which enables the non-noble metal single-atom catalysts to possess Pt-like activity toward electrocatalytic reactions.[168,169] One of the representative examples is the single Fe atom coordinated with N embedded in the carbon matrix, that is, Fe-N-C catalysts, for ORR in fuel cells. In the past decade, the activity of Fe-N-C catalyst has been significantly enhanced; for example, Dodelet group reported that the pyrolyzed Fe/N/C-based catalyst was able to provide, in fuel cells, the same current density than Pt.[170–171] The FeN_x moieties have been well accepted as the primary active sites for ORR in fuel cells.[172] As shown in Figure 9d, by using the advanced aberration-corrected scanning transmission electron microscopy (STEM), the FeN_4 sites can be directly visualized.[173] Actually, the non-noble metal single-atom catalysts have been widely used in different electrocatalytic applications. As shown in Figure 9e, the Ni single-atom catalyst shows almost 100% faradic efficiency toward CO product derived by carbon dioxide reduction reaction.[174]

The well-defined single-atom electrocatalysts have shown great promise in various electrocatalytic reactions. However, many challenges still exist; for example, the active site density of the single-atom catalysts is quite low. This could be caused by the fact that they always tend to aggregate during the high-temperature pyrolysis once many metal precursors are introduced.

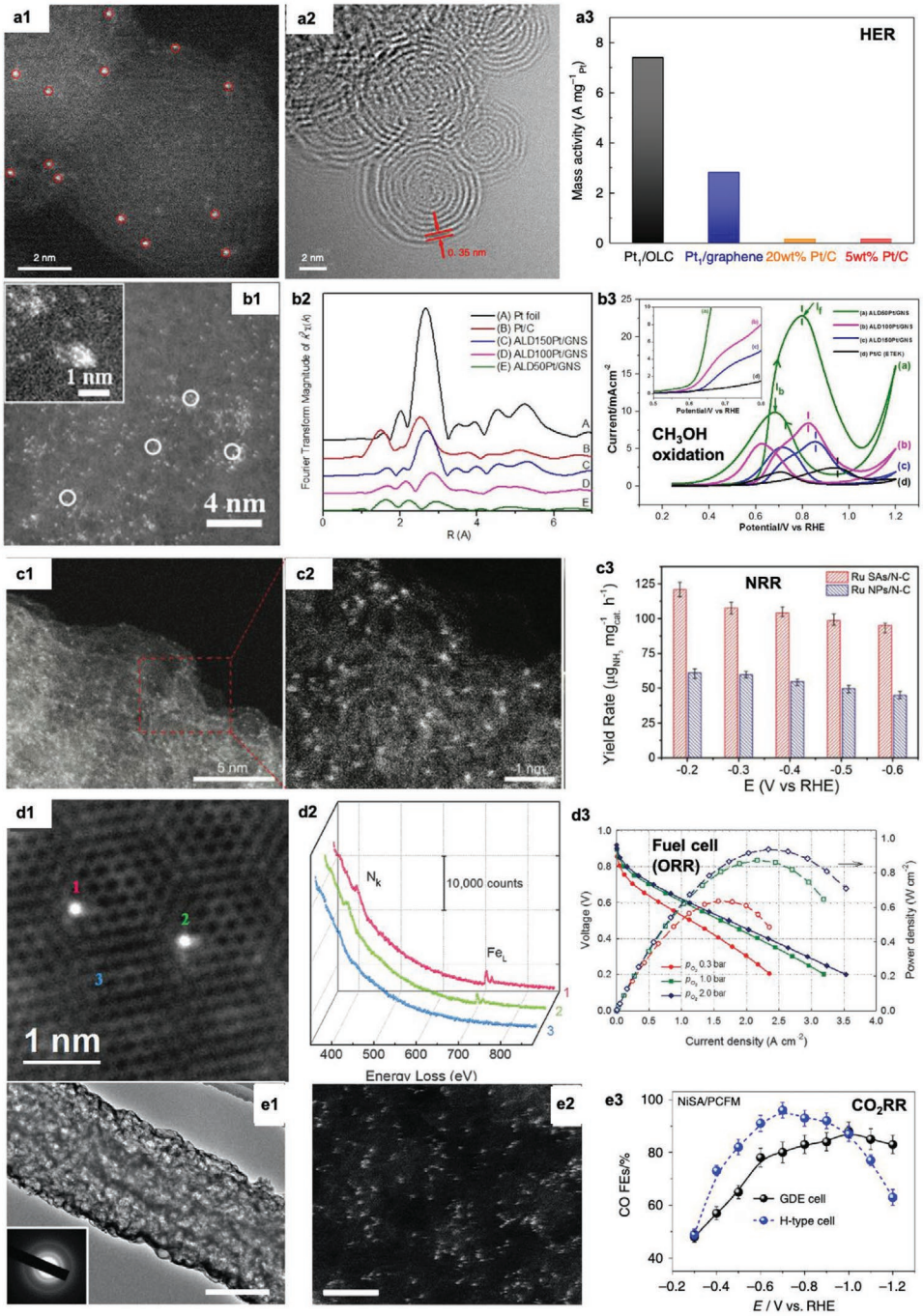

Figure 9. a1,a2) Morphology, structure, and a3) HER mass activity of Pt single-atom catalyst.[164] b1,b2) Morphology, structure, and b3) activity for methanol oxidation of Pt single-atom catalyst.[165] c1,c2) Morphology, structure, and c3) yield rate of ammonia by NRR of Ru single-atom catalyst.[167] d1,1d) Morphology, structure, and d3) fuel cell performance of Fe single-atom catalyst.[173] e1,e2) Morphology, structure, and e3) CO Faradic efficiency of CO_2RR of Ni single-atom catalyst.[174] (a) Reproduced with permission.[164] Copyright 2019, Springer Nature. (b) Reproduced with permission.[165] Copyright 2013, Springer Nature. (c) Reproduced with permission.[167] Copyright 2018, Wiley-VCH. (d) Reproduced with permission.[173] Copyright 2017, The American Association for the Advancement of Science. (e) Reproduced under the terms of the Creative Commons CC BY License.[174] Copyright 2020, Springer Nature.

The well-defined metal–organic frameworks (MOF) can be employed as the precursors to control the single-atom catalyst formation.[175] As an ultimate target, controlling the well-defined arrangement of single atoms (e.g., well distribution with a high density of the active sites) is highly desired.

4.3. 1D WDNs for Electrocatalysis

The typical 1D nanostructures, such as nanowires, nanofibers, and nanotubes, possess a high aspect ratio (i.e., the ratio of length to diameter). Such well-defined 1D nanostructures can

provide high surface area and thus a large electrochemical surface area. At the same time, the 1D nanostructure has high conductivity for electrons along the axial direction, which is highly desired for electrocatalysis. Combining with the appropriate surface engineering strategies and concepts discussed in the well-defined 0D nanostructures, the surficial atomic steps in the well-defined 1D nanostructure can further improve the overall electrocatalytic performance.[176,177]

As shown in **Figure 10**a, the PtNi alloy nanowires (NWs) were synthesized by a thermal annealing method in a mixed hydrogen and argon atmosphere, derived from core@shell Pt@NiO nanowire starting material, which was first synthesized through reducing Pt and Ni precursors in a mixed solvent, including 1-octadecene and oleylamine.[126] As expected, the PtNi nanowire with smooth surfaces presented enhanced electrochemical surface area than the conventional 0D Pt nanoparticles supported by carbon (usually ≈70 m^2 g_{Pt}^{-1}). Further, the Ni atoms were completely removed by the electrochemical dealloying method, leaving the jagged Pt nanowires. Such jagged Pt nanowires showed significantly enhanced electrochemical surface area of up to 118 m^2 g_{Pt}^{-1}. Particularly, the jagged Pt NWs catalyst demonstrated an extremely high specific ORR activity of 11.5 mA cm^{-2} and a mass ORR activity of 13.6 A mg_{Pt}^{-1} at 0.9 V. It is notable that Ni is totally leached during the electrochemical dealloying process (Figure 10a) so that the contributions from Ni can be excluded. The outstanding ORR activity of such jagged Pt NWs is due to the well-defined 1D nanostructure.

In addition to the electrochemical dealloying method, Pt NWs can also be well controlled using the simple wet chemical strategy. For example, the single crystalline Pt nanowires (4 nm in diameter) can be synthesized by reducing the Pt precursor, hexachloroplatinic acid, in the presence of formic acid as a reductant and capping agent at room temperature,[178] without any other additives or templates. As shown in Figure 10b, the Pt nanowire catalyst demonstrated three times better specific activity, in practical fuel cells, than the state-of-the-art commercial Pt/C catalyst made from 0D Pt nanoparticles. This pioneering work stimulated a new research direction of using Pt nanowire-based catalysts for fuel cell applications.[179–181]

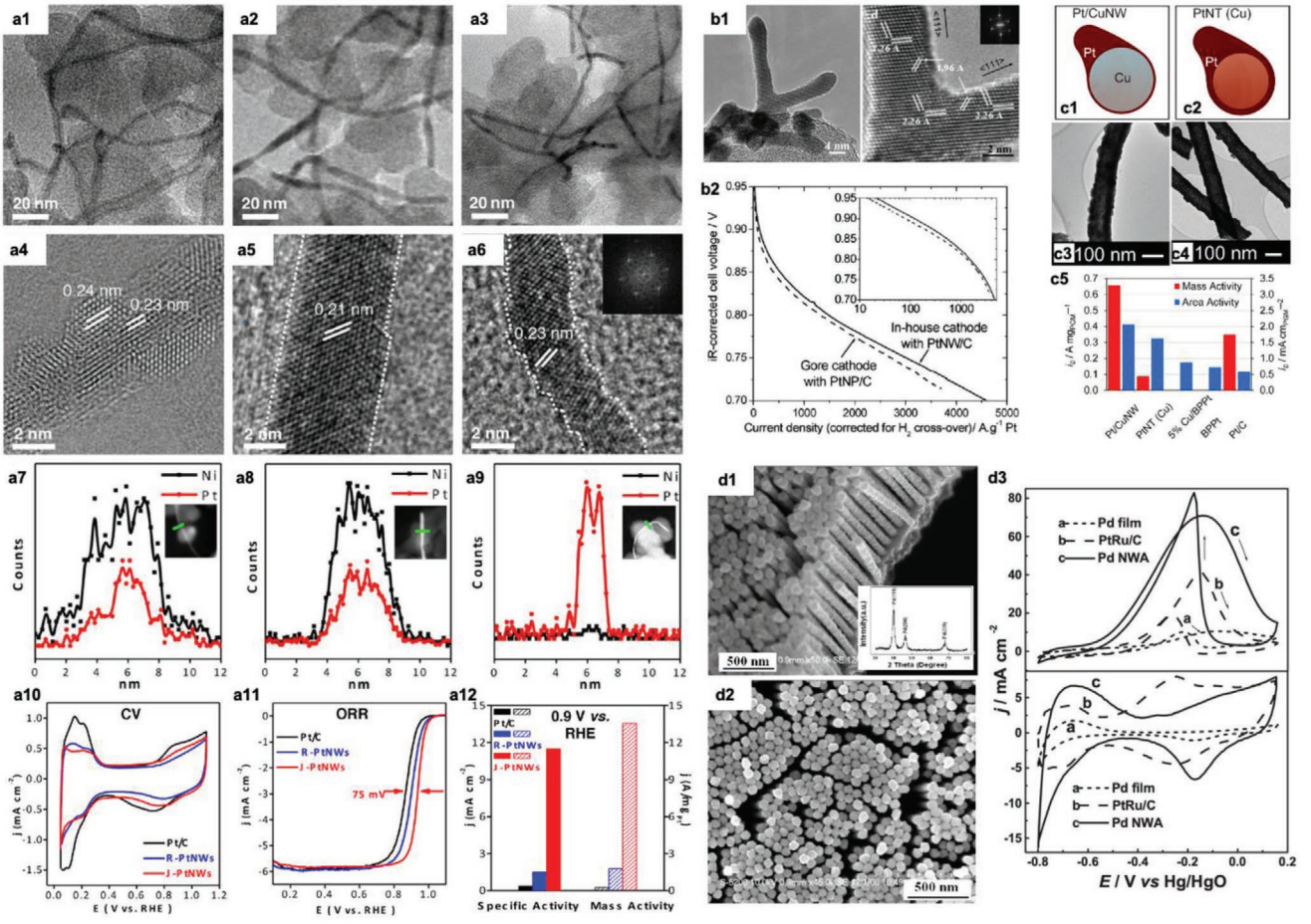

Figure 10. a1–a9) Architecture and composition characterization of different stages of (from left to right) the Pt@NiO core@shell NWs, the PtNi alloy NWs, and the jagged PtNWs; a10–a12) electrochemical behaviors of catalysts.[126] b1) Architecture of the Pt nanowires, as well as b2) its fuel cell performance.[178] c1,c2) Schematic and c3,c4) TEM images of Pt/CuNWs and PtNTs (Cu), as well as c5) the HOR mass and specific activity.[182] d1,d2) The spatial arrangement of Pd nanowire arrays and d3) their activity toward ethanol oxidation.[184] (a) Reproduced with permission.[126] Copyright 2016, The American Association for the Advancement of Science. (b) Reproduced with permission.[178] Copyright 2008, Wiley-VCH. (c) Reproduced with permission.[182] Copyright 2013, American Chemical Society. (d) Reproduced with permission.[184] Copyright 2007, Wiley-VCH.

Similar to the concept of core@shell nanostructures, it is attractive to design well-defined Pt-based 1D core@shell nanostructures. The controlled deposition of Pt thin shells onto the less expensive as-prepared NWs is a promising strategy to increase the Pt utilization and decrease the Pt amount. In ref. [182], the cheaper Cu nanowires were first prepared and then used as the sacrificing template and substrate for Pt shell formation. Through the partial galvanic displacement of Cu with Pt atoms, the Pt/Cu NWs can be synthesized. Furthermore, by complete galvanic displacement of the CuNWs, the hollow Pt nanotubes were obtained (see the illustrations and architecture of Pt/Cu NWs and PtNT catalysts in Figure 10c). Through detailed observations, the Pt/Cu NWs have a diameter of 100 nm and a length of 25–40 µm; while the PtNTs have a wall thickness of 11 nm, an outer diameter of 100 nm, and a length of 5–20 µm. Impressively, the Pt/Cu NWs showed significantly enhanced mass activity (by 1.9 times) and specific activity (by 3.5 times) toward HOR compared with the state-of-the-art commercial Pt/C catalyst. The presence of Cu is beneficial for improving the HOR kinetics, which is likely attributed to the introduced strain on Pt shells and the acceleration of hydroxyl adsorption by surficial Cu species on the catalyst surface. Zhang et al. employed the pre-synthesized dendritic Ag nanowires as the sacrificing template to prepare dendritic Pt hollow nanotubes, via the galvanic replacement reaction. The Pt dendritic tubes showed 4.4 times better activity, and 6.1-fold better stability, for ORR, than those of the state-of-the-art Pt/C catalyst.[183]

The hard-templating synthetic route, also known as "nanocasting," is a straightforward technique to fabricate highly ordered 1D WDNs.[124] The well-defined 1D nanostructures of the non-Pt metal catalysts will greatly improve their electrochemical performance. As shown in Figure 10d, the highly ordered Pd nanowires prepared with the assistance of anodized aluminum oxide (AAO) template demonstrated excellent Pt-like activity toward ethanol oxidation, which is even higher than that of the state-of-the-art PtRu/C catalyst.[184]

Inspired by refs. [182,184], it is expected that the Pt catalysts can be deposited onto the well-defined non-metallic 1D nanostructured templates. **Figure 11**a provides an excellent example. The aligned perylene red whisker arrays were first built as both the template and substrate followed by coating with Pt-based

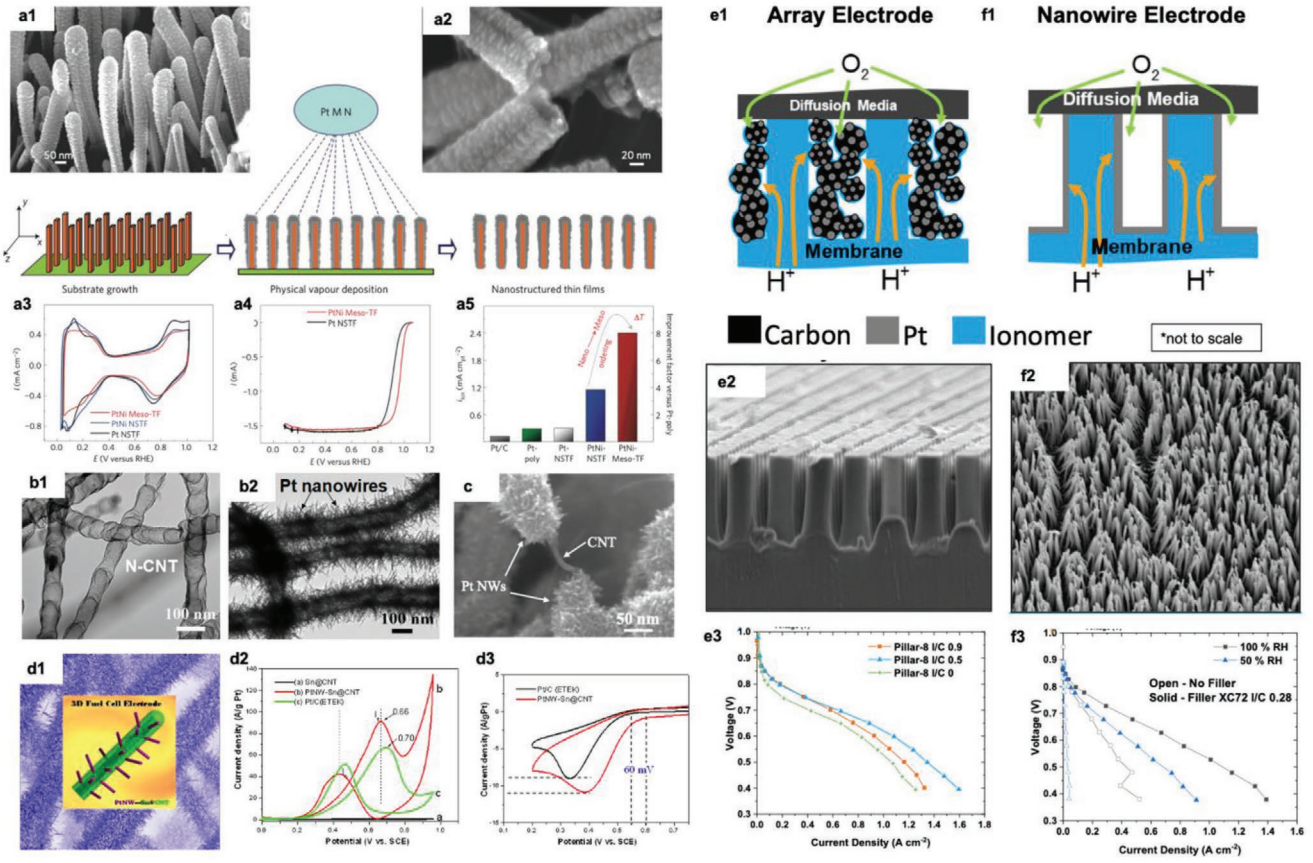

Figure 11. a1,a2) Architecture of the NSTF whiskers, the schematic illustration of the vacuum protocol to grow aligned perylene red substrate and coat with a metallic thin film (Pt, M, and/or N = Ni, Co, Fe, Ti, V); a3–a5) the electrochemical behaviors for ORR.[185] b) TEM images of N-CNTs b1) before and b2) after the growth of Pt NWs.[186] c) Morphology of the Pt NW-MWCNT hetero-nanostructures.[187] d1) Morphology of Pt NWs grown on Sn@CNT nanocables; d2,d3) the electrochemical activity for methanol oxidation and ORR.[188] e1) Illustration, e2) spatial arrangement, and e3) fuel cell performance of the array electrode. f1) Illustration, f2) spatial arrangement, and f3) fuel cell performance of the nanowire electrode.[135] (a) Reproduced with permission.[185] Copyright 2012, Springer Nature. (b) Reproduced with permission.[186] Copyright 2009, The Royal Society of Chemistry. (c) Reproduced with permission.[187] Copyright 2007, American Chemical Society. (d) Reproduced with permission.[188] Copyright 2010, Wiley-VCH. (e,f) Reproduced with permission.[135] Copyright 2018, U.S. DOE.

thin films, forming the nanostructured thin films (NSTF).[185] After annealing, the nanostructured Pt-based thin film will be gradually converted into the mesostructured thin film with the well-defined 1D nanostructures. Such a well-defined configuration demonstrates 20 times higher ORR activity than the Pt/C catalysts. Sun et al. also used various 1D nanostructures, such as CNTs, N-CNTs, and Sn@CNT nanocables, as supports to grow Pt NWs, forming 3D hierarchical nanostructured catalysts which exhibited excellent activity for ORR and MOR (Figure 11b–d).[186–188]

It should be emphasized that the highly ordered well-defined 1D nanostructure arrays not only benefit the electrocatalytic reaction kinetics on catalyst surfaces but also help build the well-defined three-phase interfaces along the axial direction, which is highly desired for electrode fabrication. Taking the fuel cell cathode as an example, the ORR at cathode requires well-defined channels for electron, proton, and oxygen transportation at the same time. However, the excessive ionomer, the proton carrier, in the catalyst layer, might block the mass transportation. The well-defined 1D nanostructure of the electrode is helpful to decrease the ionomer usage and build the desired three-phase interfaces. As shown in Figure 11e, the ionic conductive 1D membrane arrays were proposed with both catalyst and ionomer as fillers, namely the array electrode.[135] The filling catalyst particles can directly contact with the 1D nanostructural membrane arrays, thus decreasing the distance of proton transfer across the catalyst layer. Surprisingly, low ionomer content can be successfully applied by using the array electrode, which still maintains comparable fuel cell performance; even in the absence of ionomer in the catalyst layer, the fuel cell performance did not decrease much (Figure 11e).

In this array electrode configuration, the ionomer is still required to form the ionic conductive networks on the catalyst surfaces. To realize the ionomer-free electrode, another promising 1D nanostructure is the nanowire electrode as shown in Figure 11f. In this configuration, the membrane arrays are covered by the thin Pt catalyst film, where the proton transfer is accomplished by the membrane arrays—there is no need to use ionomer in the catalyst layer. By adding the electronic conductive filler in the array spaces, the fuel cell performance seems not limited by mass transport anymore (Figure 11f).[135]

4.4. 2D WDNs for Electrocatalysis

The 2D nanostructures usually have a high area-to-volume ratio, thus exhibiting high electrochemical surface area and also exposing a large number of active sites. By constructing the under-coordinated sites, the 2D nanostructure surface will have high TOF and fast kinetics toward electrocatalytic reactions. Besides, as the support materials, the 2D nanostructures are more promising to enhance both the dispersibility of electrocatalytic nanoparticles and the support-catalyst interaction than the previously discussed 0D and 1D WDNs, including nanoparticles, nanowires, and nanotubes.

As shown in **Figure 12**a, ref. [189] gives an interesting example of synthesizing ultra-thin Pt-based 2D nanosheets in the presence of CO and oleylamine. By using this strategy, the trimetallic PtPdM (M = Ni, Fe, Co) nanosheets can be obtained. Particularly, the thickness of the PtPdM (M = Ni, Fe, Co) nanosheets is only about 1.4 nm. Due to the unique 2D WDN and the optimal composition, the PtPdNi catalyst demonstrates excellent activity toward the electrocatalytic oxidation of ethylene glycol and glycerol, as well as the ORR (Figure 12a). The optimal $Pt_{32}Pd_{48}Ni_{20}$ catalyst shows 7.7 and 5.4 times higher activity toward ethylene glycol and glycerol oxidation reactions, respectively, compared with Pt/C catalyst. It also shows 7.7 times higher ORR mass activity than that of the commercial Pd/C catalyst. These results indicate that the well-defined 2D nanostructures are generally beneficial for the enhanced kinetics of electrocatalytic reactions.

It is notable that the thickness of the 2D nanostructure in ref. [189] is only about 1.4 nm. The even thinner nanosheet, for example, subnanometer, is highly desired because the area-to-volume ratio can be further increased, which is beneficial for exposing more active sites. Recently, as a new type of 2D material, the bimetallene emerges as a promising electrocatalyst and it is prepared by a facile one-pot wet chemical method.[138] In the presence of high concentration metal acetylacetonate and metal carbonyl precursors, the well-defined 2D nanostructure can be achieved under the moderately reducing conditions. As shown in Figure 12b, the 2D PdMo bimetallene has a sub-nanometer thickness of only about 0.88 nm. Importantly, the surfactants such as polyvinylpyrrolidone, which are conventionally used to control the thickness of 2D nanostructures in the wet chemical methods, are not employed during the bimetallene synthesis. The organic surfactants usually have strong adsorption on the catalyst surfaces and block the adsorption of targeted reactant species. In this regard, the clean 2D PdMo bimetallene is promising as an electrocatalyst. Such well-defined 2D nanostructure delivers a large electrochemically active surface area of up to 138.7 $m^2\ g_{Pd}^{-1}$ so that the utilization of catalyst atoms is extremely high. Reasonably, the ORR mass activity of this PdMo bimetallene is 16.37 A mg_{Pd}^{-1} at 0.9 V, which is 78 times and 327 times higher than that of the Pt/C and Pd/C catalysts, respectively (Figure 12b).

In addition to the noble metal-based 2D catalysts, non-noble metal catalysts with well-defined 2D nanostructures have also been developed. For example, the bismuth oxyiodide (BiOI) nanosheets were first prepared as the precursor, which has nine to ten layers, that is, 8.7 nm in thickness (**Figure 13**a). After the in situ topotactic transformations, the well-defined 2D Bi nanosheets were obtained.[190] The derived Bi nanosheets well maintained the 2D nanostructure of BiOI nanosheet precursor and became even thinner (Figure 13a). The primary product of CO_2RR process using this Bi nanosheets catalyst is the value-added formate along with only a small amount of CO and hydrogen as the byproducts, highlighting the excellent activity and selectivity of the 2D Bi nanosheet catalysts.

In addition to the above-mentioned metallic electrocatalysts, as a typical non-noble metal-based material, the MoS_2 is a rising star for electrochemical hydrogen production, that is, HER.[117] It is believed that the 2H phase of MoS_2 is semiconductive, and therefore the 2H plane of MoS_2 has low HER activity. The conversion from less active 2H basal phase to the highly active 1T phase (metallic conductive) is highly required to design the high-performance MoS_2 electrocatalysts. This understanding was further developed recently by using a well-defined 2D MoS_2 nanosheet as a model catalyst. As shown in

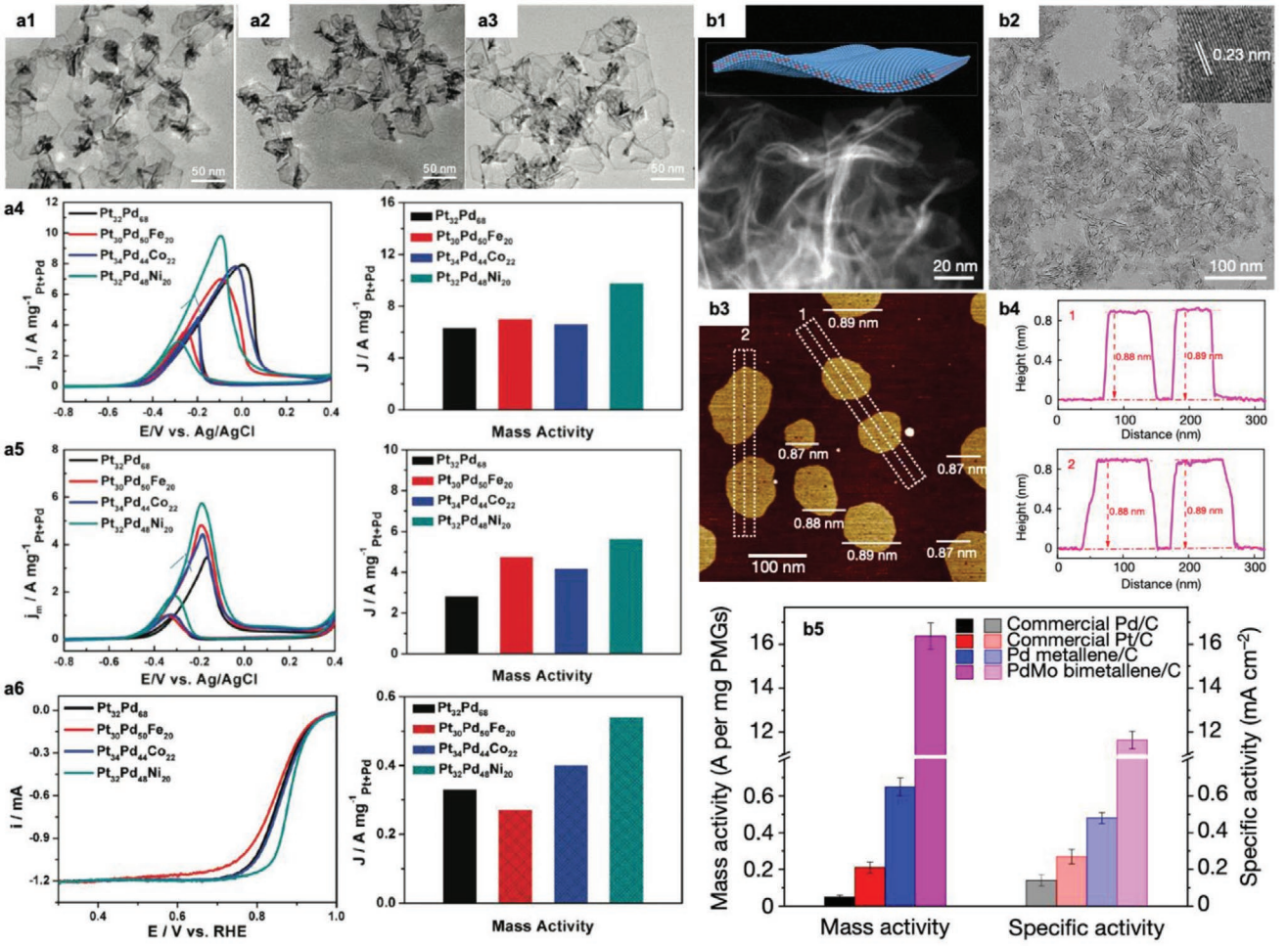

Figure 12. a1–a3) The morphology of $Pt_{32}Pd_{48}Ni_{20}$ $Pt_{30}Pd_{50}Fe_{20}$ and $Pt_{34}Pd_{44}Co_{22}$ and a4–a6) the activity of these catalysts for ethylene glycol oxidation reaction, glycerol oxidation reaction, and ORR.[189] b1–b4) Morphology of PdMo bimetallene and b5) the comparison of the mass and specific activities in 0.1 M KOH at 0.9 V.[138] (a) Reproduced with permission.[189] Copyright 2019, WILEY-VCH. (b) Reproduced with permission.[138] Copyright 2019, Springer Nature.

Figure 13b, by the electron beam lithography patterning, the electrochemical measurement of only the basal plane or only the edges of a single-layer 2D MoS_2 nanosheet can be carried out. It was shown that the decreased contact resistance between the 2H plane and the substrate would significantly facilitate the charge injection into the 2H plane catalyst, triggering the good HER activity.[191] In this work, the 2D WDNs can be used as a precise model catalyst for investigations. Meanwhile, this work supports that the 2H phase of MoS_2 can be a good HER catalyst only if the contact resistance between catalyst and support is low enough to trigger the efficient charge injection (Figure 13b).

Based on the above discussions, the well-defined 2D nanostructured catalysts are very promising in electrocatalytic reactions. It is noteworthy that 2D carbon materials have been widely investigated as catalyst supports.[141] Due to the high surface area and strong affinity of catalytic particles with the 2D supports, the electrochemical surface areas of the catalysts can be significantly enhanced, and the dispersion of catalytic particles can be improved. Moreover, the electronic structure of catalyst particles can be precisely tuned; therefore, the electrocatalytic kinetics will be increased. For example, the graphene has a well-defined 2D nanostructure, and it has been widely investigated as support material for electrocatalysts or directly used as metal-free catalysts after controllable heteroatom doping.

The evaluation of the electrocatalyst is mostly performed in the conventional three-electrode system, which includes the working, counter, and referential electrodes. In such a system, the catalyst layer is relatively thin. However, in a real device, the electrode usually has high electrocatalyst loading and much thicker catalyst layer. Particularly, in some applications, such as fuel cells, to prepare the membrane electrode assemblies (MEA), the catalyst layers need the hot-pressing process to enhance the contact between different phases. Under such conditions, the 2D nanostructure in catalyst layers tends to be stacked. As a result, the stacked 2D nanostructure blocks the active sites on the surfaces and, on the other hand, hinders the reactant transportation and product removal, likely leading to low exposed active site density and large mass transfer resistance.[142] In this regard, intentionally building the 3D nanostructure in both electrocatalysts and electrodes is promising.

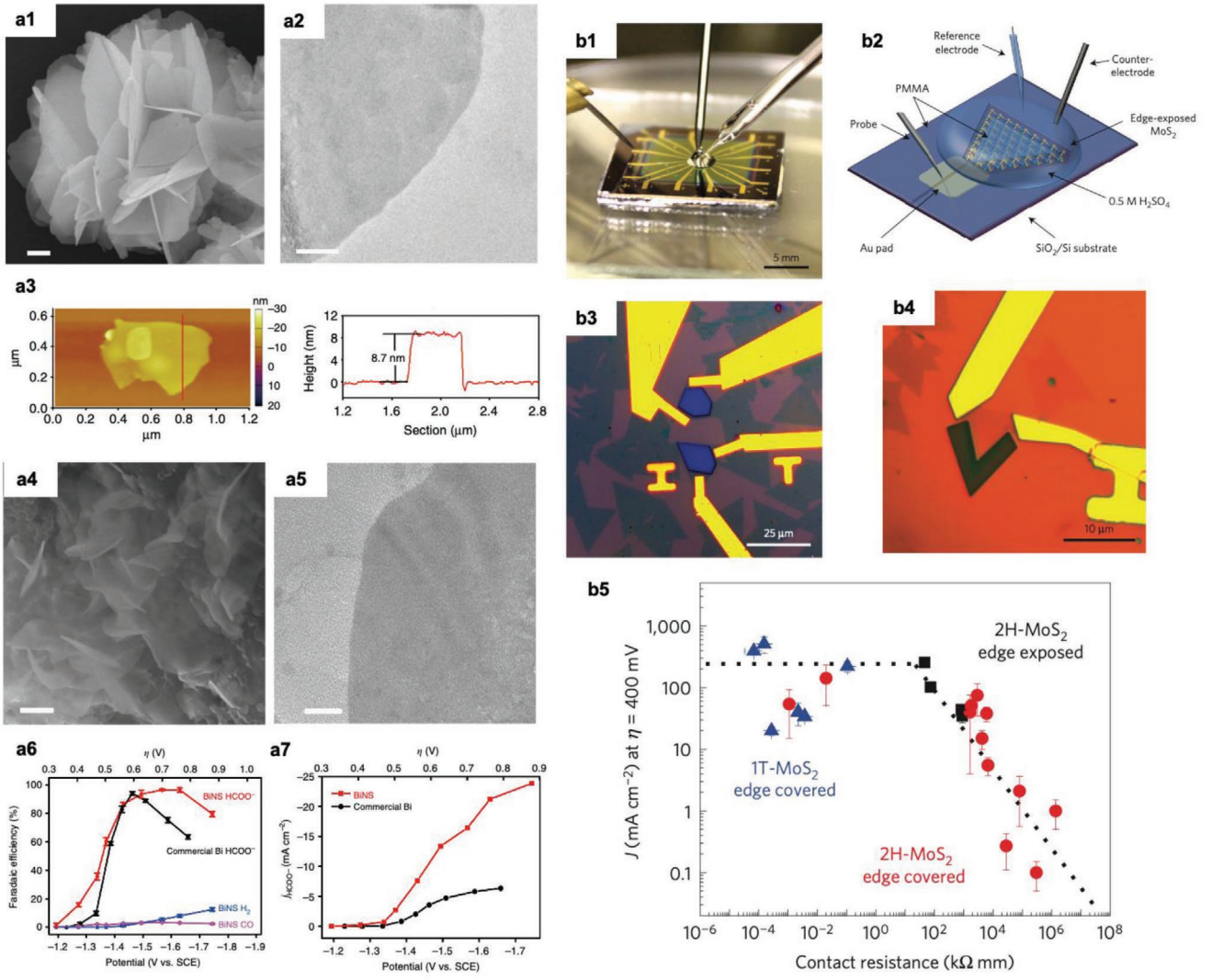

Figure 13. Structural characterizations of a1–a3) BiOI nanosheets and a4,a5) the reduced BiNS; a6,a7) the electrocatalytic performance of CO_2RR on the BiNS and commercial Bi nanopowder catalysts.[190] b1–b4) The microcell for the electrochemical HER measurement using the single-layer MoS_2 with edge covered and exposed; b5) the relationship between HER activity and the contact resistance on different catalysts.[191] (a) Reproduced under the terms of the Creative Commons CC BY License.[190] Copyright 2018, Springer Nature. (b) Reproduced with permission.[191] Copyright 2016, Springer Nature.

4.5. 3D WDNs for Electrocatalysis

The 3D nanostructured materials are highly active electrocatalysts because of their unique skeleton, a large amount of exposed active sites, high atomic utilization, and accessible mass and ion contact.[192] For the electrodes in electrocatalytic devices, the 3D well-defined structures are necessary—all the practical electrodes are designed in 3D structures.

For the Pt-based 3D nanostructures, the starting materials can be 0D Pt-based nanoparticles. Controlled etching is usually used to obtain a well-defined 3D nanostructure. For example, the gradual evolution of the $PtNi_3$ polyhedra is shown in **Figure 14**a. Along with the etching of Ni element, the original $PtNi_3$ polyhedra converted into a Pt-rich Pt_3Ni nanoframe via the PtNi intermediates.[149] Followed by high-temperature annealing, the Pt_3Ni nanoframes with smooth Pt skin supported by carbon were obtained. In such nanostructures, almost all the Pt atoms are utilized. The modulated electronic structure achieved by alloying with Ni promotes the electrocatalytic kinetics, and the unique nanoframe architecture leads to a strain of Pt atoms, facilitating kinetics as well. Furthermore, the open structure provides abundant pathways for accessible reactant species. The Pt_3Ni nanoframes demonstrate significantly enhanced ORR performance with 36-fold in mass activity and 22 times in specific activity (Figure 14a).

By precisely controlling the structures, different morphologies can be achieved. Ref. [193] is an excellent example of synthesizing Pt-based nanocages with subnanometer walls. During the deposition process of a thin Pt layer on the Pd nanocube substrates, the Pd atoms diffused into the Pt layers and formed Pd channels, which provided an efficient Pd dissolution pathway. After the complete Pd etching, Pt-based nanocages were formed

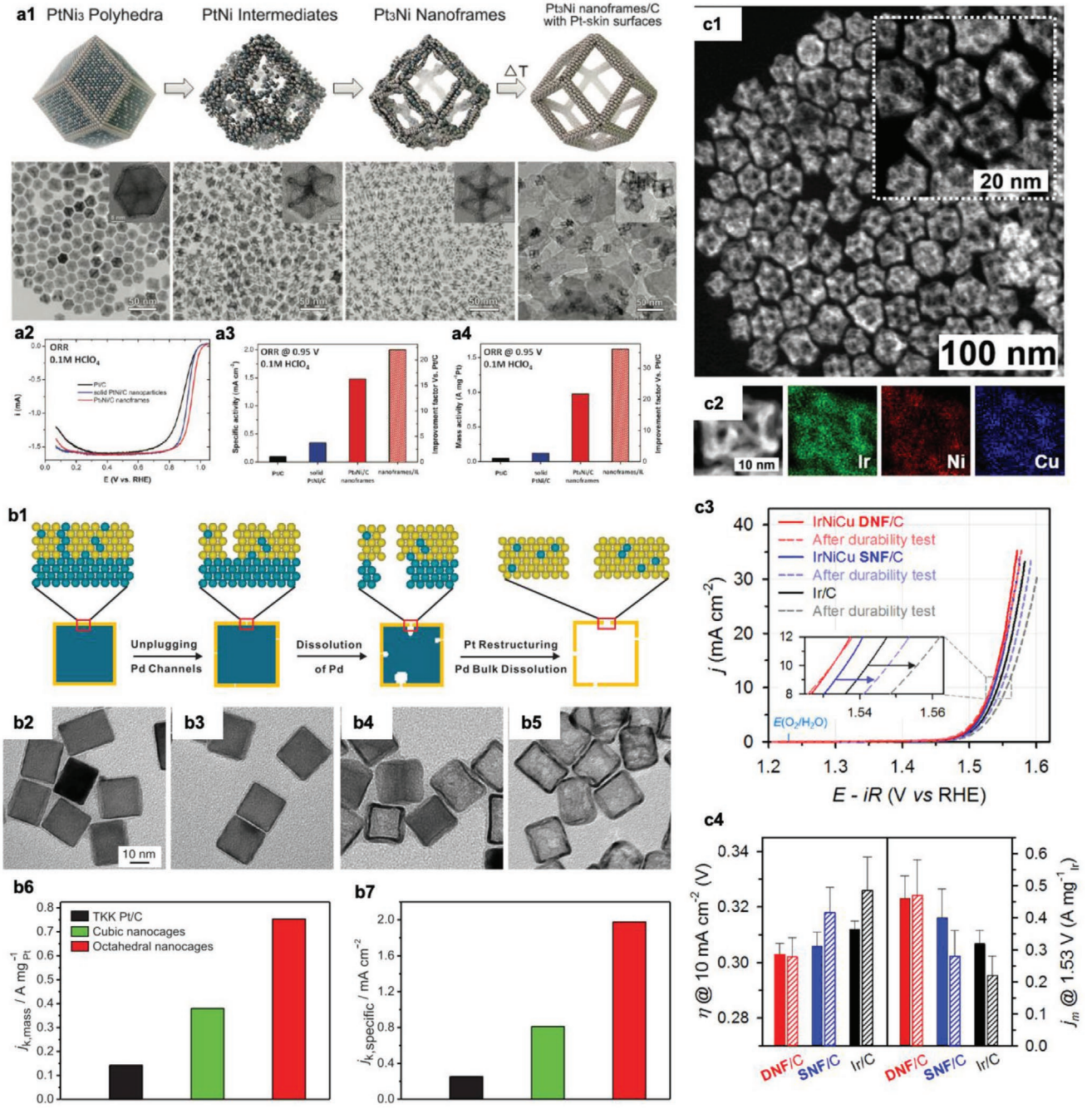

Figure 14. a1) Schematic illustrations and corresponding architecture of the samples obtained at four representative stages during the evolution process from polyhedra to nanoframes; a2–a4) the ORR LSV curves and specific activities and mass activities measured at 0.95 V for Pt_3Ni nanoframes with Pt(111)-skin-like surfaces dispersed on high-surface area carbon.[149] b1) Schematic of the major steps involved in the continuous dissolution of Pd atoms from a $Pd@Pt_{4L}$ cube to generate a Pt cubic nanocage and b2–b5) the corresponding architecture of the $Pd@Pt_{4L}$ cubes after Pd etching for 0, 10, 30, and 180 min; b6,b7) the mass and specific ORR activity for catalysts.[193] c1,c2) Architecture and composition of IrNiCu DNF, as well as c3,c4) its OER activity.[145] (a) Reproduced with permission.[149] Copyright 2014, the American Association for the Advancement of Science. (b) Reproduced with permission.[193] Copyright 2015, the American Association for the Advancement of Science. (c) Reproduced with permission.[145] Copyright 2017, American Chemical Society.

(Figure 14b). If the octahedral Pd nanocrystals were used, the octahedral Pt nanocages could be finally obtained, which demonstrated excellent ORR activity. The well-defined octahedral Pt nanocages show excellent ORR mass activity of 0.75 A mg_{Pt}^{-1} at 0.9 V, which is five times higher than that of Pt/C. The octahedral Pt nanocages exhibit almost eightfold better specific activity than that of Pt/C. Besides, the Pt atoms can also be deposited on the edges of truncated octahedral Au facets, forming truncated octahedral PtAu 3D nanostructure, which exhibited excellent activity for methanol oxidation.[194]

In particular, a unique, well-defined 3D nanoframe@nanoframe architecture (double-layered nanoframe, DNF) can be designed and achieved based on the different decomposition rates of metal precursors (i.e., $Ir(acac)_3$ and $IrCl_3$, Figure 14c).[145] After etching, the trimetallic IrNiCu DNF catalyst presents much enhanced OER activity in 0.1 M perchloric acid electrolyte in terms of either the overpotential at 10 mA cm^{-2} or the current density at 1.53 V compared with the referential Ir/C catalyst.

Other than the metals that can be precisely etched, it is challenging to achieve the carbon-based materials with the well-defined 3D nanostructure. In ref. [195], it was found that the Fe salt inside the ZIF precursor could be reduced and the decomposition of ZIF precursors during pyrolysis then promoted so that a large number of voids were generated. As a result, the hollow porous 3D nanostructure was formed. This catalyst not only showed Pt-like ORR activity in the half cell RDE measurement (half-wave potential of 0.863 V vs Pt/C with 0.858 V, **Figure 15**a), but also demonstrated excellent performance in the practical single MEA fuel cells. This indicates that the 3D structures are beneficial for enhancing fuel cell device performance.

Despite much progress achieved, the 3D porous structure is still difficult to be well controlled. Recently, the hard templates have been employed to precisely control the pore size and distribution. As shown in Figure 15b, the ZIF material was coated by a mesoporous silica template. The silica template not only induced porous structure (high surface area) but also protected

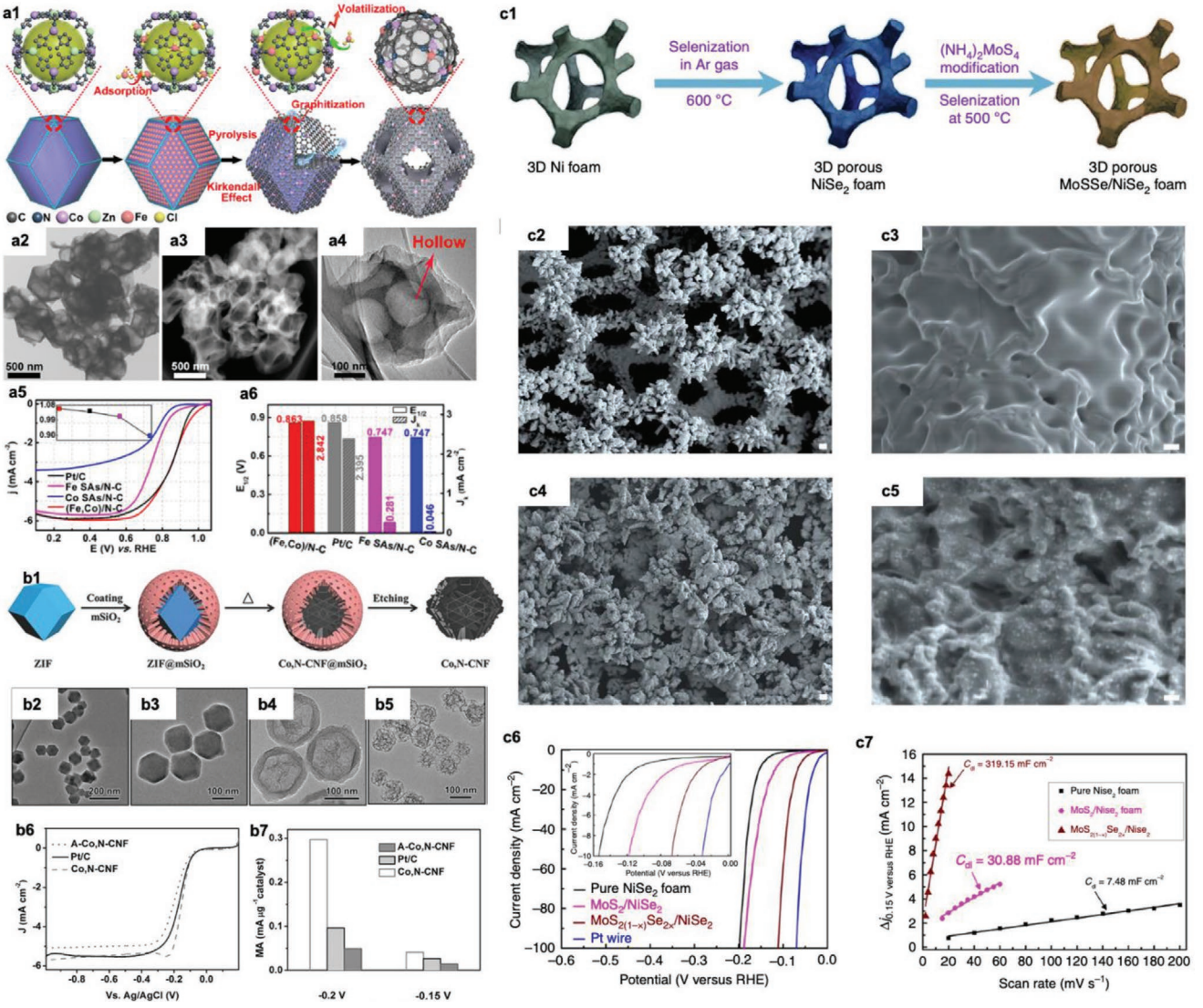

Figure 15. a1) Schematic of the catalyst synthesis and a2–a4) architecture of (Fe,Co)/N-C catalyst; a5,a6) the ORR activity of catalysts.[195] b1) Synthetic procedure of the Co,N-CNF by the $mSiO_2$-protected calcination strategy and b2–b5) corresponding morphology of Co,Zn-ZIF, Co,Zn-ZIF@$mSiO_2$, Co,N-CNF@$mSiO_2$, and Co,N-CNF; b6,b7) ORR activity of catalysts.[196] c1) Synthetic procedure of the growing ternary $MoS_{2(1-x)}Se_{2x}$ particles on porous $NiSe_2$ foam; c2,c3) SEM images of the $NiSe_2$ foam grown at 600 °C; c4,c5) hetero-architecture of the $MoS_{2(1-x)}Se_{2x}$ particles distributed on porous $NiSe_2$ foam grown at 500 °C; c6,c7) the HER performance of the electrodes.[197] (a) Reproduced with permission.[195] Copyright 2017, American Chemical Society. (b) Reproduced with permission.[196] Copyright 2015, WILEY-VCH. (c) Reproduced under the terms of the Creative Commons CC BY License.[197] Copyright 2016, Springer Nature.

the ZIF precursors from aggregation after high-temperature pyrolysis. The silica template can be removed by hydrofluoric acid and the well-defined 3D porous Co,N-CNF catalyst is obtained. As shown in Figure 15b, the silica template-mediated Co,N-CNF catalyst shows the half-wave potential of –0.155 V and the diffusion limiting current density of 5.71 mA cm^{-2}, which are superior to both the silica-free Co,N-CNF catalyst (–0.194 V; 5.09 mA cm^{-2}) and commercial Pt/C catalyst (–0.175 V; 5.69 mA cm^{-2}).[196]

The 3D structures in electrocatalysis should be considered at different levels. One is at the catalyst level and another one is at the electrode level. In Section 4.3, the advantages of 1D nanostructures in electrodes have been discussed. Actually, such type of 1D arrays plus 2D substrate can be regarded as the 3D electrodes. Similarly, the 0D nanocatalysts usually require loading on support materials to finally form a 3D nanostructure in catalyst layers in practice. In ref. [197], the Ni foam was employed as the 3D substrate to grow the catalysts. As shown in Figure 15c, the electrode presented a well-defined 3D porous structure, which is beneficial for enhanced HER performance. The Ni foam as a popular template with a well-defined 3D nanostructure can be widely used as the substrate to load or grow the desired catalysts, forming the controllable nanostructures. The 3D nanostructures could be very important in designing the catalyst layers for related electrocatalytic devices.[198–200]

4.6. WDNs for Photoelectrocatalysis

As indicated in the early chapter, in addition to the conversion of solar energy into electrical energy, which will be handled by electrocatalysis and metal–air battery, the solar energy can also be directly employed to generate electrons and holes.[201] Photoelectrocatalysis has emerged as a promising powerful tool for various catalytic applications by combining photocatalytic and electrolytic processes. It consists of the promotion of electrons from the valence band to the conduction band of a semiconductor photocatalyst upon light irradiation, with the production of positive holes. The fast recombination of the electron–hole pairs formed is avoided in photoelectrocatalysis by applying an external bias potential to the photocatalyst that extracts the photogenerated electrons up to the cathode of the electrolytic cell.[202] The ultimate performance of the photoelectrocatalysis is primarily determined by the light absorption and the utilization rate of photogenerated electrons and holes. Therefore, to achieve efficient solar energy conversion, it is necessary to enhance the light trapping capability and meanwhile suppress the electron–hole recombination before participating in a chemical reaction by modulating the material's intrinsic property or introducing physical effects (e.g., surface plasmon resonance [SPR], band engineering, etc).[87,203–206] Compared with conventional bulk devices, WDN-based devices demonstrate unique advantages in both aspects. In the following discussions, we will focus on the strategies to enhance solar energy conversion by using WDNs.

The indispensable component for photo(electro)catalysts is the semiconductor material with response to the illumination. Improving the performance of semiconductors is important to meet the requirements of photoelectrocatalysis. Titanium dioxide (TiO_2) is one of the most commonly used photoelectrocatalysis materials, which, however, suffers from poor light absorption capability and low electrical conductivity. To modulate its photoelectrocatalysis performance, 0D nanoparticles have been employed and demonstrated promising performance because of their high surface-to-volume ratio. By introducing defects into the high-density surface atoms during the hydrogen plasma treatment, the intrinsic light absorption property of TiO_2 was modulated, which can be directly observed by the color variation from white to gray and black (**Figure 16**a).[207] The slightly hydrogenated TiO_2 demonstrates optimal photoelectrocatalysis performance which can be attributed to the reduced electron–hole recombination rate caused by the introduced surface defects. This mechanism is also applicable to TiO_2 nanostructures with other dimensions such as 1D nanowires and nanotubes. Due to the efficient charge separation and transportation, hydrogenated TiO_2 NWs, as shown in Figure 16b, demonstrated a very low photocurrent saturation potential of –0.6 V versus Ag/AgCl. Accordingly, a photocurrent density of about 1.97 mA cm^{-2} was obtained with an external bias of 0.6 V versus Ag/AgCl in 1 M NaOH solution illuminated by simulated AM 1.5G solar spectrum (Figure 16b).[208] In addition to suppressing the electron–hole combination by controlling the surface defects, tuning the intrinsic light-trapping capability of TiO_2 is also in favor of boosting the solar energy conversion. Park et al. found that the incorporation of carbon into TiO_2 nanotubes by heating in a CO atmosphere could narrow the bandgap, which successfully extended the light absorption spectrum into the visible light spectrum range and gave rise to obvious photoelectrocatalysis response beyond 420 nm (Figure 16c). More importantly, these photoelectrocatalysis performances can be further enhanced in conjunction with controlling the geometrical features of nanostructures. Taking the length modulation of nanotubes as an example, prolonging nanotubes from 0.7 to 3.3 μm resulted in a monotonic increase for the photocurrent densities, which reach the maximum for the nanotubes with 3.3 μm length (Figure 16c).[209] Another example is the top-opened ZnO/CdS/PdS nanotube array electrode. The successive ionic layer adsorption reactions were efficient to open the nanotube tops, as shown in Figure 16d.[210] The top-opened ZnO/CdS/PdS nanotube electrode demonstrated a hydrogen production rate of 5.5 mL cm^{-2} h^{-1} at 0 V (vs Ag/AgCl), indicating that the opened architecture is promising for use as the photoelectrode. The opened architecture as a photoanode not only increases the surface area for light absorption but also provides abundant channels for mass transfer. These investigations indicate that material treatments to reduce the bandgap or alleviate recombination can be combined with the controlling of geometrical features to maximize solar energy conversion. All the above results are universal for the device design with 2D and 3D WDNs for the solar energy conversion. As shown in Figure 16e, the establishment of 2D hybrid nanosheets leads to an interface between α-Fe_2O_3 and g-C_3N_4, which simultaneously allows the efficient transfer of the electron in g-C_3N_4 to the active site, effective electron–hole recombination suppression in both α-Fe_2O_3 and g-C_3N_4, and fast electron transport from the conduction band of α-Fe_2O_3 to the valance band of g-C_3N_4. These unique advantages

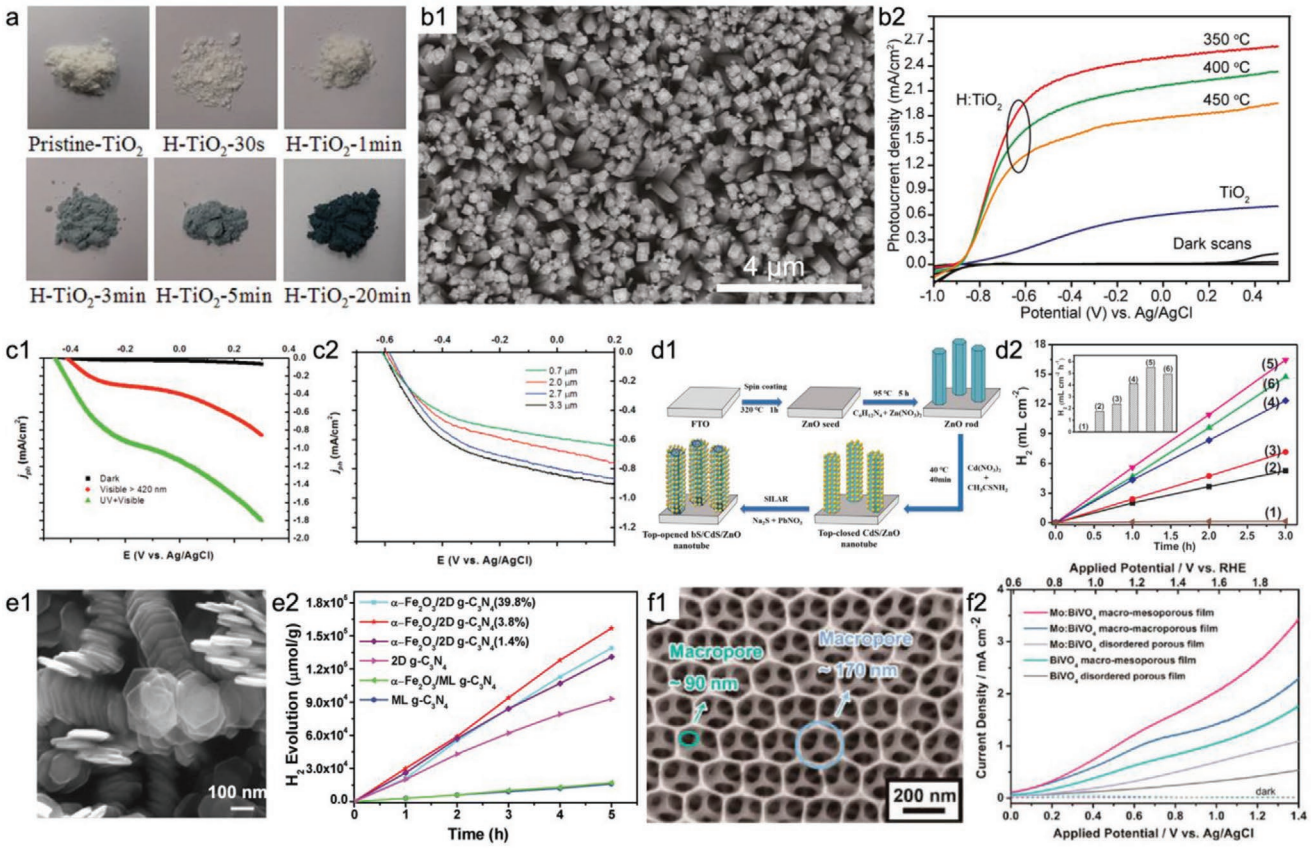

Figure 16. a) Photographs of the pristine-TiO_2 and H-TiO_2 0D nanoparticles prepared by H_2 plasma treatment after 30 s, 1 min, 3 min, 5 min, and 20 min.[207] b1) SEM image of 1D TiO_2 nanowire arrays; b2) photocurrent densities of pristine TiO_2 nanowires and H:TiO_2 nanowires annealed at different temperatures.[208] c1) Photocurrent densities of 1D carbon-doped TiO_2 nanotube array in the dark and under the illumination of visible light and white light; c2) variation of photocurrent density as a function of TiO_2 nanotube length.[209] d1) Synthesis procedures of the top-opened ZnO/CdS/PdS nanotube electrode; d2) the photo-hydrogen production rate on catalysts.[210] e1) SEM image of hexagonal 2D α-Fe_2O_3 nanosheets; e2) photocatalytic H_2 evolution using carbon-nitride-based hybrid nanostructures illuminated by visible light.[211] f1) SEM image of Mo:$BiVO_4$ 3D-ordered macro-macroporous nanostructures; f2) photocurrent densities of various 3D-ordered nanostructures.[212] (a) Reproduced with permission.[207] Copyright 2014, The Royal Society of Chemistry. (b) Reproduced with permission.[208] Copyright 2011, American Chemical Society. (c) Reproduced with permission.[209] Copyright 2006, American Chemical Society. (d) Reproduced with permission.[210] Copyright 2019, Elsevier. (e) Reproduced with permission.[211] Copyright 2017, WILEY-VCH. (f) Reproduced with permission.[212] Copyright 2014, American Chemical Society.

greatly promoted the H_2 evolution to achieve a high rate of 31 400 μmol g^{-1} h^{-1} and prominent external quantum efficiency of 44.35% under an illumination of 420 nm wavelength (Figure 16e).[211] Besides the above advantages for 0D–2D WDNs, the 3D highly ordered mesoporous WDNs have a more compact space occupation of an active semiconductor due to a larger interstitial space (Figure 16f). The compact configuration leads to significantly reduced carrier-transport resistance in the electrode, the contact resistance at the electrode/electrolyte interface, and the electrode/current collector junction. Moreover, the uniform channel is particularly desirable for the elimination of as-produced O_2. In conjunction with the material regulation, the charge migration in Mo:$BiVO_4$ was further enhanced which, together, resulted in significantly enhanced photoelectrocatalysis photocurrent densities (Figure 16f).[212]

In addition to engineering semiconductors into WDNs, the integration of auxiliary constituents into the semiconductor to form hetero-architectures provides an alternative route to enhance the photoelectrocatalysis performance. Among them, noble-metal (e.g., Au, Ag, Cu, etc) integrated WDNs have been widely exploited because the SPR effects can both improve the solar light absorption and increase the utilization rate of photogenerated electrons and holes.[213] In particular, the optical response of SPR is highly dependent on the geometries of the metals in the WDNs, thus endowing a versatile platform to modulate photoelectrocatalysis performance.

For correlating the size contribution with the light absorption capability in photocatalysis, 0D nanoparticles were selected as a model. The investigation on the size effect requires well-defined size distribution. By a direct contact printing strategy, the 0D Au nanoparticles could be successfully controlled in three narrow size distributions, that is, 50 ± 5%, 63 ± 5%, and 83 ± 5% nm (**Figure 17**a). Accordingly, the photocurrent density of photoelectrocatalysis water splitting increased with the decrease of the Au NP size (Figure 17a), which could be attributed to the increased local field enhancement and increased formation rate of photogenerated electrons and holes.[214] The precise controlling over

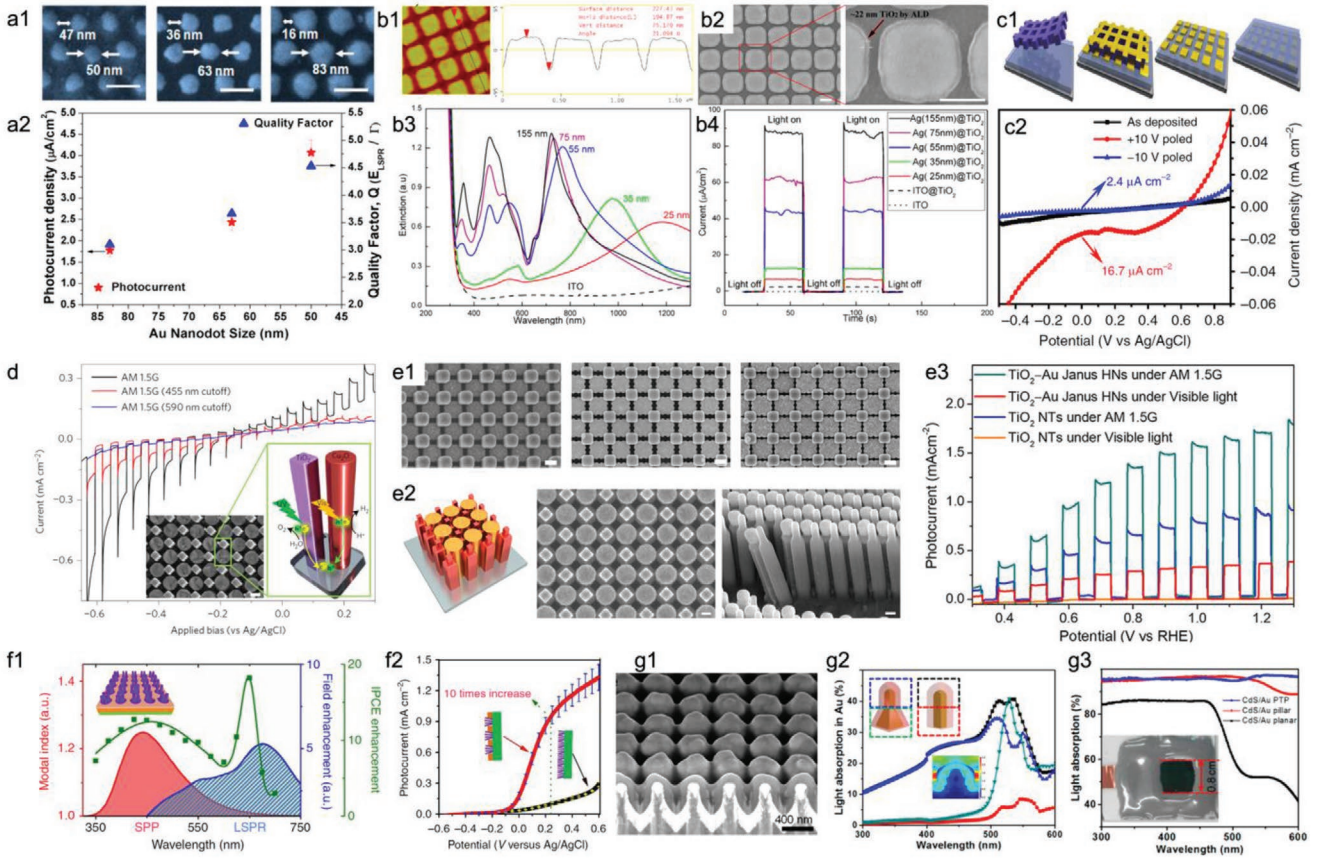

Figure 17. a1) Morphology of 0D Au nanodot arrays with controlled size; a2) size effect of Au nanodot arrays on the performance. Scale bars: 100 nm.[214] b1) AFM height characterization of 0D Ag nanoparticles; b2) SEM images of nanoparticles after coating with a conformal TiO_2 layer; b3) optical extinction spectra of Ag nanoparticles (with different heights of about 25, 35, 55, 75, and 155 nm); b4) photocurrent densities of Ag/TiO_2 photoelectrodes. Scale bars: 200 nm.[215] c1) Schematic illustration of fabrication processes for plasmonic-ferroelectric hybrids; c2) the photocurrent densities of the as-grown (black), +10 V (red), and −10 V (blue) poled samples under the filtered white-light excitation.[216] d) Chopped photocurrent densities of a 1D TiO_2 nanotube/Cu_2O nanowire binary-electrode.[80] e1) 1D TiO_2 nanotube/Au nanowire arrays with different shapes; e2) binary nanostructures with two different sizes in each constituent; e3) photocurrent densities of binary electrodes and TiO_2 nanotube reference. Scale bars: 200 nm.[217] f1) Waveguiding efficiency, local field enhancement, and IPCE enhancement for hematite nanorods grown into a 2D gold nanohole array; f2) photocurrent densities.[102] g1) Cross-sectional SEM of a 3D CdS/Au PTP array; g2) FDTD simulated light absorption in the top and bottom parts of Au PTPs and pillars, and the electric field distribution at 550 nm wavelength; g3) light absorption spectra and photo of a typical CdS/Au PTPs.[92] (a) Reproduced with permission.[214] Copyright 2014, American Chemical Society. (b) Reproduced with permission.[215] Copyright 2015, American Chemical Society. (c) Reproduced under the terms of the Creative Commons CC BY License.[216] Copyright 2016, Springer Nature. (d) Reproduced with permission.[80] Copyright 2016, Springer Nature. (e) Reproduced with permission.[217] Copyright 2018, American Chemical Society. (f) Reproduced with permission.[102] Copyright 2013, Springer Nature. (g) Reproduced with permission.[92] Copyright 2017, American Chemical Society.

nanoparticle height is another strategy for tuning the influence of SPR in photocatalysis (Figure 17b). By altering the nanoparticle heights, the SPR is shiftable in a broad spectrum that covers ultraviolet, visible, and near-infrared regions. With the increase of the nanoparticle height, the dipolar SPR mode demonstrated obvious blue-shift from the near-infrared to the visible region as well as intensity increasing (Figure 17b). Meanwhile, multipolar SPR modes began to arise in the ultraviolet and visible range for these higher nanoparticles. Due to the increased intensity and multipolar modes, the photocurrent of TiO_2 photocatalyst demonstrated a decent increase from 2.5 to 90 μA cm^{-2} (Figure 17b).[215] The SPR-induced photoelectrocatalysis enhancement was also observed in a ferroelectric material $Pb(Zr,Ti)O_3$ (PZT). Due to an effective charge transfer between the plasmonic nanoparticles and PZT as well as the ferroelectric polarization controlling in PZT, the photocurrent density was increased by nearly an order of magnitude (Figure 17c).[216]

Compared with the 0D nanoparticles, the 1D nanostructures offer more geometrical modulation possibility; thus, richer optical properties are highly expected from the 1D plasmonic nanostructures. To fully exploit the aforementioned advantages of the semiconductor and plasmonic nanostructures, the control of the geometries of both nanostructures simultaneously is needed. Recently, a new type of multi-pore AAO template was developed to address this challenge.[80] Through the sequential pore-opening process, two different materials can be deposited into two sets of pores. As shown in Figure 17d, a matrix combining arrays of 1D Cu_2O NWs and TiO_2 NTs were constructed, forming a unique Z-scheme photoelectrocatalysis

cell. More importantly, such multi-pore templates are easy to control, separately, the geometries (e.g., size and shape) of two sets of pores which impart geometrical tunability to the replicated nanostructure counterparts. Taking the Au/TiO_2 system as an example, Figure 17e shows the combinations of different shapes and sizes in which the Au NWs are altered from four-cross to eight-cross in shape.[217] In combination with a two-step anodization process, the synthesis offers higher degrees of control for two constituents, including shapes, sizes, and compositions (Figure 17e). Impressively, the optimal TiO_2/Pt-Au WDNs demonstrated a 4.6 times higher HER rate than that of using TiO_2 nanotubes (Figure 17e).

Limited by the narrow-band response for a specific SPR mode, the photoelectrocatalysis contribution of SPR stemming from 0D and 1D plasmonic nanostructures is limited when considering the broadband solar spectrum. To address this challenge, scientists have turned their focus upon 2D and even 3D nanostructures. Li et al. incorporated the hematite nanorods into a 2D gold nanomesh consisting of arrayed nanoholes.[102] Figure 17f shows that the SPR effects excited in the 2D gold nanomesh take roles in two different wavelength regions: one is below the band edge where SPR-induced resonant energy transfer promotes light trapping, and the other is above the absorption band edge of hematite where the surface plasmon polarization launches a guided wave mode along the hematite nanorod. Because of the complementary effect between the two resonance modes in a broad wavelength range, the light trapping capability of the hematite and the photoelectrocatalysis water splitting performance was greatly enhanced. For example, the photocurrent density at 0.23 V (vs Ag/AgCl) demonstrated an approximately tenfold increase under the illumination of a simulated solar spectrum (Figure 17f). The 3D plasmonic nanostructures also demonstrate broadband function. Proof-of-concept 3D Au pillar/truncated-pyramid (PTP) arrays were constructed and the CdS/Au PTP photoanode was used to unravel the spectrally synergistic complementation in solar energy harvesting (Figure 17g).[92] Compared with the Au pillar photoanode in which plasmonic resonance is localized at the top part, the CdS/Au PTP photoanode can excite SPR in both the top pillar and the bottom pyramid (Figure 17g). As expected, these SPR modes function in different wavelength ranges given the high nanostructure-shape dependency of the SPR response. Benefiting from the SPR near the bandgap wavelengths of CdS and the photonic modes in short-wavelength range, the CdS/Au PTPs demonstrated high light adsorption of ≈95% in the wavelength range between 300 and 600 nm (Figure 17g) and accordingly achieved a photocurrent enhancement of ≈400% relative to the planar reference.

Based on the above discussions, the dimensionality (in the combination of the size, shape, hetero-architecture, and spatial arrangement) of the electrocatalysts and photoelectrocatalysts, and the corresponding electrodes greatly determine the performance of related practical energy devices. Through constructing the WDNs from 0D to 3D, the intrinsic activity, active site density, mass transportation rate, as well as the photoresponse capability can be reasonably facilitated. Accordingly, excellent electrocatalysis and photoelectrocatalysis performances for various reactions are achieved.

5. Well-Defined Nanostructures for Energy Storage (Metal-Ion Batteries and Supercapacitors)

Well-defined nano-structuring of functional energy materials is focused on the controlled manipulation of the geometric properties such as the size, shape, hetero-architecture, and spatial arrangement. These WDNs can be either 0D, 1D, 2D, or 3D, and this can be achieved by using different fabrication techniques discussed in Section 3 of this review. Over the years, the chemistry of nano-structuring has proven to play a pivotal role in improving the performance of the energy storage devices and overcoming the issues related to material design in rechargeable batteries and supercapacitors.[218] By considering the theoretical capacity of materials in rechargeable batteries, the choice of electrode materials used in a battery system dictates its performance and large-scale industrial applications. However, the significance of the architecture, dimensionality, surface area, and pore-size distribution of the materials at the nanoscale level must not be overlooked. Specifically, the structural design of an electrode material significantly impacts its performance and electrochemical behavior in a rechargeable battery.[219] Nanostructured materials provide various unique advantages in rechargeable battery systems such as flexible morphology, large specific surface area with shorter ionic and electronic transfer distances, superior conductivity, and effective face-to-face contact with the current collector (see **Table 2**).[220] Furthermore, due to their high surface to volume ratio, nanoscale electrode materials experience the in situ formation of an electrode-electrolyte interface which ensures better electrolyte contact for rapid ionic and electronic transport.[221] Moreover, the problem of pulverization and electrode destruction experienced by several battery electrodes can be mitigated by designing a well-defined nanostructured material such as a core–shell structure. Also, the crystallographic modification of some electrode materials for improved battery performance may be essential in large-sized alkali metal ion battery systems such as K-ion and Al-ion batteries. By using the appropriate synthesis method, such modifications can be made at the nanoscale level as this may be impossible to achieve at the bulk level. Likewise, while some electrode materials are limited by ineffective adsorption of ions, others are hindered by the desorption of the adsorbed alkali ions. This problem is often caused by extremely high adsorption energy of alkali-metal atoms, thereby resulting in inefficient intercalation/deintercalation.[19] Through strategic and innovative synthesis methods, designing a WDN of such electrode material can solve this problem. Congruently, the solid electrolyte interphase (SEI) is an essential part of the ionic storage mechanism in rechargeable batteries; due to the effective surface interaction achieved by nanostructured materials, it is possible to optimize the SEI layer. In addition, the need for a fast-charging battery system for the development of electric vehicles can be achieved through nano-structuring due to increased ionic diffusion rate and reduced diffusion path; they foster increased charge/discharge rate.[222] To this end, active materials in rechargeable batteries can be optimally utilized to achieve high performance by fabricating WDNs.

In other to maintain a balanced overview of nanostructured materials and their impact on rechargeable battery electrode

Table 2. The benefits and limitations associated with the application of each category of WDNs in energy storage devices.

0D	1D	2D	3D
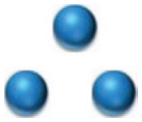		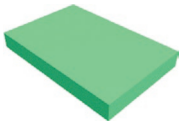	
Benefits for application in energy storage devices			
Improved mechanical strength[223]	Flexible freestanding structure[224]	Large surface area[225]	Improved metal ion accessibility[226]
Shorter alkali ion diffusion length[227]	High aspect ratio[228]	Good electrical conductivity[229]	Minimized diffusion limitations and improved electrolyte penetration[230]
No bulk solid-state diffusion[231]	Efficient electron transport along and through the 1D geometry[232]	A large number of accessible electrochemically active sites[233]	Higher surface-to-volume ratio[234]
Easy electrolyte accessibility[235]	Facile strain relaxation[236]	Surface and interlayer storage of large-sized metal ions[237]	Effective absorption of electrode strain[226]
Limitations for application in energy storage devices			
Low dimensionality/surface area[238]	The tightly interconnected configuration could impede Li ion diffusion and strain relaxation[236]	Consumption of large amounts of electrolyte[239]	Possibility for side reactions due to large surface area[240]
Low tap density/limited active sites[241]	Poor mechanical property[242]	Parasitic reactions related to electrolyte decomposition[243]	Complicated synthesis method[244]
Agglomeration[245]	Low coulombic efficiencies caused by continuous formation of the SEI film[246]	Restacking and aggregation[247]	Thicker electrode often leads to increased resistance[248]
Poor chemical stability[249]	Low tap density[250]	irreversible capacity loss in the first cycle due to SEI formation[251]	Large consumption of electrolyte resulting in electrode flooding[252]

design, we must also highlight the fact that some challenges have also been encountered (see Table 2). First, due to the improved interactions at the surface of the electrode and its larger surface area, the possibilities for the side reactions and the formation of insulating layers which could inhibit effective ionic transport is very high. Also, due to their nano-size, most nanostructured electrode materials suffer from low tap density, which often impacts their volumetric capacity, initial columbic efficiency, and cycle life. This often limits their large-scale industrial applications and requires them to be coated by other conductive materials such as graphene or highly conductive carbon.[219,253] Other issues related to WDNs electrode materials include the formation of unstable SEI layer, irreversible consumption of alkali-metal ions, volume changes, which results in structural changes and loss of electrode, and severed attachment to the current collector after several cycles. All these issues severely impact the coulombic efficiency, cycle life, and capacity retention of WDNs.[222]

In this section of the review, we shall focus on some highly relevant works that have applied the concept of well-defined nanostructured electrode materials for rechargeable batteries. Although the improvements in rechargeable batteries can be approached from the anode and cathode, tunability of the anode for improved performance and energy density is more feasible.[219,254] To this end, this will be the focus of this chapter, specifically, a focus on the structural parameters (size, shape, hetero-architecture, and spatial arrangement) of well-defined nanostructured anode materials and how these properties positively impacted the storage of alkali-metal ions. For simplicity, these innovative nanostructured electrode materials will be grouped into three categories based on the ionic reaction mechanism: carbon-based (insertion), alloys (alloying), transition metal oxide (conversion) based WDNs and silicon for rechargeable batteries, and supercapacitors (**Figure 18**).

5.1. Carbon-Based WDNs

Carbon-based materials, characterized by the excellent reversible cycle, super stability in chemical, electrochemical and thermal conditions, ease of availability, and low cost,[256] are important components in Li-ion batteries. Presently, the anode materials of commercial LIBs are primarily made of graphite, but its limited theoretical capacity is a major drawback associated with graphite-based LIBs.[257] Due to this limitation, several approaches have been made to improve the performance of carbon-based materials such as tuning of its morphology and dimension. Carbon can be fabricated into different nanostructures such as 1D carbon nanofibers, nanotubes, and nanorods; 2D carbon nanosheets; and 3D carbon nanospheres. Precisely, the design of 2D graphene and 1D carbon nanotubes (CNTs) displayed the possibility of fabricating carbon materials with improved electronic properties. CNTs possess high surface area, superior electronic conductivity, high mechanical, and thermal stability. CNTs provide an interesting advantage to rechargeable batteries because the storage of alkali metal ions can occur at their internal and external walls, and ions can transport through the electrode materials.[258,259] Graphene is regarded as a super material for batteries because of its extremely large surface area with several active sites for alkali-metal ion storage, both sides of the sheet can be used for ion storage, flexibility, defect rich pores, functional groups on its oxide form, and

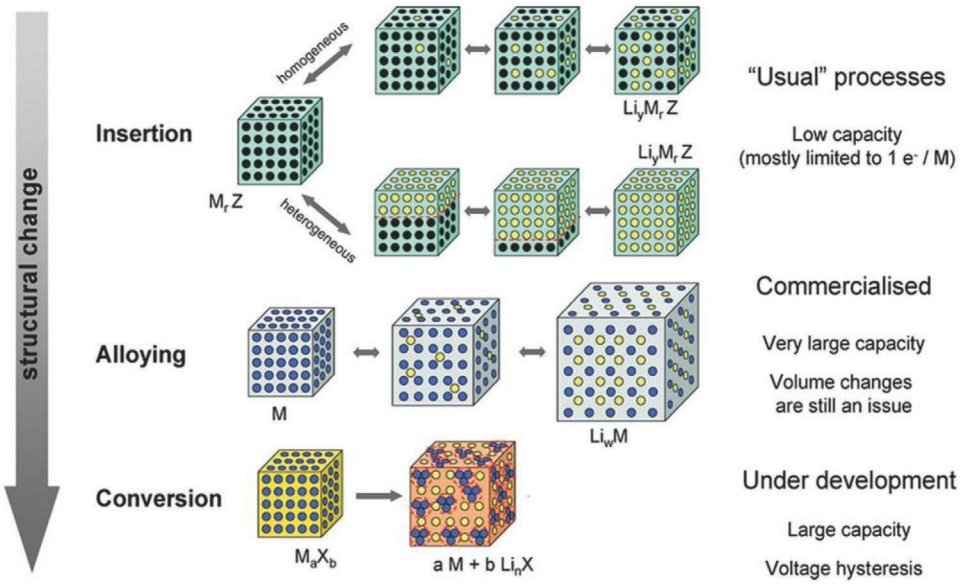

Figure 18. A schematic representation of the different classes of electrode materials based on WDNs and their reaction mechanism in Li-ion batteries. Black circles in the cubes represent vacant spaces for alkali metal-ion storage in the crystal structure. Blue circles represent metals, while yellow circles represent adsorbed Li^+. Reproduced with permission.[255] Copyright 2009, Royal Society of Chemistry.

faster electronic and ionic transport. Despite these functional properties, carbon materials, including CNTs and graphene, are limited in their application for LIBs because they suffer from a very large capacity loss at the first cycle, poor initial coulombic efficiency, and large voltage hysteresis.[260] Pure nanostructured carbon-based materials are often used as a conductive/protective layer on the surface of LIB active materials to accommodate for volume changes during cycling, to prevent surface side reactions between the active materials and electrolyte, and to inhibit the pulverization of electrodes.[253] Hence, researchers have focused on different strategies to improve the conductivity and LIB performance of carbon materials.

WDNs have been employed to large-sized alkali metal ion batteries such as sodium and potassium ion batteries. Due to their enlarged interlayer distances and disoriented structures, carbon materials have proven to be effective for large-sized alkali-metal ion storage. Nano-structuring of the carbon materials facilitates the optimum transport and storage of Na^+ and K^+ ions. Liu et al. designed a ternary composite based on the interpenetrating effect of pillars by infusing MoS_2 deposited carbon nanofibers into graphene architecture to form a MoS_2@CNFIG hybrid electrode for SIBs (**Figure 19**a). This is an excellent example of the fabrication of WDNs via the spatial arrangement of 1D nanowire and 2D graphene sheets. The SEM image in Figure 19b shows that the carbon nanofibers have a uniform 1D shape with an average diameter of 1 µm. The 2D-graphene oxide sheets were also dispersed, exhibiting large size domain (Figure 19c). From the SEM of the hybrid architecture (Figure 19d), it is obvious that the carbon nanofibers were effectively interpenetrated into the large 2D-GO sheets with sufficient spacing between each fiber. The rationale behind this design is that the problem of restacking often encountered by 2D-graphene sheets can be avoided by interpenetrating them with carbon nanofibers. Also, these carbon nanofibers assist in rapid electronic and ionic transfer in the composite. The controlled insertion of the carbon nanofibers into the layers of the graphene sheets displays a sophisticated level of WDN engineering to optimize the sodium-ion battery performance. When applied as a SIB anode material, the MoS_2@CNFIG hybrid electrode delivered an exceptional reversible capacity of 412 and 366 mAh g^{-1} after 1000 cycles when cycled at 1 and 5 A g^{-1}, respectively, (Figure 19e) and displayed excellent rate capability even when tested in a full cell battery.[261] An effective way of modulating the electronic conductivity and battery performance of the carbon materials is by doping, which usually involves either replacing carbon atoms from its structure with a heteroatom or doping the foreign atom into its crystalline structure or surface.[262] A common example of doping in carbon materials is the nitrogen-doped carbon, for example, N-doped graphene. Ji et al. reported the assembly of a 3D graphene doped with nitrogen; due to the 3D architecture and improved conductivity as a result of N-doping, an improved LIBs performance was recorded. However, it still suffered from low initial coulombic efficiency and capacity loss.[263] Doping with lower electronegative heteroatoms, for example, phosphorus, boron, oxygen, and sulfur, can also modify the ionic and electronic conductivity of carbon materials. The work of Zhang et al. showed that due to the large atomic diameter of phosphorus and lower electronegative heteroatoms when compared to nitrogen, P-doped graphene displayed superior conductivity and electrochemical performance.[264] By interrupting the electron cloud of the graphitic carbon and shifting its Fermi level toward the conductive band, doping of heteroatom into carbon materials can elevate its electronic properties and boost LIB performance. Doping also creates defects in the pores of carbon, thereby facilitating the electron transport along its plane.[177] Moreover, manipulating the defects at a material surface is also crucial to regulate the charge transfer behavior at the electrode/electrolyte interface. A good example is the work of Xu et al., who reported the controlled synthesis of an N-doped carbon nanofiber

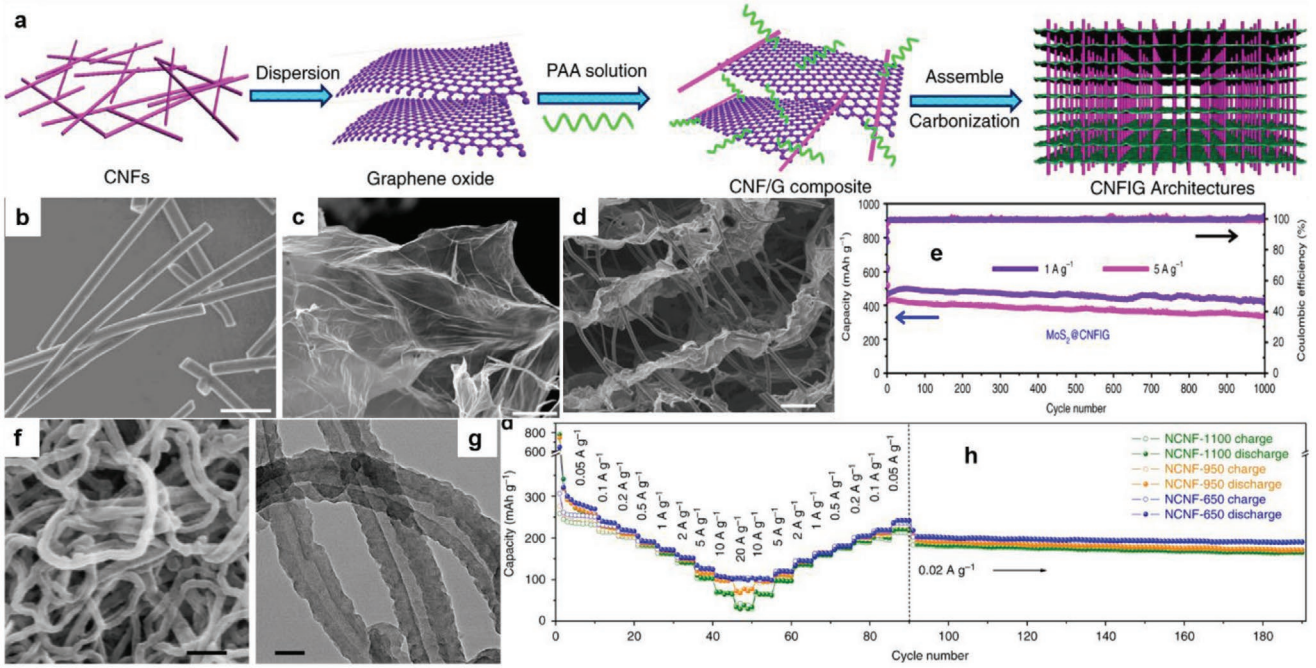

Figure 19. Schematic illustration of the fabrication of WDNs via the spatial arrangement of 1D nanowire and 2D graphene sheets: a) The synthesis of ultra-stable CNFIG architecture based on CNFs and graphene sheets; SEM images of b) CNFs (scale bar = 5 µm) and c) GO sheets (scale bar = 5 µm); d) SEM images of CNFIG architectures at high magnification (scale bar = 10 µm); e) long-term cycling performances of MoS_2@CNFIG at 1.0 and 5.0 A g^{-1}. Reproduced with permission.[261] Copyright 2019, Nature Communication. f) SEM and g) TEM images of NCNF-650. h) Rate performance of different N-doped carbon nanofibers (NCNFs) at current densities ranging from 0.05 to 20 A g^{-1}. Reproduced with permission.[265] Copyright 2018, Nature Communication.

(13.8% nitrogen). By using nitrogen-rich polypyrrole as the precursor for the synthesis of the N-doped carbon nanofiber, it contained a high concentration of pyrrolic and pyridinic nitrogen, which are favorable for K^+ attraction into the carbon matrix. Through hetero-atom doping and oxygen vacancies, abundant surface defects were successfully created. The SEM image (Figure 19f) of the as-synthesized N-doped carbon nanofibers shows they were well cross-linked, and the rough surface confirms the structural defects, which is beneficial for KIBs application. The TEM image (Figure 19g) of the nanofiber displays its hollow nature, which suggests the multi-directional transport of electrons and ions through the fiber. Nitrogen doping in carbon nanofibers creates defects in graphene layers and highly reactive nitrogen sites simultaneously, both of which can highly increase the ion absorption energy and result in surface-dominated K-storage. The N-doped carbon nanofibers displayed their resilience during rate cycling because at ultrahigh current densities of 10 and 20 A g^{-1} it retained up to 104 and 101 mAh g^{-1} (Figure 19h). A full-cell PIB using these nitrogen-doped carbon nanofibers delivers a high reversible capacity of 195 mAh g^{-1} at 0.2 A g^{-1} with an energy density of 130 Wh kg^{-1}, which is comparable to commercial lithium-ion batteries.[265]

Although doping (especially nitrogen doping) has proven to be an effective way to improve the properties and performance of carbon materials for rechargeable batteries, other nitrogen-rich carbon materials have also garnered interest, and one such material is graphitic carbon nitride (g-C_3N_4). Nitrogen doping of carbon materials is often achieved by either in situ doping or post-synthesis treatment via the CVD method; however, these methods only provide a controlled and limited quantity of nitrogen into the carbon matrix. Amine- and nitrogen-rich polymeric materials are considered as the more reliable sources of N-doped carbon.[266] Graphitic carbon nitride is a nitrogen-rich graphene analogue containing ≈60% nitrogen with rich active sites for alkali metal ion storage and a theoretical capacity of 524 mAh g^{-1}. However, bulk C_3N_4 suffers from unsuitable intercalation/deintercalation due to the extremely high Li adsorption energy caused by the interaction between its graphitic C_3N specie and Li^+. By controlling the size and shape, Adekoya et al. fabricated a porous 1D-C_3N_4 nanofiber with suitable Li adsorption energy at the edges of the nanofiber, high surface area, and several reversible Li active sites. **Figure 20**a shows the SEM image of the 1D-C_3N_4 nanofiber displaying its 1D architecture and porous structure. Compared to previous bulk and 2D C_3N_4 LIBs electrode, which only delivered about 50 mAh g^{-1}, the 1D C_3N_4 nanofiber exhibited a reversible capacity of 181.7 mAh g^{-1} at 0.5C and 138.6 mAh g^{-1} at 10C after 5000 cycles (Figure 20b). This performance remains the best performance of all g-C_3N_4 electrodes to date. This work exemplified the significance of employing the WDN design to tune the properties and boost the performance of electrode materials for rechargeable batteries. Through controlled nano-structuring of carbon, Wei et al. reported the application of soft template assisted hydrothermal synthesis for obtaining mesoporous carbon microspheres (MPCs) and employed it as an anode material for SIBs. By using Pluronic F127 as a soft template, a self-assembly approach was achieved during hydrothermal. The carbon microspheres exhibited an extremely large surface area of

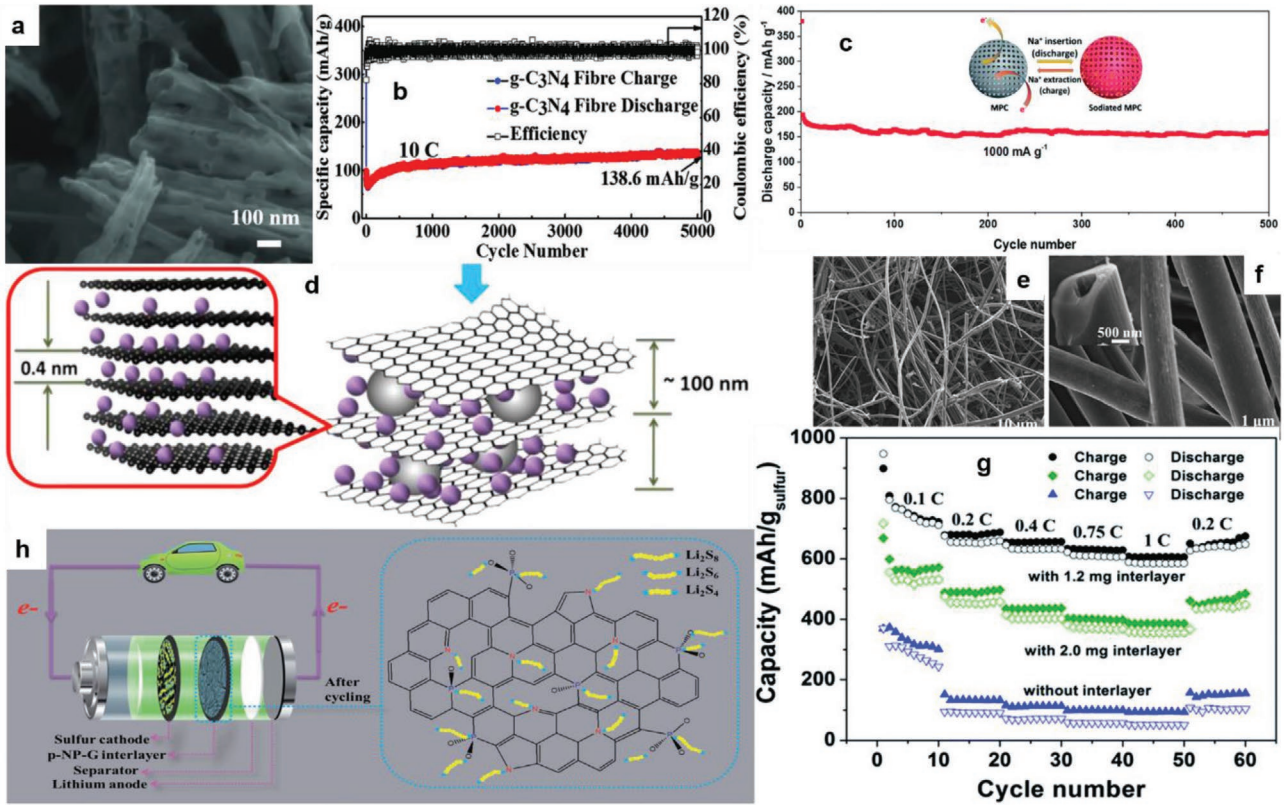

Figure 20. Schematic illustration of the fabrication of WDNs via the spatial arrangement of 1D nanofiber: a) SEM image of the 1D-g-C_3N_4 fiber; b) cycling performance of 1D-g-C_3N_4 fiber structure at a high current density of 10 C. Reproduced with permission.[271] Copyright 2018, Wiley-VCH. c) Long-term cycle performance at 1000 mA g^{-1} for MPC-700 (inset is the scheme of the electrochemical process for MPCs) Reproduced with permission.[267] Copyright 2016, The Royal Society of Chemistry. d) Schematic diagram of Na ions storage mechanisms of AC/G nanocomposites. Reproduced with permission.[268] Copyright 2015, Elsevier. e,f) SEM images of bamboo fibers (BCFs). g) The rate capability of the cells with and without interlayer. Reproduced with permission.[269] Copyright 2015, The Royal Society of Chemistry. h) A p-NP-G membrane incorporated in a Li–S battery and adsorptive mechanism of polysulfides at the p-NP-G membrane. Reproduced with permission.[270] Copyright 2015, The Royal Society of Chemistry.

642.5 m^2 g^{-1} and were mesoporous in nature (2–3 nm). Through well-defined nano-structuring, one of the major features of the MPCs, which significantly impacted its SIBs performance, is its spherical shape. The MPCs formed thin film electrodes with no definite orientation, which promoted the even distribution of current through the electrode. Also, the spherical shape is favorable for achieving high packing density, which promotes stable rate capability and performance. Due to these benefits, the MPCs delivered a very high reversible capacity of approx. 160 mAh g^{-1} after 500 cycles when cycled at 1000 mA g^{-1} (Figure 20c) with high rate stability and capacity retention.[267] Li et al. also reported the fabrication of an amorphous carbon/graphene (AC/G) nanocomposite, by hydrothermal synthesis, as an anode material for SIBs. The AC spheres in the composite served as the nanopillars to enlarge the graphene interlayer distance for the effective storage of large-sized Na^+ (Figure 20d). A reversible capacity of 120 mAh g^{-1} was obtained at ultra-high 10 A g^{-1}, and 142 mAh g^{-1} was retained after 2500 cycles when tested at 0.5 A g^{-1}.[268] The design of WDNs has also been exploited for lithium–sulfur (Li-S) battery systems due to the possibility of tuning the properties of materials at the nanoscale level. Gu et al. reported the controlled synthesis of conductive interwoven carbon fibers derived from bamboo via electrospinning. Figure 20e shows that the carbon fibers were indeed interwoven with a fiber-like morphology, while the hollow nature can be seen from the high magnification SEM image of the top view of a single fiber (Figure 20f). Such interconnected architecture of porous carbon fibers will create an interconnected network for electronic and ionic transport. The bamboo-derived carbon fibers were eventually used as an interlayer (BCFM) for the effective suppression of dendrite formation and inhibiting polysulfide shuttling in Li-S batteries. At a high current of 1C, the electrode with BCFM interlayer delivered 588 mAh g^{-1} rate capability which surpassed that of the electrode without the interlayer (Figure 20g).[269] The same group also reported the nanoscale fabrication of a phosphorus and nitrogen-doped graphene as a blocking layer for polysulfides in Li-S batteries (Figure 20h).[270]

5.2. Metals/Alloys WDNs

Electrode materials which exhibit the alloying mechanism (Li_xM where M represents the metals that include Sb, Sn, Si, Ge, and Sn,) and they are characterized by their very high theoretical capacities when applied as the anode materials; therefore, they are believed to produce high-capacity and energy density LIBs for large scale applications. Unfortunately, these families of

anode materials are hampered by several challenges, including poor electronic conductivity, sluggish Li^+ reaction kinetics, and excessive volumetric changes. These issues lead to poor cycle performance (reversible capacity far below their high theoretical capacity), instability, and inferior rate capability. In addition, the group of alloying materials is often prone to the side reactions which arise from the surface dendrite formation, and this destroys the separator as well as battery integrity. Of all these problems, the most common and destructive one is the large volume changes because this directly affects the structural integrity of the active material in the electrode and impacts the energy density of the battery. Also, when volume changes occur in the electrode material, it fractures the sub particle. This leads to the disruption of electrical contact, which impacts the electrical conductivity, and the distortion of the SEI layer, and therefore a new electrode–electrolyte surface layer is formed, thereby impeding Li^+ transport. If the expansion continues, the electrode will detach from the current collector and the separator will be damaged. Since the problem of volume changes is connected to the structure of the active materials, modifying their chemical and physical characteristics, including the size, shape, hetero-architecture, and spatial arrangement, can address these issues. A shift from macroscale to nanoscale dimension can significantly dictate how the active materials deal with the issues of volume change and how it performs in the battery cell. To this end, designing well-defined nanostructured materials have proven to be a viable solution to the structural issues accompanying alloying anode materials, and several significant works have demonstrated this. For example, as an alloying anode material, Sb exhibits a relatively high theoretical capacity of 660 mAh g^{-1} for LIBs, but it suffers from extremely large volumetric variation (up to 390%). Liang and co-workers synthesized fern-like Sb composed of well-crystallized Sb nanoparticles to address this problem as well as the poor rate capability and capacity fading issues. By using the cost-effective electrochemical deposition method, the authors successfully grew metallic Sb on a Ti substrate, and by controlling the growth mechanism, a fern-like morphology composed of Sb nanoparticles was designed. The significance of this WDN design is that by controlling the growth of the leaves of the fern, spaces can be created in between them serving as porous spaces for enhancing ionic transport and accommodating the volume expansion during cycling. Thanks to the unique WDN design, the fern-like Sb was applied as a binder-free electrode for SIBs and a reversible capacity of 589 mAh g^{-1} was retained at 0.5 A g^{-1} after 150 cycles (98.5% capacity retention) along with impressively high rate capability even at 10 A g^{-1} and after 80 cycles. Also, the WDN fern-like Sb was applied as an SIB full cell anode material, and it delivered more than 400 mAh g^{-1} after 100 cycles when tested at 0.5 A g^{-1} as well as excellent rate capability.[272]

The problem of poor intrinsic conductivity suffered by alloying materials can be resolved by the introduction of highly conductive elements such as Ni and Fe. The addition of these metallic elements can modulate the electronic conductivity. Since these elements are ductile, they also function as buffers to impede the volumetric expansion, which occurs during the cycling of the electrode materials. This concept was explored in the work of Liang et al. when they fabricated a hierarchical Sb-Ni nanoarray as a binder-free SIB anode material. A schematic illustration of the fabrication of the Sb-Ni nanoarrays is depicted in **Figure 21**a–c. The scheme shows that the aluminum oxide template (Figure 21a) was used to obtain Ni nanoarray (Figure 21b) via the electrodeposition, and the final Sb-Ni array (Figure 21c) obtained after in situ growth of Sb nanoplates on the Ni nanoarrays. The SEM image of the 3D Sb-Ni array (Figure 21d) shows the well oriented and evenly spaced 3D Sb-Ni nanoarray architecture. Due to the unvaried and well-organized distribution of the conductive nanorod arrays, abundant reactive sites and diffusion pathways were available for the electron and ion transport. To this end, at 0.5 A g^{-1}, a reversible capacity of 579.8 mAh g^{-1} was retained after 200 cycles (Figure 21e) along with an energy density of 100 Wh kg^{-1}. Also, the post cycle SEM image (Figure 21f) shows that the 3D Sb-Ni nanoarray maintained its morphology after 200 cycles.[273] Alloying anode materials are also limited by the onset of surface electrode–electrolyte side reactions caused by dendrite formation, and this affects the performance of the battery. The coating of the alloying metals with conductive carbon is a very effective approach to deal with this problem because the carbon functions as a protective shield between the electrolyte and the alloying active material. This approach is a very effective method as the carbon provides a conductive network for the interconnected transport of ions, thereby boosting the electrical conductivity of the electrode, protecting the active material, and providing room for volume expansion. By encapsulating the bismuth nanospheres in a porous carbon network, Qiu et al. effectively boosted its electronic conductivity and suppressed the volume changes. The use of a molten salt phase during the synthesis of the electrode material prevented the aggregation of the bismuth nanospheres and aided the particle size control. The controlled distribution of bismuth nanospheres also ensured the creation of nanopores which were beneficial for electrolyte penetration and ionic and electronic transport. Moreover, the nanostructure design encouraged effective contact between the current collector and the electrode material. Post cycle analysis further confirmed that the bismuth nanoparticles were preserved after 60 cycles. The composite exhibited a reversible capacity of 106 mAh g^{-1} at 0.2 A g^{-1} after 1000 cycles.[274] Jin et al. also exemplified the concept of carbon encapsulation in their report by hosting phosphorus in a hollow carbon nanosphere. By hosting the red phosphorus in hollow carbon nanospheres, the authors aimed at resolving the issue of excessive volume expansion (300–500%) and other issues limiting the application of phosphorus. While this approach is a very effective one, the possibility of surface phosphorus displaced on the carbon coating can lead to side reactions, which will result in capacity deterioration. To ensure that no surface phosphorus coating occurred, the authors carried out secondary annealing after treatment, which further improved the electrical conductivity of the electrode and rearranged the phosphorus into pores of the carbon nanospheres, ensuring it was adequately confined. As an SIB anode, a superior capacity of 1027 mAh g^{-1} was recorded at 4 A g^{-1} after 2000 cycles, demonstrating excellent cycle life.[275] Yan et al. also reported the encapsulation of phosphorus in an MOF (ZIF-8)-derived porous carbon for LIBs. This work also focused on solving the problem of volume changes associated with alloying red phosphorus by protecting the active material in a conductive

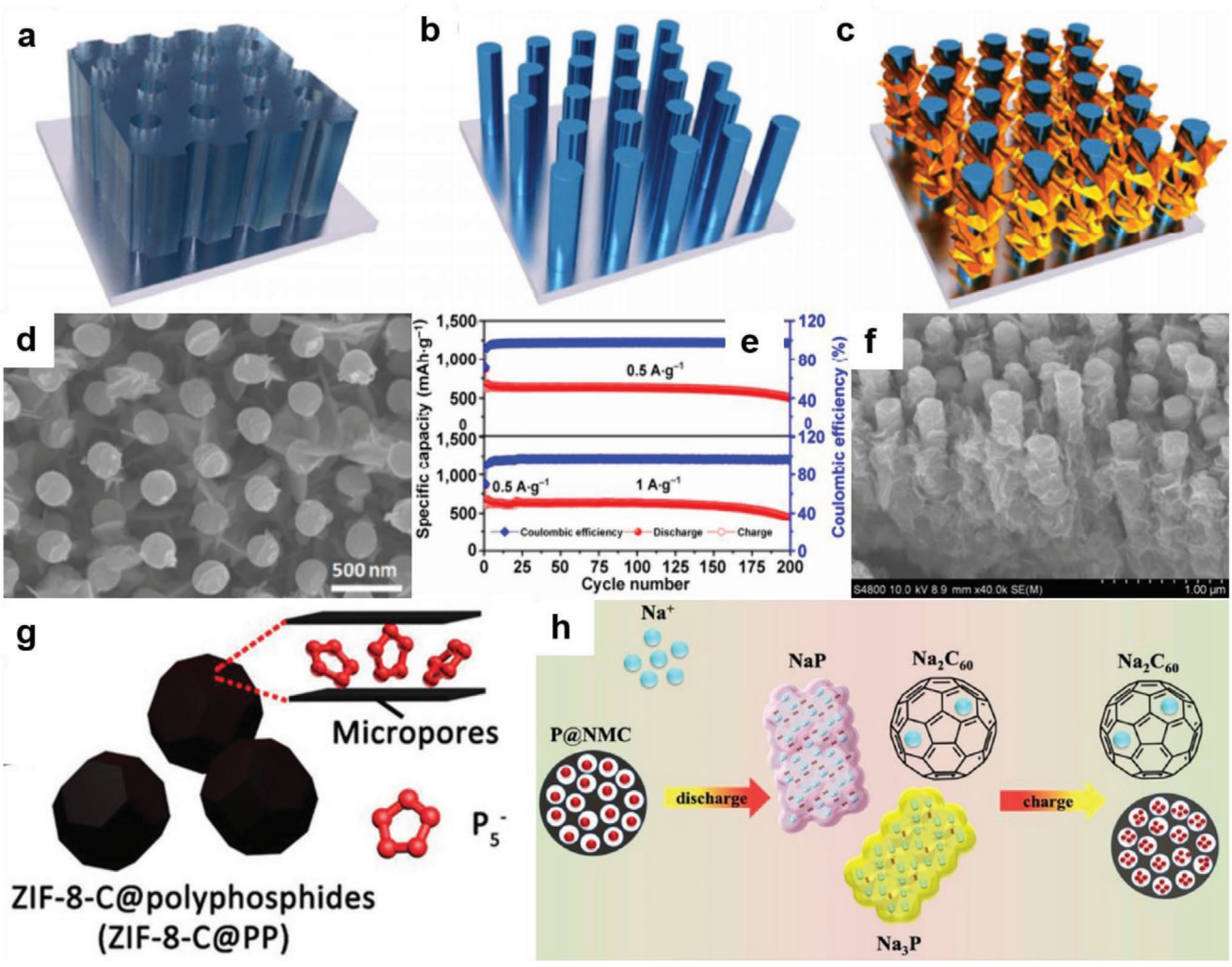

Figure 21. a) Schematic illustration of AAO template, b) Ni nanorod arrays, and c) 3D Sb-Ni nanoarrays. d) SEM image of 3D Sb-Ni nanoarrays. e) Cycling performance at current densities of 0.5 and 1.0 A g^{-1}. f) SEM image of 3D Sb-Ni nanoarrays anodes after 200 cycles. Reproduced with permission.[273] Copyright 2017, Springer Nature. g) Schematic of ZIF-8-C@PP illustrating P_5^- adsorbed into its micropores. Reproduced with permission.[276] Copyright 2020, Wiley-VCH. h) Representative illustration of the electrochemical reaction process for the P@NMC. Reproduced with permission.[277] Copyright 2020, Elsevier.

carbon shell. A common roadblock in the design of such phosphorus-protected nanostructured material is ensuring that it is effectively encapsulated in the carbon shell, and no phosphorus particles are dispersed at the surface. This is particularly challenging because red phosphorus is a large block-like particle. To cross this hurdle, the authors employed a solution-based strategy in which phosphorus is incorporated into the micropores of the MOF-derived carbon in the form of negatively charged polyphosphate ions (P_5^-) (Figure 21g). This unique approach ensured the optimum utilization of the active material and secured protection from volume changes during repeated cycling. Also, the use of MOF-derived carbon provided a porous host that facilitates electron transport and ionic transfer through the electrode, which improved the conductivity and performance for LIBs. A reversible capacity of 786 mAh g^{-1} was delivered at 0.1 A g^{-1} after 100 cycles along with excellent rate and cycle stability.[276] Zhang et al. also reported the confinement of red phosphorus in N-doped carbon (P@NMC) for SIBs. By using a unique self-assembly method, N-doped multicavity carbon was synthesized, and it was used as a host for red phosphorus. The nitrogen-rich active sites in the highly porous carbon host ensured efficient transfer of electrons and Na^+ to the guest and provided room to accommodate volume changes, thereby protecting the P from pulverization (Figure 21h). The P@NMC composite delivered 923.7 mAh g^{-1} at 0.5 A g^{-1} after 100 cycles with impressive cycle stability and rate capability.[277]

5.3. Transition Metal Oxide-Based WDNs

Another family of materials with high theoretical capacity is the transition metal oxides. They are also low-cost since they are largely available in the earth's crust. In rechargeable batteries such as LIBs, metal oxides are characterized by two reaction mechanisms: the insertion and conversion reaction mechanisms. Generally, metal oxides react with Li^+ to form metal NPs

inside the Li_2O matrix, and this process is thermodynamically favorable. However, the reverse reaction, which involves the decomposition of Li_2O is rather difficult as it is accomplished by the interaction between the metallic NPs specie and inert Li_2O. This is where well-defined nano-structuring of the metal oxide becomes essential because the bonding orientation of surface atoms has a considerable effect on the physical properties of the materials. In a nutshell, the quantity of Li^+ that can successfully interact with the Li_2O matrix is greatly influenced by the nanoscale architectures of the electrode materials. Metal oxide electrodes in rechargeable batteries are also hampered by the low coulombic efficiency, large voltage hysteresis, and high working potential. Through nanoscale chemistry and specifically the design of well-defined nanostructured materials, these issues can be resolved. Furthermore, like alloying materials, metal oxides suffer from structural strain after repeated cycling, and the application of WDNs is a practical solution to this problem. The metal oxides include the oxides of cobalt (Co), iron (Fe), and nickel (Ni), and of this family, Co and Fe represent a popular category because of their very high theoretical capacity. For instance, Fe_2O_3 possesses a theoretical capacity of 1006 mAh g^{-1}, but it is still affected by the low Li^+ diffusivity, inferior electrical conductivity, below-par reversible capacity, and pulverization caused by volume changes. To address these issues, Wang et al. synthesized 4 nm hexagonal-shaped ultrathin Fe_2O_3 nanoflakes by employing a unique chemical stripping method. In line with the previous reports,[278] the (001) facet of Fe_2O_3 was identified as the more stable facet with higher crystallinity and superior Li-ion diffusivity. However, isolating this facet from the Fe_2O_3 nanosheet is not an easy task. In this work, the authors used the high hydrogenation and annealing treatment to strip off the disordered layers, assisting the reduction in thickness and formation of uniform Fe_2O_3 nanoflakes with exposed (001) surface. This unique and effective synthesis method provided Fe_2O_3 with better electronic conductivity, crystallinity, and excellent battery performance. Compared to pure Fe_2O_3, the as-synthesized Fe_2O_3 nanoflakes delivered a superior long cycle reversible capacity of 599 mAh g^{-1} at 5 A g^{-1} after 500 cycles. The authors attributed the outstanding performance to the thin 2D structure of the Fe_2O_3 nanoflakes, as this facilitated rapid Li^+ transport and discouraged the volumetric variation during cycling.[278] Xu et al. also reported the synthesis of α-Fe_2O_3 nanoplates via a facile iron-based ionic liquid assisted solvothermal synthesis method. Thanks to the nucleation and self-assembly property of the ionic liquid, the formation of 2D α-Fe_2O_3 nanoplates was simply achieved during the solvothermal synthesis. The authors studied the difference between the solid microspheres, nanoparticles, and α-Fe_2O_3 nanoplates, and the LIB results showed that the performance of the nanoplate architecture exceeded the others. A reversible capacity of 1950 mAh g^{-1} was recorded at 0.5 A g^{-1} and up to 520 mAh g^{-1} was retained after 1000 cycles at 10 A g^{-1}. It was discovered that the nanoplates performed better than the microsphere and nanoparticle because of its regular distinct morphology, higher surface area, and structural integrity even after 1000 cycles.[279] Fe_2O_3 can also be synthesized in different nanoscale architectures such as nanotubes,[280] nanodiscs,[281] nanoflakes,[282] nanotubes,[280] and hollow nanoparticles.[283] Another widely used metal oxide anode material is Co_3O_4; based on its conversion mechanism involving eight electrons, it possesses a theoretical capacity of 892 mAh g^{-1}, and like Fe_2O_3 tuning, its nanoarchitecture can modulate the electronic properties and battery performance. WDNs of cobalt oxide has been achieved in different morphologies and shapes such as 1D nanowires, nanotubes,[284] nanoneedles,[285] nanobelts,[286] nanosheets,[287] multi-shelled hollow spheres,[288] and nanocages.[289] By controlling the synthesis method and thermodynamic properties, these WDNs can be synthesized, and modification of their size, shape, heteroarchitecture, and spatial arrangement significantly impact their battery performance.

TiO_2 is another common metal oxide for rechargeable batteries, with different phases, such as the anatase and rutile, and several unique morphologies. The controlled design of WDNs is highly beneficial for tuning its electronic conductivity and battery performance. Surface modification and engineering of materials to optimize the availability of ions and how to maximize the wettability of solvents were explored by Zhou et al. using amorphous TiO_2 inverse opal. Their work showed that by improving the availability of surface ions through better wettability of solvents, the SIB performance of TiO_2 anode material was significantly improved, and this concept can be employed to other anode materials.[104] Different approaches have been made to improve the inferior rate capability of TiO_2 as an anode material concept of the AAO template that has been devoted to developing well-constructed nanostructured electrodes with enhanced storage capacity and rate capability on sodium-ion batteries (SIBs).[104,273,290,291] Highly ordered Sb[291] and Ni@TiO_2[290] nanoarrays were fabricated (**Figure 22**a–d) and have been used as high-performance anodes of SIBs. Designing nanoarrays with appropriate parameters give enough interval spaces among the nano-units for alleviating the damage of volume expansion during charging/discharging and facilitating electrolyte accessibility. By optimizing the aspect ratio of Sb nanorod arrays with a diameter of 190 nm and length of 1.5 μm, it shows high capacities of 620 mAh g^{-1} at 0.5 A g^{-1} and 557.7 mAh g^{-1} at 20 A g^{-1} (Figure 22e). Ni/TiO_2 core/shell nanoarrays also exhibited high rate capabilities of the respective anode materials (Figure 22f). Moreover, both works explored the impact of ordered nanoarrays on the sodium-ion storage comparing to their disordered counterparts, demonstrating that such highly ordered nanoarrays can simultaneously facilitate the fast electron transport, interfacial ion diffusion, and remarkable integrity of electrode at high-rate charge and discharge (Figure 22g), and hence play a crucial role in improving the rate capability of the batteries.

Although hollow metal oxides show great promise to address the issue of volume expansion, poor conductivity is still a common problem that limits the application of metal oxide anodes. To solve this problem, Wang et al. reported the synthesis of a hollow-shell V_2O_5 nanosheet (THS-V_2O_5) synthesized via a hard template method for full and half-cell LIB anode material. By creating hollows in the metal oxide (see inset of **Figure 23**a), a metal oxide with shortened charge transfer distance, reduced Li^+ transport resistance, and improved conductivity was achieved. Due to the controlled synthesis of the nanostructured anode material, a high reversible capacity of ≈400 mAh g^{-1} was retained after 100 cycles for the half cell LIBs (Figure 23a) and 250 mAh g^{-1} was recorded for the full

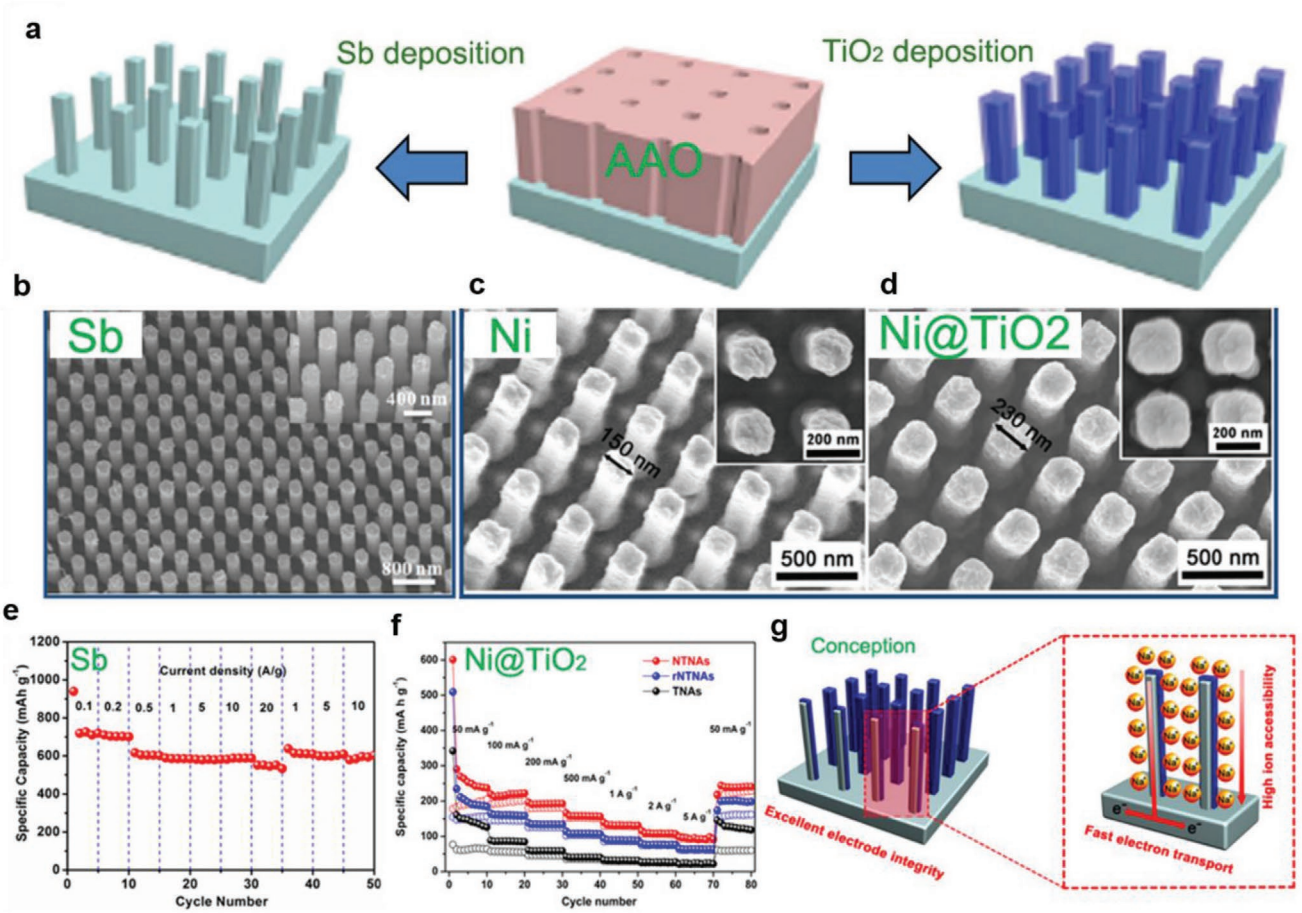

Figure 22. The fabrication of a nanoarray (i.e., a type of WDNs) via the controlled manipulation of 1D nanorods: a) Process of fabricating Sb and Ni@TiO_2 nanoarrays. SEM images of Sb (b), Ni (c), and Ni@TiO_2 (d) nanoarrays. e) Rate performance of SIBs based on Sb nanoarrays. f) Rate capability of SIBs with three different Ni@TiO_2 nanoarray anodes. g) Proof-of-concept demonstration of highly ordered nanoarray electrode configuration. Reproduced with permission.[291] Copyright 2015, Royal Society of Chemistry, and reproduced with permission.[290] Copyright 2015, American Chemical Society.

cell application.[292] Another proven way to overcome the poor conductivity is through the nanocomposite formation with the highly conductive carbon materials. Furthermore, the protective layer provided by the conductive carbon can function as a buffer to accommodate the volume changes in the metal oxide electrodes, thereby preventing pulverization. The Sun group reported the even distribution of diamond-like Fe_3O_4 nanoparticles on graphene nanosheets (see inset of Figure 23b) to suppress the volume changes during cycling, prevent aggregation of the NPs, enlarge the surface area, increase the conductivity, and achieve stable cycling. By using a simple synthesis approach, the Fe_3O_4/graphene composite was designed and employed as an anode material for LIBs and SIBs. In LIBs, the composite delivered 600 mAh g^{-1} at a high current density of 3000 mA g^{-1} (Figure 23b). In both battery systems, the composite outshined the Fe_3O_4 and graphene nanosheet and demonstrated superior conductivity with reliable structural stability.[293] Likewise, Yang et al. reported the fabrication of 3D WDNs TiO_2@C core/shell nanobelt arrays with MOF as the source of carbon. In this work, 1D TiO_2 nanobelts were uniformly assembled on a Ti substrate to obtain a 3D TiO_2 nanobelt array, which was subsequently coated with a porous carbon shell derived from ZIF-67 MOF (Figure 23c). By uniformly growing the 1D nanobelts on the Ti substrate, a larger surface area was provided for rapid electron transport, and the charge transfer distance was shortened and the migration of Na^+ unhindered. The composite also benefitted from the functional electron and Na^+ transport due to the carbon coating, which significantly improved the conductivity.

The composite exhibited a reversible capacity of 210.5 mAh g^{-1} after 100 cycles at 50 mA g^{-1} with impressive cycle life.[294] Zhang et al. also fabricated a 3D composite comprised of 1D-TiO_2 nanofibers and 1D free-standing and bendable carbon nanotubes. CNTs served a dual function in the composite, in that it formed in a conductive network for effective electron transfer and fostered Li^+ transfer through the composite. Additionally, the aggregation of TiO_2 was prevented because of the synergistic interaction between both materials. The nano-structural transformation of the two 1D architectures to produce a better 3D composite material displayed the versatility of WDNs.[295] Congruently, by taking advantage of the high conductivity and large surface area of graphene, Cai et al. synthesized a nanocomposite of N-doped graphene modified TiO_2 for LIBs. A gas/liquid interface synthesis approach was deployed to synthesize the composite such that aggregation of

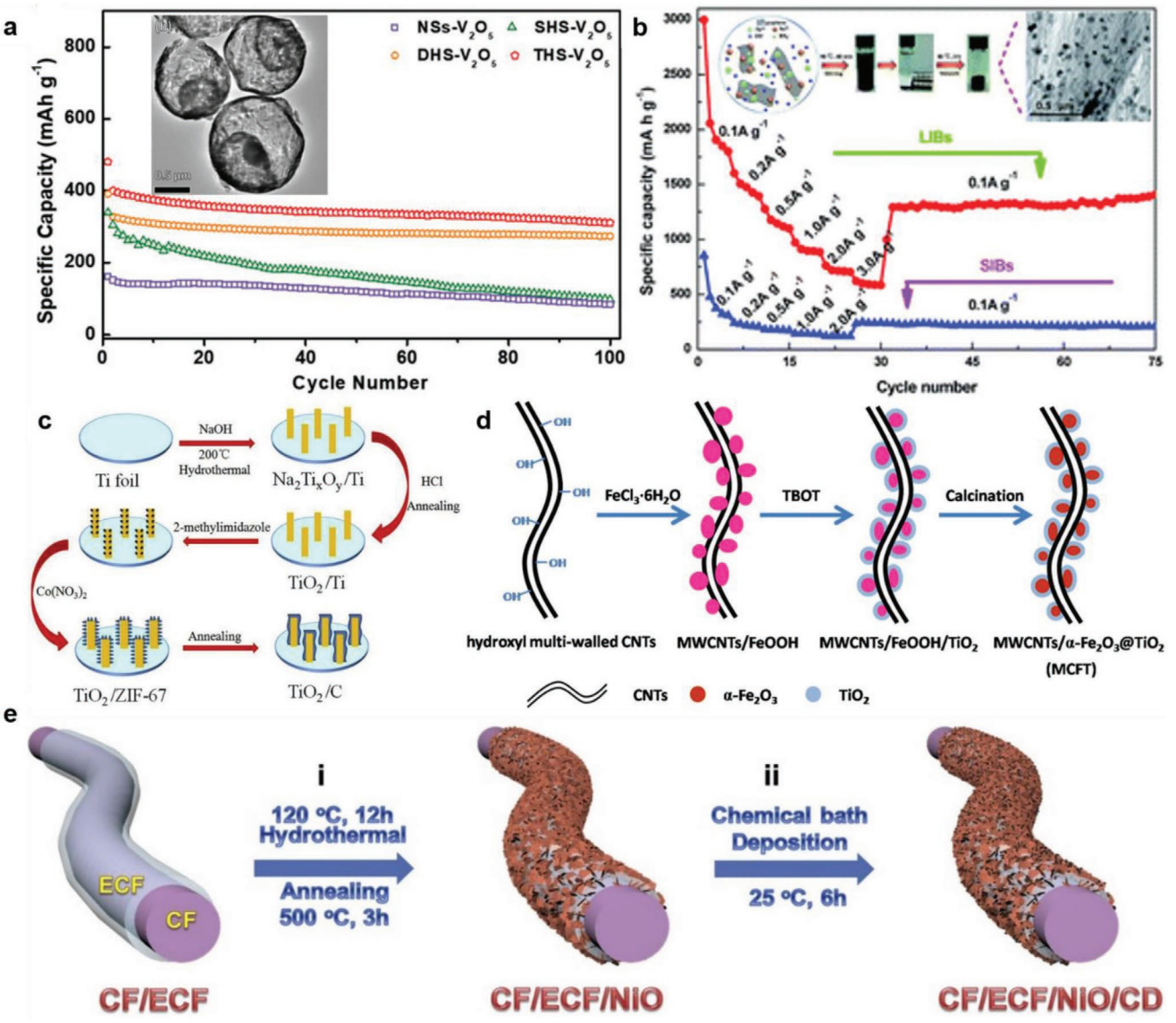

Figure 23. a) Cycle performance of the THS-V_2O_5-cathode; inset: TEM image of the THS-V_2O_5. Reproduced with permission.[292] Copyright 2019, Wiley-VCH. b) Rate performance of the Fe_3O_4 (blue) and Fe_3O_4/graphene (red); inset: schematic illustration of the synthesis process of diamond-like Fe_3O_4/graphene composite. Reproduced with permission.[293] Copyright 2016, The Royal Society of Chemistry. c) Schematic illustration of the preparation process for the anatase 3D TiO_2@C core/shell nanobelt arrays. Reproduced with permission.[294] Copyright 2018, Elsevier. d) Schematic of the synthetic process for MCFT. Reproduced with permission.[297] Copyright 2013, Elsevier. e) Schematic synthesis of WDNs via a controlled manipulation of 0D and 1D nanomaterials in the synthesis of the CF/EF/NiO/CD hybrid. Reproduced with permission.[298] Copyright 2020, Elsevier.

TiO_2 NPs could be prevented, the conductivity will be improved, and a superior LIBs performance will be achieved. The LIB performance of the TiO_2/nitrogen-doped graphene nanocomposite surpassed that of TiO_2 NPs and TiO_2/graphene nanocomposite.[296] Wang and Sun et al. designed a nano-heterostructure of multi-walled carbon nanotube (MWCNT)-modified Fe_2O_3/TiO_2 for LIBs. The heterostructure possessed a unique stem-like morphology, which was evident by the intertwining of the Fe_2O_3/TiO_2 with MWCNTs (Figure 23d). This nano-architectural design ensures close effective contact between the constituents of the nanocomposite and creates an interconnected network for electron and charge transfer. The composite also exhibited a high surface area thanks to the stem-like architecture and the MWCNTS. A reversible capacity of 770 mAh g^{-1} was retained after 200 cycles when the composite was tested at 200 mAg and 670 mAh g^{-1} at 1000 mA g^{-1}. The authors attributed the performance to the high theoretical capacity of Fe_2O_3, improved conductivity due to MWCNT, and the steady structure of TiO_2 to accommodate the volume changes.[297] Carbon coating of other metal oxides has also been reported. For example, Huang et al. reported the tuning of the adsorption energy of NiO nanosheet by coating it on a porous N-doped carbon fiber along with carbon QDS. Typically, the N-doped carbon fiber is a 1D WDN, and it was coated with NiO via the facile hydrothermal method, and finally, carbon QDS was deposited on the architecture via the chemical deposition. In this unique hybrid architecture

denoted CF/ECF/NiO/CD, NiO nanosheet functioned as the active material, N-doped carbon as the current collector, and carbon QDS as the stabilizer (Figure 23e). As a flexible LIB, the hybrid nanostructure delivered a high energy density of 201.7 W kg^{-1} and a high areal capacity.[298] Nitrogen doping can create defects on the surface of carbon materials such as graphene, and the oxygen vacancies are also able to tune the electronic properties of a material without altering its intrinsic properties, and metal oxides are known to possess these oxygen vacancies.[177] Xu et al. reported that tuning the oxygen vacancy can be utilized as an effective strategy to enhance the sodium-ion storage of MoO_{3-x} nanosheets. The effect of oxygen vacancies at deep-charging condition can be enhanced through coating an optimal ultrathin Al_2O_3 layer on the MoO_{3-x} nanosheets.[299] This strategy was also confirmed by the SIBs with oxygen-vacancies-containing SnO_2 ordered arrays that exhibit high rate capability with the capacities of 210 mAh g^{-1} at 10 A g^{-1} and 200 mAh g^{-1} at 20 A g^{-1}.[85] This type of binder-free nanoarray architecture can exclude the influences of conductive additives and binders. Gu et al. reported the application of a simple and scalable ball milling method for coating ZnO and $Ni(OH)_2$ with S-doped carbon for Li-S battery. 1D carbon nanotubes were used as the source of carbon and this was ball milled with sulfur which was then used to coat the metal and metal hydroxide. The common problems of polysulfide dissolution and shuttling effect, which are limiting large scale application of Li-S batteries, were addressed by the effective surface interaction initiated between the metal oxide (ZnO) and the sulfur specie in the electrolyte.[300]

Apart from the carbon coating or modification of metal oxides to form nanostructured composites, they can also be combined with each other to maximize their individual high theoretical capacities. To effectively minimize the volume changes of Fe_2O_3, Fu et al. reported the synthesis of a highly porous and hollow α-Fe_2O_3@TiO_2 core–shell nanosphere for LIBs and SIBs. The core–shell structure design is highly beneficial for alkali-metal ion storage because the vacant space in such hollow structures can accommodate large volume changes of Fe_2O_3. Also, the porous nature of the nanostructure will facilitate electron transport and ionic transfer through the electrode material. Unoccupied zig-zag pathways in the crystallographic structure of TiO_2 also provide active sites for Li^+/Na^+ storage. Thanks to these properties of the Fe_2O_3@TiO_2 core–shell nanosphere, it displayed excellent performance in both LIBs and SIBs more than the individual electrodes.[301]

5.4. Silicon-Based WDNs

Silicon (Si) is one of the most popular and widely used anode materials for rechargeable batteries, especially LIBs, due to its superior volumetric, gravimetric, and theoretical capacity in comparison to other elements. Furthermore, Si in its raw form is cheap and abundant in the earth's crust. Because it operates at a lower working potential compared to graphite, it can avoid some problems; thus, it is commercially used in an increasing scale in LIBs. Therefore, although Si is a member of the alloying family, we have chosen to discuss it separately.[219] Due to its smaller atomic mass, Si forms an alloy with Li^+ to deliver up to 8.5 Ah cm^{-1} or 4.2 Ah g^{-1} which exceeds that of other electrode materials. However, this alloying process ($Li_{4.4}Si$) results in a 440% increase in the number of atoms, resulting in large volume change (over 300%) which could be catastrophic to battery performance and life.[302] By designing well-defined nanostructured Si anode materials, the large volume change experienced by bulk Si can be significantly minimized because such nanoscale materials provide a higher surface–to-volume ratio which will equalize the system. For example, well-defined 1D Si nanomaterials such as 1D nanowires,[303] 1D nanotube,[304] and 1D micro/nanoporous nanorods[305] provide a high aspect ratio compared to their 0D counterparts; therefore, they have proven to effectively curtail rapid volume changes in Si anodes.[246] The green controlled synthesis of well-defined hollow 1D Si nanostructures was reported by Huang et al. via a carbon templating method using carbonates (**Figure 24**a). By modifying the reaction time and precursor, the authors designed various 1D hollow nanostructures (Figure 24b–m) which were applied as anode materials for LIBs.[306] Hollow 1D WDNs also provide an additional benefit of fast ionic and electron transfer through the hollow 1D WDNs, and this not only ensures stable cycle life but also improves conductivity and performance.[306,307] Castrucci et al. and Yao et al. showed that by creating hollows in 1D nanotubes and nanospheres, the volume changes could be accommodated, and pulverization can be lessened while conductivity can be improved.[307,308] Yao et al. synthesized hollow Si nanospheres coated on stainless steel substrate (see Figure 24n), and the hollow architecture of the Si spheres prevented the excessive volumetric change and improved LIBs' cycle life. After 700 cycles, the Si hollow nanospheres retained up to 1420 mAh g^{-1} with a coulombic efficiency of 99.5%.[308] Xia et al. also reported the fabrication of the Si membrane (see inset of Figure 24o), which is capable of absorbing/distributing the electrode strain generated during cycling, thereby supporting the electrode against volume changes and pulverization. The Si membrane delivered an ultra-high reversible capacity of 2414 mAh g^{-1} after 100 cycles when cycled at 0.1 C (Figure 24o).[236]

Another major limitation of the Si anode materials is that during lithiation, a thin Si film is formed. This film expands and contracts during cycling, building up tensile stress in the active material and resulting in cracks/fissures, which ultimately cause the electrode to be detached from the current collector. Additionally, while the nanoscale design is highly beneficial to fabricating better Si anode materials, low tap density is a concern for Si nanomaterials as well as the possibility of side reactions due to their large surface area.[219] 2D silicon WDNs has proven to be a viable solution to these problems because they display superior cycle and structural stability than 0D NPS and 1D Si architectures. This was proven by the work of Xie et al., who compared the performance of 1D Si nanowires and 2D Si nanonets for LIBs. The authors reported that the 2D nanonets retained 90% of its initial capacity, unlike 1D nanowires which could only maintain 80%.[307] The report of Chen et al. also solidified this idea by synthesizing mesoporous 2D nanosheet and coating it with carbon to form a carbon-coated Si composite (**Figure 25**a). Comparing its performance to the commercial Si NPs, the 2D architecture exhibited superior cycle

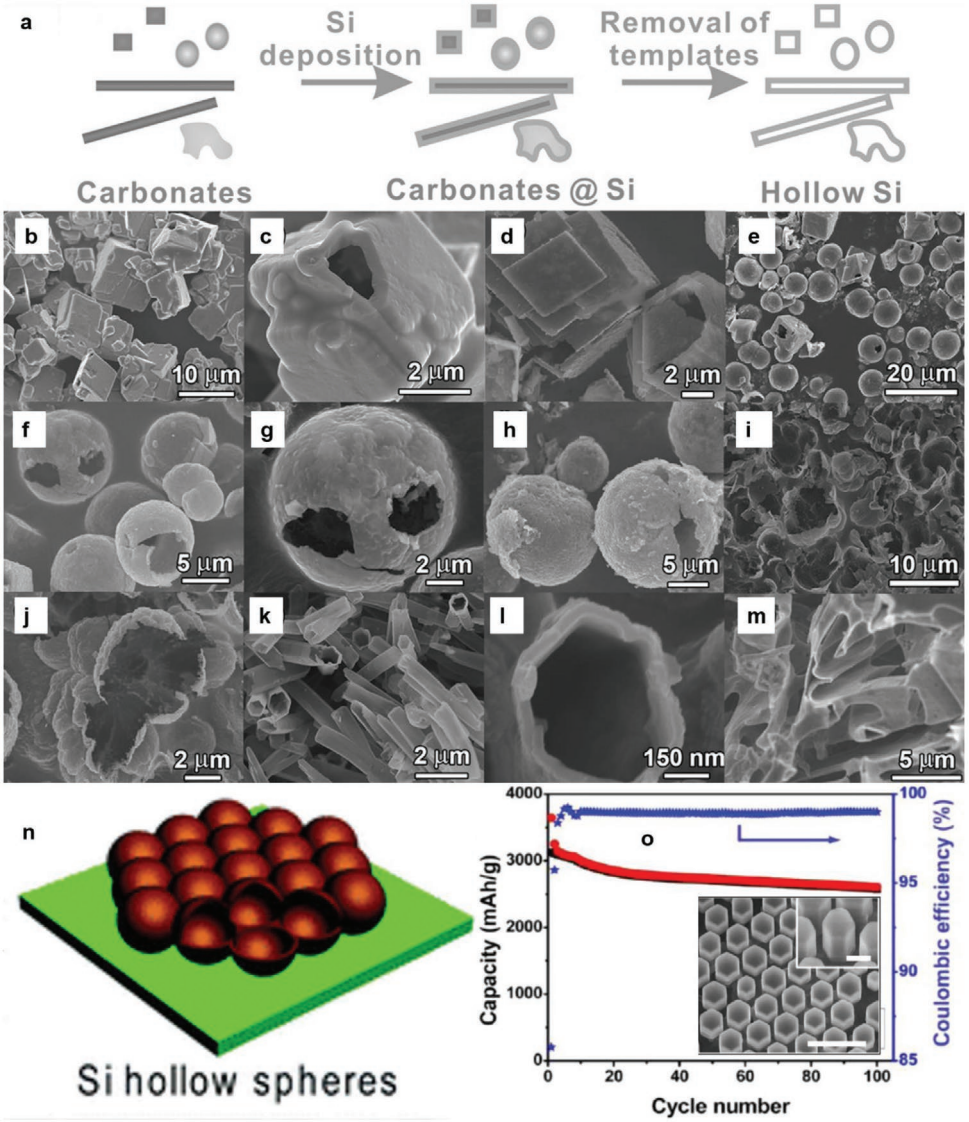

Figure 24. a) Schematic illustration for the synthesis of hollow Si with controllable morphologies (b–m). SEM images of hollow/porous Si: hollow cubes from 4-h Si deposition on cubic $CaCO_3$ (b,c); hollow cubes from 1 h Si deposition (d); hollow spheres from 4 h Si deposition on spherical $CaCO_3$ (e); hollow spheres from 2 h Si deposition (f,g); hollow spheres from 1 h Si deposition (h), flower-like Si from 1 h deposition on $CaCO_3$ obtained at 5 °C (j,k); Si tubes using $BaCO_3$ as a template (k,l); and porous Si using Na_2CO_3 as a template (m). Reproduced with permission.[306] Copyright 2014, Wiley-VCH. n) Schematic of synthesized hollow Si nanospheres on the stainless-steel substrate. Reproduced with permission.[308] Copyright 2011, American Chemical Society. o) Cycle performance of the Si membrane at a rate of 0.1 C for 100 cycles; inset: SEM image of Si membrane. Reproduced with permission.[236] Copyright 2013, American Chemical Society.

life, rate capability, and conductivity than the Si NPs. Even at a high current density of 4 A g^{-1}, the Si/C nanocomposite still retained 1072.2 mAh g^{-1} after 500 cycles (see Figure 25b).[309] A porous 3D nanostructured design of Si anode materials has also proven to be able to mitigate some of the drawbacks of Si. The 3D WDNs of Si experience minimal internal stress during the charge/discharge process and higher tap density due to their thicker and more rigid layers. Also, due to their 3D architecture, they exhibit shorter electronic and ionic transport distance and multiple diffusion pathways. Gowda et al. reported the synthesis of a 3D porous Si anode coated on Ni current collector for LIBs, and a high areal capacity of 0.8 mAh cm^{-2} was recorded along with an impressive cycle and structural stability.[310] Surface modification and composite design of Si-based anode materials is another very effective way to manage the problems of Si anode. Carbon coating is regarded as one of the most effective ways to modify Si because the presence of a conductive carbon material improves the electrical conductivity, provides support to the active Si and boosts the mechanical strength, protects Si from cracks/fissures after repeated cycling, and limits volume expansion. The carbon for coating Si can be sourced from different materials such as hard and soft carbon, biomass, and polymeric carbons.[311] Binders have been proven to have a significant impact on the electrochemical performance of Si for battery storage. For example, Liu et al. reported the application of hard and soft polymers as a cross-linking

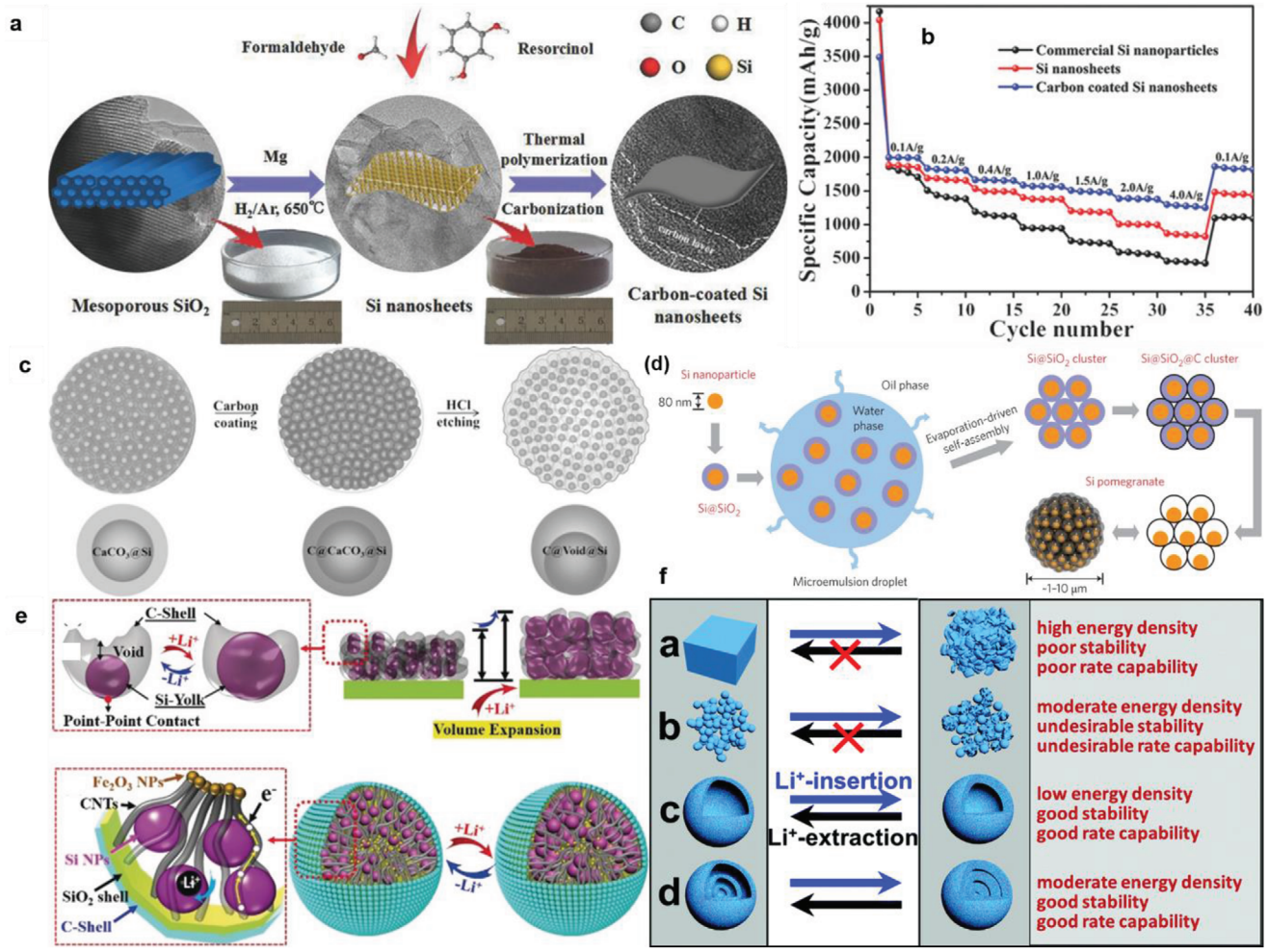

Figure 25. a) Schematic illustration for the synthesis of 2D-Si nanosheet and Si/C nanocomposite. b) Comparison of the rate capability of commercial Si NPs, pure Si nanosheet, and Si/C at different current densities. Reproduced with permission.[309] Copyright 2018, Wiley-VCH. c) Schematic representation of the silicon granadillas' composite design. Reproduced with permission.[316] Copyright 2018, Wiley-VCH. d) Schematic of the fabrication process for silicon pomegranates. Reproduced with permission.[323] e) Schematic illustration of existing yolk–shell Si/C nanobeads and the proposed new yolk–shell Si/C structure. Reproduced with permission.[324] Copyright 2019, Wiley-VCH. f) Schematic illustration of the structural changes for different structures during Li^+ insertion/extraction processes: solid bulk (a); nanoparticles (b); single-shelled hollow structures (c); multi-shelled hollow structures. (d) Reproduced with permission.[315] Copyright 2017, The Royal Society of Chemistry. Copyright 2014, Springer Nature.

agent for covalent bonding between the polymer binder and Si, thereby achieving a high areal and rate capacity with long and stable cycle life.[312] The concept of self-healing Si anode was also developed by Wang et al. in their work which displayed a unique carbon-coated Si anode with the ability to heal itself after the structural damage during cycling. The polymeric carbon matrix used to coat the Si NPs facilitated the self-healing process, and this enabled the composite to deliver high reversible capacity with high capacity retention.[313] Wu et al. also reported a unique concept of vacant engineering spaces between Si NPs in a carbon-coated composite so that the problems of pulverization and unstable SEI are solved. In this work, Si NPs were confined inside carbon tubes so that direct Si-electrolyte contact is prevented, and Si is optimally utilized. The engineering of this SiNP@CT composite, precisely the creation of empty space is indeed a display of WDNs for the advanced battery electrode design.[314] Congruently, core–shell composite structures of Si and carbon materials are widely reported because the WDNs design allows the carbon shell to effectively insulate the core active material from potential fracture or destruction, accommodates the volume changes, improves the conductivity, and prevents the pulverization of the electrode.[311] Also, the number of the shells can be varied by controlling the nanostructure design and such multi-shell nanostructured composites ensure better protection of the core, regulate SEI layer thickness, and effectively minimizes volume changes.[315] For example, Lei et al. reported the synthesis of a granadilla-like Si NP encapsulated with a carbon shell for high-performance LIBs, thanks to the unique synthesis approach for controlling the dispersion of Si NPs, each of which was coated by a carbon shell with a controlled space between the core and the shell (Figure 25c). The creation of this vacant space prevented the aggregation of the NPs and provided ample space for volume changes thereby effectively protecting the Si core from pulverization.

The anode material delivered exceptional reversible capacity (1100 mAh g^{-1} at 250 mA g^{-1} after 200 cycles) with a long and stable cycle life.[316] Conversely, Yang et al reported the fabrication of a double core–shell composite of Si encapsulated by an outer layer of carbon and an inner layer of SiO_2. The double layer protection of Si ensured the stable formation of SEI layer and the improved conductivity and alleviated the pressures of repeated lithiation.[317] Core–shell design of carbon-coated Si composites such as 0D Si/graphene,[318] 1D SiNP@C nanofibers,[319] 1D Si@C nanorods,[320] 1D C@Si nanotubes,[321] and hollow core–shell Si/C[322] have also been reported for LIBs with improved performance and rate capability.

Despite the effectiveness of core–shell nanostructure design, a common problem is the rupturing of the outer shell due to increased volume changes after several cycles. To resolve this issue, researchers focused on designing yolk–shell structures, which included the addition of vacant space between the core and shell. By using this WDNs approach, the volumetric expansion can be well accounted for by this void space, without any damage to the Si core.[315] The yolk–shell Si-based nanocomposite design is prone to excessive flow of electrolyte into the void space, which can cause severe side reactions at the Si core–electrolyte interface and lead to the low coulombic efficiency. The WDN design of materials proved to be the solution to this problem, and this approach was reported by Liu et al. on the pomegranate-inspired nanoscale design. In this work, Si NPs were contained in a conductive layer of carbon with enough voids for volume expansion, and it was then further confined in a thicker micrometer-sized carbon layer pouch, which functioned as an electrolyte flooding break wall/obstacle (Figure 25d). This nanoscale design was achieved by a bottom-up microemulsion approach, and it demonstrates the versatility of WDNs to resolve electrochemical issues of electrode materials for rechargeable batteries. Post and in situ analysis confirmed that the SEI layer was stabilized in the composite, the electrode–electrolyte contact area was minimized, and a very high areal capacity of 3.7 mAh cm^{-2} was achieved with an ultra-high volumetric capacity of 1270 mAh cm^{-3}.[323] To address the low tap density of Si-based anode nanomaterials, Lei et al. synthesized a Si-based yolk–shell composite in which Si NPs surrounded by CNT connected Fe_2O_3 NP yolk were encapsulated in two layers of SiO_2 and carbon shell for full cell LIBs. This unique WDNs design addressed the problem of poor electrical conductivity by encapsulating Si NPs with the conductive carbon and high capacity Fe_2O_3. Furthermore, the effective contact between the core and shell is optimized by the CNTs, which link the Fe_2O_3 NPs with the shell, thereby ensuring continuous electronic and ionic transport through the composite (see Figure 25e). An exceedingly high areal capacity of 3.6 mAh cm^{-2} was achieved in half cell LIBs, and 260 mAh g^{-1} was retained in the full cell after 300 cycles.[324] Conclusively, through nano-structuring of silicon-based anodes, improved performance and ultrahigh energy density can be obtained. Bulk and NP based electrodes suffer from poor intercalation and deintercalation while controlling the nanostructured material to obtain core–shell and multi-shelled materials with void space to accommodate the volume expansion will facilitate effective electrolyte penetration and better performance (Figure 25f).[315]

5.5. WDNs for Supercapacitor

Electrochemical capacitors, also known as supercapacitors, are high power density energy storage devices characterized by extensive cycling stability and cycle life. Hence, supercapacitors are often considered a suitable backup to rechargeable batteries and employed in several electronic devices.[325] The classification of supercapacitors can be based on the active materials and the mechanisms of their charge transfer process when applied in a device. To this end, two categories are recognized, namely, electric double-layer capacitors (EDLCs) and pseudo-capacitors. In terms of the charge storage mechanism, the former reversibly adsorb ions from the electrolyte into the active materials, and they are characterized by stable cycle life and large specific surface area. Conversely, in the latter, the storage of ions on the surface of the active materials is initiated by a series of reversible rapid redox reactions. Owing to their characteristic large surface area and accessible porous network, carbon-based materials (graphene, activated carbon, carbon nanotubes, etc.) are often used in the EDLC electrodes, while metal oxides, conductive polymers, etc., are considered as the active materials for pseudo-capacitive capacitors.[326] Rational strategies for improving the specific capacitance and a deeper understanding of electrochemical interlayer in supercapacitors have been the focus of researchers over the years. While the low-cost, large surface area, high pore volume, and stability of the carbon-based materials are attractive for boosting the specific capacitance, the performance is still limited, and a concise understanding of the interfaces at the nanoscale level is lacking. Pseudo-capacitive capacitors tend to deliver superior capacitance, but they are costly and suffer from poor cycle stability. WDNs can provide features that will improve the cycle stability and boost the power and energy density of supercapacitors for energy storage.

5.5.1. Carbon-Based-WDNs for Supercapacitors

Due to their low cost and abundant availability, high surface and pore volume, electrolyte accessibility, and high conductivity, carbon-based materials have shown great promise as active materials for supercapacitors.[327] However, most of the readily available carbon-based materials are limited in delivering the desired performance because of intrinsic properties. For example, although the activated carbon possesses a high surface area, it is limited by its poor mesoporosity, which prevents free-flowing electrolyte penetration, thus limiting its energy density. Furthermore, pore sizes of less than 0.5 nm will be too small for double layer formation, which could result in poor capacitance. Other carbon-based materials such as CNTs and graphene exhibit extremely large surface areas, high conductivity, better mechanical properties as well as high aspect ratio, but their performance still needs to be further improved. Nanostructure engineering of these carbon-based materials is a viable way to tune their properties at the nanoscale and improve their performance. Taking CNTs as an example, An et al. reported the application of a random SWNT network with a capacitance of 180 F g^{-1}, and energy and power density of

10 Wh kg^{-1} and 20 kW kg^{-1}, respectively.[328] Concerned by the low energy and power density of this randomly oriented CNTs, Lu et al. fabricated vertically aligned CNTs with well-defined tube spacing and an interconnected pathway for electrolyte accessibility. These well-aligned nanotubes had opened top endcaps for the multi-directional flow of electrolyte through its internal and external walls. Compared to the disordered 1D-CNTs, the vertically aligned CNTs recorded a superior energy and power density of 148 Wh kg^{-1} and 315 kW kg^{-1}, respectively.[329] This shows that through well-defined nano-structuring and control of the orientation and tip of 1D CNTs, their capacitance and energy density can be significantly improved. Hollow porous carbon materials provide a unique advantage, which is unlike the closed 1D nanostructures; they exhibit multi-directional electrolyte penetration. The synthesis of mesoporous hollow CNTs was reported by using dopamine and ZnO nanorod template (**Figure 26**a). The low-magnification TEM image of the synthesized CNTs (Figure 26b) shows that they are indeed 1D and clustered but not aggregated. Also, the high-magnification TEM (Figure 26c) displays the interior of a single nanotube highlighting the inner walls (17.2 nm thickness), which confirms that they are indeed hollow nanotubes. Interestingly, by tuning the concentration of P-123 used during the synthesis, the authors can control the pore size distribution of the hollow nanotubes and optimize its performance for supercapacitors. Compared to the closed carbon nanotube, which recorded only 208 F g^{-1}, the MCNT delivered a high specific capacitance of 249 F g^{-1} at 0.5 A g^{-1}, and ≈75% capacity was retained at 20 A g^{-1}. This work again shows that by controlling the features of nanostructured materials, their performance can be improved.[330]

Graphene is one of the most attractive carbon-based active materials in supercapacitors because of its high conductivity, large surface area, excellent mechanical stability, and ease of scale-up. Even better, the edge functionalized graphene is easily scaled up to produce graphene with improved properties and higher energy density. Through functionalizing graphene and modifying the edge functional groups, its electronic and mechanical properties can be readily modified, thereby providing more active sites for charge storage and improved capacitance. The combination of nanosized carbon-based materials together to achieve a carbon-based composite is another effective way to boost the capacitance and energy density. However, a WDN does not simply involve a direct combination. A common challenge with graphene is the problem of π–π restacking because this limits the accessibility of its large surface area, resulting in less active sites for surface charge interactions. Du et al. proposed a way to solve this problem by designing a 3D architecture of vertically aligned CNTs (VACNTs) and graphene. Specifically, 1D CNTs were used to separate the layers of the 2D graphene

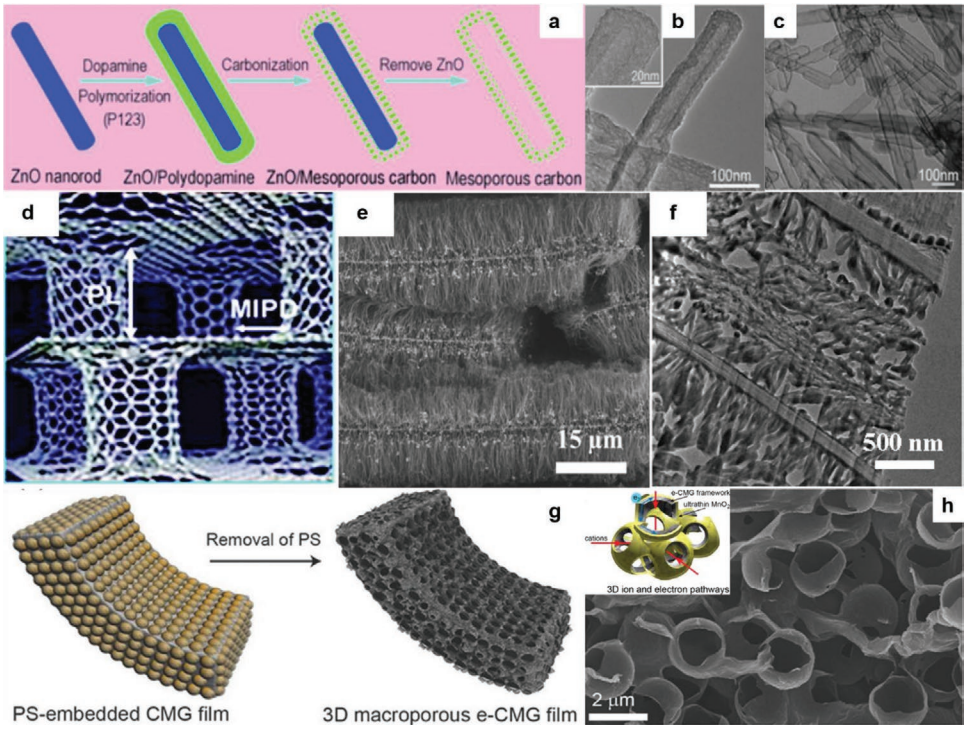

Figure 26. a) Schematic diagram showing the strategy for the synthesis of WDNs, functional mesoporous carbon nanotubes (MCNTs); b) high and c) low magnification TEM images of MCNTs, respectively. Reproduced with permission.[330] Copyright 2011, The Royal Society of Chemistry. d) Schematic representation, e) SEM image, and f) cross-sectional TEM image of the 3D pillared VACNT–graphene architecture. Reproduced with permission.[331] Copyright 2011, American Chemical Society. g) Schematic illustrating a procedure to fabricate 3D macroporous films through an embossing process using PS templates for e-CMG film as well as a subsequent deposition process of MnO_2 for MnO_2/e-CMG film. h) High-magnification cross-sectional SEM images of e-CMG film. Inset illustrates 3D ionic and electronic transport pathways in the MnO_2/e-CMG electrode. Reproduced with permission.[332] Copyright 2012, American Chemical Society.

sheets; by controlling the length and packing density of the VACNTs, they can assemble into the layers of 2D graphene and effectively inhibit restacking in the 3D pillared CNT/graphene architecture (see Figure 26d). In this architecture, the 1D-CNTs pillars mechanically support the graphene layers, prevent the restacking, and provide a continuous pathway for ionic and electronic transport (see Figure 26e,f). The 3D pillared VACNT–graphene architecture delivered an ultra-high capacitance of 1065 F g^{-1}, with ≈4% capacity loss after 20 000 cycles.[331] Choi et al. also reported the polystyrene template synthesis via using a macroporous free-standing chemically modified graphene film (e-CMG) to fabricate a macroporous 3D e-CMG//e-CMG and MnO_2/e-CMG//MnO_2/e-CMG composite electrode for supercapacitor. The macroporous nature of the graphene film was achieved by the removal of the template to generate a series of the interconnected porous network (Figure 26g). The SEM image of the e-CMG film (Figure 26h) shows the pores on the free-standing structure of the carbon matrix. This macroporous assembly facilitated improved conductivity and promoted electrolyte penetration because of the 3D electronic and ionic transport through the composite (see inset, Figure 26h). The composite operated at a high voltage of 2 V, and at 1A g^{-1}, a high specific capacitance of 202 F g^{-1} was delivered as well as a power and energy density of 25 kW kg^{-1} and 44 Wh kg^{-1}.[332] Yu et al. also reported the synthesis of a CNT-graphene fiber with impressive capacitive storage as a promising electrode for supercapacitors. The nanotube fiber was obtained by infusing well-aligned 1D-CNTS in-between layers of N-doped graphene oxide such that they prevent the restacking of GO. The N-doping modulates the conductivity of the composite, and the GO facilitates dispersion of CNTs. Thanks to the controlled synthesis of the composite and fabrication of the electrode material, an ultrahigh conductivity of 102 S cm^{-1} was recorded, and a volumetric energy density of 6.3 mWh cm^{-3} was achieved.[333] Similarly, Fan et al. also reported a 3D CNT-graphene sandwich (CGS) composite where CNT functioned as pillars to prevent the aggregation of graphene, facilitate the electrolyte penetration through the layers, and buffer the composite for volumetric expansion. The CGS composite recorded a specific capacitance of 385 F g^{-1}.[334] Conversely, Xu et al. also reported a graphene-based composite involving conductive polymer—PANI nanowire. In this work, the aggregation and restacking of 2D-graphene oxide sheets were inhibited by systemically arranging vertically aligned PANI nanowire arrays into its layers of GO. The PANI-GO composite exhibited excellent cycle stability and delivered a specific capacitance of up to 555 F g^{-1} and capacity retention of 92% after 2000 cycles.[335] Carbon-based materials have also been used as the binder electrodes as this prevents the coating of insulating material over the conductive carbon matrix from binders used during electrode preparation. Gao et al reported the fabrication of a 3D paper-like graphene framework (3DGF) via a hard template approach. By controlling the pore size and pore structure of the network, the 3DGF framework (the resultant WDNs) enjoyed effective charge transfer, shortened diffusion distance, and limited resistance. To this end, 95 F g^{-1} specific capacitance was recorded along with stable cycle life and rate capability.[336]

5.5.2. Metal Oxide-Based WDNs for Supercapacitors

The challenge of low specific surface area and pore volume distribution limiting the performance of metal oxide active materials has been addressed by using nanostructure design. 1D nanostructured metal oxides have shown great prospects because their unidirectional geometry can serve as a highway for charge migration, and charge transfer distance can be shortened as a result of their smaller boundary diameter. Furthermore, the nanosized dimension can facilitate the rapid transport of solvated ions from the electrolyte to the electrode surface.[337] These 1D nanostructures can be fabricated as nanosphere,[338] nanowire,[232,339,340] and hollow fiber[338] for advanced super capacitance. For example, by using electrospinning, Srinivasan et al. reported the synthesis of 1D $NiCo_2O_4$ hollow nanotubes. The hollow structure of the nanotubes facilitated easy diffusion of ions through the entire active material resulting in improved capacitance of 1647 F g^{-1} at 1 A g^{-1} and excellent cycle stability. Fabrication of electrodes often involves the use of binders, which, however, has been proven to decrease the performance, especially when used as flexible devices. Hence, binder-free electrodes assembled on a substrate which acts as a current collector was deployed. In the case of WDNs, such current collectors provide the electrode with uniform spacing, the larger supporting surface area for efficient charge transfer. Additionally, the electrode–electrolyte interfacial contact can be improved because no "dead surface" is present as a result of binder coating over the electrode, and this improves the performance and cycle life.[326] Array arrangement of such 1D nanostructured materials is a preferred electrode design approach and this was displayed in the work of Wen et al. who reported the ALD synthesis of Pt nanotube arrays. 1D $NiCo_2O_4$ nanoneedles were assembled on the Ni foam substrate and used as a binder-free electrode. Due to the even distribution of the nanoneedles and the improved charge transfer, the electrode delivered impressive specific capacitance and stability.[33] Furthermore, due to the long pore depth and insulative property of alumina, Zhao et al. fabricated the nanoporous Ni arrays by a two-step process of electroplating and electrodeposition (**Figure 27**a). The AAO-like nanoporous Ni arrays were then deployed as a current collector of a Ni/MnO_2 core–shell electrode. As shown in the SEM image of the Ni nanopore arrays after 400 μg cm^{-2} MnO_2 coating (Figure 27b), a uniform and evenly spaced nanoporous assembly can be obtained, which is beneficial for electrolyte penetration. The AAO-like 1D nanoporous Ni arrays provided the electrode a platform for easy electron and charged transport by the various diffusion channels and larger surface area attained. These features enabled the Ni/MnO_2 core–shell electrode to exhibit a high capacitance of 672 F g^{-1} at 2 mV s^{-1} (80 μg cm^{-2} MnO_2 mass loading) and 382 F g^{-1} at 400 μg cm^{-2} mass loading (Figure 27c).[341] The charge storage mechanism of the nanopore arrays (Figure 27d) depicts a multidirectional transport of charges due to the highly oriented arrangement and nanoporous structure.

CNTs, carbon cloth, and other 3D current collectors have also been reported as excellent substrates for active materials as they offer improved conductivity, and they are cheap and safe. A perfect display of this approach is the work of Grote et al. in which an asymmetric supercapacitor consisting of SnO_2 nanotube arrays, 3D core–shell PPy coated SnO_2

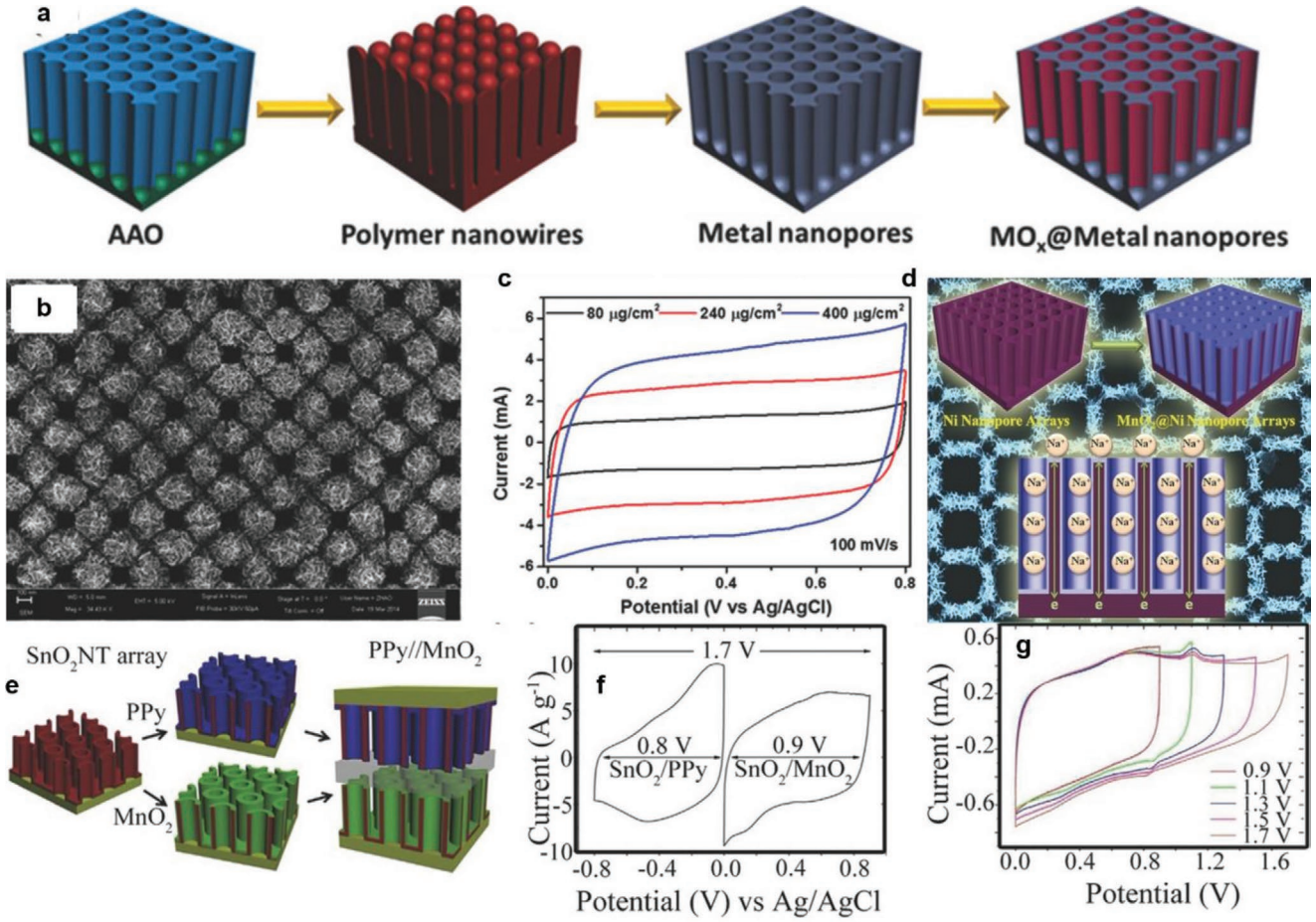

Figure 27. a) Schematic illustration of the fabrication process of metallic nanopore based heterogeneous WDNs. b) SEM image of Ni nanopores after being coated with MnO_2 (400 μg cm^{-1}). c) CV curves of MnO_2@Ni nanopores with different MnO_2 loadings at a scan rate of 100 mV s^{-1}. d) The storage mechanism of the MnO_2@Ni nanopore arrays. Reproduced with permission.[341] Copyright 2014, Wiley-VCH. e) Schematic diagram of the fabrication and assembly of the asymmetric three-dimensional supercapacitor. f) CV curves of single SnO_2/PPy and SnO_2/MnO_2 core-shell NT arrays measured at 20 mV s^{-1} in a three electrode cell, showing the complementary voltage windows of both materials. CV curves of PPy//MnO_2 asymmetric supercapacitor measured at different potential windows from 0.9–1.7 V in a two-electrode cell configuration at 20 mV s^{-1}, exhibiting a mirror-image current response on voltage reversal until 1.7 V. Reproduced with permission.[342] Copyright 2014, Elsevier.

nanotube arrays, and MnO_2 coated SnO_2 nanotube arrays, that is, typical WDNs, were employed as the current collector and negative and positive electrodes, respectively (see Figure 27e). A two-step anodization approach was used for the synthesis of the AAO template, while a scalable AAO-assisted ALD process was used for the synthesis of the current collector. Thanks to the highly effective core–shell nanotube array design of the 3D PPy//MnO_2 asymmetric supercapacitor, while operating at a high voltage of 1.7 V (see Figure 27f), it delivered ultra-high energy and power densities of 27.2 Wh kg^{-1} and 24.8 kW kg^{-1} (Figure 27g).[342] Specific capacitance can also be improved by the heteroatom modification of metal oxide active materials. Such asymmetric active materials benefit from the voltage window of both materials, and this can boost the energy density of the entire electrode. This can also be achieved by combining two metal oxides together, or a metal and a metal oxide, through nanostructured design core–shell heterostructures that can be fabricated and employed as higher-performance electrodes. Wen et al. demonstrated the importance of the core–shell design for improved conductivity and performance by synthesizing MnO_2-coated 1D Pt nanotube arrays for supercapacitor. In this work, the AAO template-assisted ALD process was used to fabricate the electrode, and 1D Pt nanotubes served as the current collector. When the Pt/MnO_2 was used as an electrode for supercapacitor, a specific capacitance of 810 F g^{-1} was attained at 5 mV s^{-1} scan rate, and 68% capacitance was retained when cycled between 2–100 A g^{-1} after 8000 cycles. The core–shell electrode also demonstrated negligible capacity loss and excellent cycle stability. The authors attributed the performance to the improved conductivity and the Pt and rapid ionic transfer validated by the effective electrode–electrolyte contact as a result of the unique core–shell structure design.[343]

Aside from electrochemical supercapacitors, micro-supercapacitors are recently gaining attention as miniaturized electronic devices. Some of the interesting features of such miniaturized supercapacitors include small dimensions and high-power density. Through nanostructured design, micro-supercapacitors

(MSC) can be achieved, and this was proposed by Lei et al. when they reported the downsizing of microminiaturized honeycomb monolith to nanoscale by a nanoindentation–anodization–etching process. Considering the large surface-to-volume ratio and straight/parallel channels of micro-sized honeycomb monoliths,(**Figure 28**a,b), the authors fabricated ultrathin honeycomb alumina monolith scaffolds (HAN), that is, WDNs, by mimicking the structure of natural honeycomb and electrochemically converted them to current collectors (Figure 28c). Such a nanostructured HAN current collector will facilitate effective mass transport across its channels when applied in a supercapacitor. The nanostructured HAN scaffold derived current collector was coated with SnO_2 via ALD to obtain a HAN@SnO_2 nanostructured current collector. This HAN@SnO_2 current collector was then used to design the magnesium oxide (MnO_2)-coated (HAN@SnO_2@MnO_2) and polypyrrole (PPy)-coated (HAN@SnO_2@PPy) nanoelectrodes, respectively. Due to its superior electrical conductivity, the MSC with PPy (HAN@SnO_2@PPy) exhibited less charge transfer resistance and better performance than the one with MnO_2 (HAN@SnO_2@MnO_2). Both electrodes were then used to develop an asymmetric MSC where HAN@SnO_2@PPy functioned as the negative and HAN@SnO_2@MnO_2 served as the positive electrode. The high specific capacitance of 128 mF cm^{-2} was achieved at 0.5 mA cm^{-2} (Figure 28d) along with a high power and energy density of 40 mW cm^{-2} and 160 mW cm^{-2}, respectively.[344] The areal energy density of these micro-supercapacitors is comparable to that of some state-of-the-art 3D micro-batteries but with much higher areal power density (Figure 28e). With such a performance, the micro-supercapacitors shall have the potential for a range of applications from mobile electronics to wireless autonomous sensor networks.

Designing WDNs has proven to be an effective way to improve the performance and resolve some of the critical issues

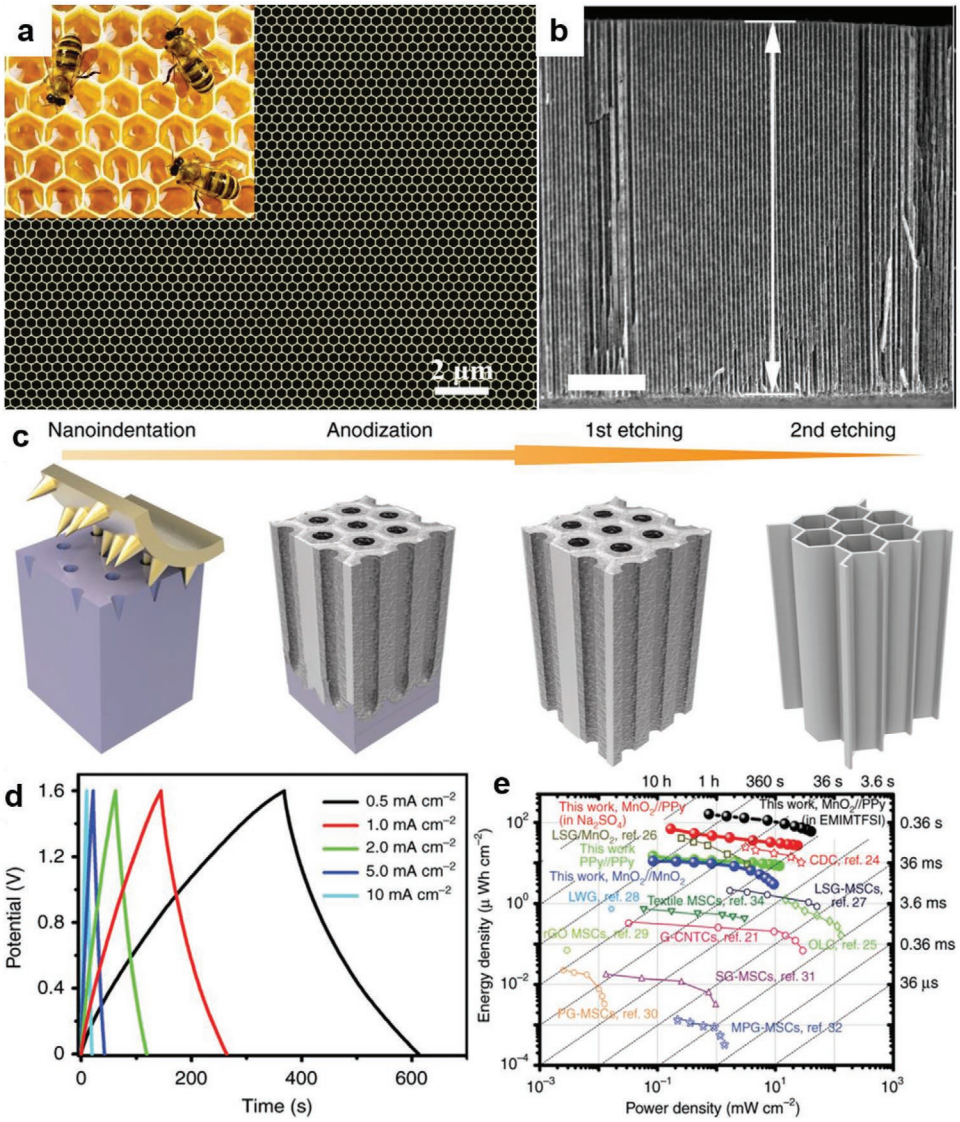

Figure 28. a) The honeycomb-like electrode of HAN/SnO_2. b) Cross-sectional view SEM image of a HAN indicating the cell depth to be about 25 μm. c) Illustration of the HAN fabrication process. d) GCD profiles at different current densities. e) Ragone plots of MSCs with HAN-based nanoelectrodes compared with some reported MSCs. Reproduced with permission.[344] Copyright 2020, Springer Nature.

limiting the large-scale application of energy storage devices. In rechargeable batteries, the problems of inadequate surface area and poor conductivity can be effectively resolved by designing well-defined 2D nanostructures materials. Similarly, the pulverization and volume expansion can be inhibited through the fabrication of core– and yolk–shell nanocomposites. Moreover, WDNs, through multi-dimensional nanocomposite design, the benefits of two different nanomaterials with unique dimensions (e.g., 1D/2D), can be deployed to resolve multiple problems. In supercapacitors, the fabrication of WDNs, such as nanoarrays in a uniform and well-dispersed manner has proven to address the issues of ineffective ion transport, sluggish kinetics, and poor conductivity. Free-standing and binder-free active materials have effectively prevented the formation of inactive "dead surface" and improved the electrode–electrolyte interfacial contact.

6. Conclusions and Future Perspectives

Renewable energy conversion and storage is one of the essential foundations for the sustainable development of our modern society, and it is also one of the most important research and development topics for now and for a long time to come. Academia and industry have been devoting tremendous efforts to developing and commercializing these clean energy technologies, including fuel cells, electrolyzers, photoelectrolyzers, batteries, and supercapacitors. For example, Toyota's Mirai fuel cell vehicles and Tesla's Li-ion battery vehicles have been successfully launched to the market and widely adopted by consumers globally. Nevertheless, the competitiveness of these technologies in terms of performance, stability, sustainability, and cost, still needs to be further enhanced.

Well-defined nanostructures, in terms of extensive modulation of geometric characteristics, including well-defined size, shape, hetero-architecture, and spatial arrangement of nanostructures, benefit both the chemical reaction and the carrier transport, which promote the thermodynamics and kinetics of chemical processes for energy conversion and storage. Therefore, developing WDNs for sustainable energy applications are attracting extensive attention from academia and industry. It is well-established that the WDNs have been largely improving the performance of various clean and sustainable energy devices. The recent rapid development of various advanced characterization techniques, especially for those in the (sub)nanoscale, dramatically facilitates the exploration and understanding of the structure–property relationship between the well-defined nanostructures and their electrochemical (fuel cells, electrolyzers, batteries, and supercapacitors) and PEC performance. Despite much progress, significant gaps still exist between the state-of-the-art technology and consumers' expectations/needs. Here, we list some future perspectives on the research and development of WDNs for devices as follows:

1) Rational design of WDNs, assisted by advanced in situ characterization and theoretical simulation/modeling. As we discussed above in this review, the desired WDNs of various materials from 0D to 3D benefit their related electrochemical and photoelectrochemical reactions. Rational design of WDNs is emphasized in this review because the materials for energy applications should be ideally demand-oriented. That is, the electrodes should be designed based on the specified property parameters of energy conversion and storage devices,[345] such as specific energy density, power density, efficiency, and lifetime in fuel cells, electrolyzers, photoelectrolyzers, batteries, and supercapacitors. To realize the rational design of WDNs, a deep understanding of the mechanisms of reactions and the structure–property relationship of WDNs is required. Unraveling the electrochemical and photoelectrochemical mechanisms is still rather challenging due to the complex nature of the electrochemical processes. As the traditional nanomaterials lack controlled characteristics, WDNs with controllable structures and properties can be regarded as excellent and simplified models for the investigation of electrochemical processes. This generic strategy of building the WDNs provides more possibilities to address the challenges and guide the design of high-performance electrodes. The transition states of chemical intermediates on model electrocatalysts/electrodes and the electrode itself during the electrochemical and photoelectrochemical reactions have to be explored and studied in order to establish the structure–property relationship. This requires precise, accurate, and more challenging in situ characterizations. In particular, the advanced in situ/operando techniques, for example, synchrotron-based X-ray absorption spectroscopy (XAS),[346] TEM,[347] FTIR,[348] Raman,[349] XRD,[350] and mass spectroscopy,[351] have been recently established to capture the changes of both the electrocatalysts/electrodes and the intermediates during the reaction processes. To address the capability limits of the characterization tools, moreover, theoretical simulations (e.g., DFT and thermodynamic modeling) and artificial intelligence (AI) are powerful tools to explain and predict the properties of the WDNs in energy applications and beyond. The knowledge obtained from the ex situ and in situ characterizations and simulation/modeling will provide important feedback and guidance to the rational design of high-performance WDNs.
2) Precisely controlled fabrication of WDNs in tailoring their performance. The electrochemical and PEC reactions usually take place at the surface and interface of electrodes, catalysts, and electrolytes. The so-called "three-phase" interfaces ensure the efficient transportation of electron, mass, ion, etc., while, determining the kinetics of these electrochemical and PEC reactions. Therefore, building well-defined "three-phase" interfaces of the electrodes and catalysts is essential. The WDNs discussed in this review greatly benefit the building and construction of the favorable three-phase interfaces. Based on the knowledge of the rational design of WDNs, various advanced, especially environmentally friendly and cost-effective, synthesis strategies are highly desired for the precisely controlled fabrication of WDNs; for example, the replacement of Pt-based catalysts with carbon-based WDNs in fuel cell application and the substitution of Co-based cathode materials with other transition-metal-based WDNs for batteries application. Various advanced techniques have been applied in the synthesis of WDNs, from microscale to nanoscale in the past years. However, given that the concept of three-phase interfaces is in the molecular and atomic scales,

the more precise control of WDNs is urgently needed, especially in the bottom nanoscale (1–10 nm), sub-nanometer scale, and even molecular/atomic levels.

3) Wide deployment of the low-cost and scalable production of WDNs in sustainable energy devices. Ideally, based on the above two aspects, the community knows what kinds of WDNs are needed and how to rationally fabricate them for various electrochemical and PEC reactions. Another big challenge is how to deploy and integrate these WDNs in sustainable energy conversion and storage devices, as well as their broad commercialization. Much progress on the precisely controlled fabrication of WDNs has been achieved, while the yield of WDNs is still not satisfied, which leads to difficulties in the scale-up production of the WDNs. Besides, the fabrication of WDNs usually costs more than the synthesis of traditional nanomaterials. Thus, lowering the cost should be considered as well. In this regard, the development of low-cost and mass-production strategies/techniques for the scaling up of WDNs from lab to the industrial scale is highly desired. Further, the novel stack and/or pack design of these energy devices has to be further continued, to meet the urgent requirements of safety, high power density, and energy density. Last but not the least, the lifetime of these electrochemical energy devices, that is, material and device stability, is still insufficient. WDNs are promising to improve stability due to the strengthened skeletons and frameworks.[352] However, they still need further improvement, especially for operating under harsh electrochemical conditions.[172,353–355] Understanding the degradation mechanisms as well as how the WDNs benefit the material and device stability should be paid more attention.[356,357] Again, the advanced in situ/operando characterizations with high resolution are powerful in monitoring the catalyst and electrode changes during practical device working conditions. Theoretical calculations and AI can assist the understanding of aging and failing mechanisms of the devices.

In summary, based on the above discussions, future scientific research and developments of WDNs are highly desired, yet, challenging. As such, intensively national and, especially, international collaborations among research groups, institutions, and industries are critical to addressing the needs of sustainable energy. It has been demonstrated in the past decades that many international collaborations have produced breakthrough discoveries, creations, and inventions in the fields of functional nanostructures for high-performance fuel cells, electrolyzers, photoelectrolyzers, batteries, and supercapacitors. The comprehensive and efficient international collaborations on this aspect will further promote and more importantly accelerate the development of a low-carbon footprint society built on sustainable materials and energy technologies.

Acknowledgements

R.X., L.D., D.A., and G.Z. contributed equally to this work. R.X. and Y.L. acknowledge the financial support from the German Research Foundation (DFG: LE 2249/5-1) and Chinesisch-Deutsches Zentrum für Wissenschaftsförderung (GZ 1579). D.A. and S.Z. acknowledge the financial support from the Australian Research Council (ARC) Discovery Projects (DP160102627 and DP1701048343) and Griffith University Ph.D. scholarship awards. L.D., G.Z., and S.S. acknowledge the financial support from the Natural Sciences and Engineering Research Council of Canada (NSERC), Fonds de Recherche du Québec-Nature et Technologies (FRQNT). L.D. thanks the FRQNT Postdoctoral scholarship.

Conflict of Interest

The authors declare no conflict of interest.

Keywords

electrochemical, energy conversion, energy storage, nanostructures, well-defined geometries

Received: May 5, 2020
Published online:

[1] S. Chu, A. Majumdar, *Nature* **2012**, *488*, 294.
[2] Z. P. Cano, D. Banham, S. Ye, A. Hintennach, J. Lu, M. Fowler, Z. Chen, *Nat. Energy* **2018**, *3*, 279.
[3] J. Herranz, J. Durst, E. Fabbri, A. Patru, X. Cheng, A. A. Permyakova, T. J. Schmidt, *Nano Energy* **2016**, *29*, 4.
[4] Y.-G. Guo, J.-S. Hu, L.-J. Wan, *Adv. Mater.* **2008**, *20*, 2878.
[5] M. Pumera, *Energy Environ. Sci.* **2011**, *4*, 668.
[6] X. Chen, C. Li, M. Gratzel, R. Kostecki, S. S. Mao, *Chem. Soc. Rev.* **2012**, *41*, 7909.
[7] Q. Zhang, E. Uchaker, S. L. Candelaria, G. Cao, *Chem. Soc. Rev.* **2013**, *42*, 3127.
[8] Z. Y. Zhou, N. Tian, J. T. Li, I. Broadwell, S. G. Sun, *Chem. Soc. Rev.* **2011**, *40*, 4167.
[9] L. Dai, D. W. Chang, J. B. Baek, W. Lu, *Small* **2012**, *8*, 1130.
[10] A. S. Arico, P. Bruce, B. Scrosati, J. M. Tarascon, W. van Schalkwijk, *Nat. Mater.* **2005**, *4*, 366.
[11] M. Zhou, Y. Xu, Y. Lei, *Nano Today* **2018**, *20*, 33.
[12] R. Kant, J. Kaur, M. B. Singh, *Electrochemistry* **2013**, *12*, 336.
[13] I. Hasa, J. Hassoun, S. Passerini, *Nano Res.* **2017**, *10*, 3942.
[14] F. E. Osterloh, *Chem. Soc. Rev.* **2013**, *42*, 2294.
[15] P. Warrier, A. Teja, *Nanoscale Res. Lett.* **2011**, *6*, 247.
[16] C. Reale, *Czech. J. Phys.* **1971**, *21*, 662.
[17] A. W. Cohn, A. M. Schimpf, C. E. Gunthardt, D. R. Gamelin, *Nano Lett.* **2013**, *13*, 1810.
[18] P. Balaya, A. J. Bhattacharyya, J. Jamnik, Y. F. Zhukovskii, E. A. Kotomin, J. Maier, *J. Power Sources* **2006**, *159*, 171.
[19] P. G. Bruce, B. Scrosati, J. M. Tarascon, *Angew. Chem., Int. Ed.* **2008**, *47*, 2930.
[20] C. Clavero, *Nat. Photonics* **2014**, *8*, 95.
[21] P. Poizot, S. Laruelle, S. Grugeon, L. Dupont, J. Tarascon, *Nature* **2000**, *407*, 496.
[22] T. Takagahara, K. Takeda, *Phys. Rev. B* **1992**, *46*, 15578.
[23] K. F. Lin, H. M. Cheng, H. C. Hsu, L. J. Lin, W. F. Hsieh, *Chem. Phys. Lett.* **2005**, *409*, 208.
[24] L. S. Li, J. T. Hu, W. D. Yang, A. P. Alivisatos, *Nano Lett.* **2001**, *1*, 349.
[25] L. A. Swafford, L. A. Weigand, M. J. Bowers, J. R. McBride, J. L. Rapaport, T. L. Watt, S. K. Dixit, L. C. Feldman, S. J. Rosenthal, *J. Am. Chem. Soc.* **2006**, *128*, 12299.
[26] M. Liu, Y. J. Pang, B. Zhang, P. De Luna, O. Voznyy, J. X. Xu, X. L. Zheng, C. T. Dinh, F. J. Fan, C. H. Cao, F. P. G. de Arquer, T. S. Safaei, A. Mepham, A. Klinkova, E. Kumacheva, T. Filleter, D. Sinton, S. O. Kelley, E. H. Sargent, *Nature* **2016**, *537*, 382.

[27] C. F. Guo, T. Y. Sun, F. Cao, Q. Liu, Z. F. Ren, *Light: Sci. Appl.* **2014**, *3*, e161.
[28] M. L. Brongersma, Y. Cui, S. H. Fan, *Nat. Mater.* **2014**, *13*, 451.
[29] X. S. Hua, Y. J. Zhang, H. W. Wang, *Sol. Energy Mater. Sol. Cells* **2010**, *94*, 258.
[30] L. L. Huang, M. Liu, H. X. Lin, Y. B. Xu, J. S. Wu, V. P. Dravid, C. Wolverton, C. A. Mirkin, *Science* **2019**, *365*, 1159.
[31] A. S. Barnard, *Cryst. Growth Des.* **2009**, *9*, 4860.
[32] J. Li, Y. Qiu, Z. Wei, Q. Lin, Q. Zhang, K. Yan, H. Chen, S. Xiao, Z. Fan, S. Yang, *Energy Environ. Sci.* **2014**, *7*, 3651.
[33] K. A. Arpin, A. Mihi, H. T. Johnson, A. J. Baca, J. A. Rogers, J. A. Lewis, P. V. Braun, *Adv. Mater.* **2010**, *22*, 1084.
[34] M. Seo, T. D. Chung, *Curr. Opin. Electrochem.* **2019**, *13*, 47.
[35] X. Y. Lu, Y. Yin, L. Zhang, L. X. Xi, S. Oswald, J. W. Deng, O. G. Schmidt, *Nano Energy* **2016**, *30*, 69.
[36] S. Choi, J. I. Lee, S. Park, *J. Mater. Chem.* **2012**, *22*, 22366.
[37] V. R. Manfrinato, L. Zhang, D. Su, H. Duan, R. G. Hobbs, E. A. Stach, K. K. Berggren, *Nano Lett.* **2013**, *13*, 1555.
[38] Q. P. McAllister, K. E. Strawhecker, C. R. Becker, C. A. Lundgren, *J. Power Sources* **2014**, *257*, 380.
[39] D. Zhuang, J. H. Edgar, *Mater. Sci. Eng.: R: Rep.* **2005**, *48*, 1.
[40] H. Jiang, X. Zhou, G. G. Liu, Y. H. Zhou, H. Q. Ye, Y. Liu, K. Han, *Electrochim. Acta* **2016**, *188*, 777.
[41] R. You, X. D. Hao, H. Y. Yu, B. X. Wang, G. Y. Lu, F. M. Liu, T. H. Cui, *Sens. Actuators, B* **2018**, *263*, 445.
[42] G. Nanda, G. Hlawacek, S. Goswami, K. Watanabe, T. Taniguchi, P. F. A. Alkemade, *Carbon* **2017**, *119*, 419.
[43] W. H. Chen, F. C. N. Hong, *Sol. Energy Mater. Sol. Cells* **2016**, *157*, 48.
[44] W. Y. Shang, G. Q. Gu, F. Yang, L. Zhao, G. Cheng, Z. L. Du, Z. L. Wang, *ACS Nano* **2017**, *11*, 8796.
[45] H. T. Soh, K. W. Guarini, C. F. Quate, *Scanning Probe Lithography*, Vol. *7*, Springer Science & Business Media, Berlin **2013**.
[46] R. Becker, J. Golovchenko, B. Swartzentruber, *Nature* **1987**, *325*, 419.
[47] V. Bouchiat, *Nano-Lithography* (Ed: S. Landis), Wiley, New York **2013**.
[48] S. Y. Chou, P. R. Krauss, P. J. Renstrom, *Appl. Phys. Lett.* **1995**, *67*, 3114.
[49] N. Vigneswaran, F. Samsuri, B. Ranganathan, *Proc. Eng.* **2014**, *97*, 1387.
[50] Y. Y. Kim, H. J. Kim, J. H. Jeong, J. Lee, J. H. Choi, J. Y. Jung, J. H. Lee, H. Cheng, K. W. Lee, D. G. Choi, *Adv. Eng. Mater.* **2016**, *18*, 1349.
[51] E. H. Kil, K. H. Choi, H. J. Ha, S. Xu, J. A. Rogers, M. R. Kim, Y. G. Lee, K. M. Kim, K. Y. Cho, S. Y. Lee, *Adv. Mater.* **2013**, *25*, 1395.
[52] Q. Dong, G. J. Li, C. L. Ho, M. Faisal, C. W. Leung, P. W. T. Pong, K. Liu, B. Z. Tang, I. Manners, W. Y. Wong, *Adv. Mater.* **2012**, *24*, 1034.
[53] L. H. Wu, Q. Li, C. H. Wu, H. Y. Zhu, A. Mendoza-Garcia, B. Shen, J. H. Guo, S. H. Sun, *J. Am. Chem. Soc.* **2015**, *137*, 7071.
[54] C. Wang, L. X. Wu, H. Wang, W. H. Zuo, Y. Y. Li, J. P. Liu, *Adv. Funct. Mater.* **2015**, *25*, 3524.
[55] C. Y. Zhao, X. Wang, J. H. Kong, J. M. Ang, P. S. Lee, Z. L. Liu, X. H. Lu, *ACS Appl. Mater. Interfaces* **2016**, *8*, 2372.
[56] B. Cai, D. Wen, W. Liu, A. K. Herrmann, A. Benad, A. Eychmuller, *Angew. Chem., Int. Ed.* **2015**, *54*, 13101.
[57] C. Wang, W. Wan, Y. H. Huang, J. T. Chen, H. H. Zhou, X. X. Zhang, *Nanoscale* **2014**, *6*, 5351.
[58] C. W. Lee, S. D. Seo, D. W. Kim, S. Park, K. Jin, D. W. Kim, K. S. Hong, *Nano Res.* **2013**, *6*, 348.
[59] K. C. Poon, D. C. L. Tan, T. D. T. Vo, B. Khezri, H. B. Su, R. D. Webster, H. Sato, *J. Am. Chem. Soc.* **2014**, *136*, 5217.
[60] M. Y. Hua, C. Liu, S. Yang, S. H. Liu, K. Fu, Z. H. Dong, Y. Cai, B. S. Zhang, K. J. Chen, *IEEE Electron Device Lett.* **2015**, *36*, 448.
[61] M. B. E. Griffiths, S. E. Koponen, D. J. Mandia, J. F. McLeod, J. P. Coyle, J. J. Sims, J. B. Giorgi, E. R. Sirianni, G. P. A. Yap, S. T. Barry, *Chem. Mater.* **2015**, *27*, 6116.
[62] Y. Li, S. L. Yu, T. Z. Yuan, M. Yan, Y. Z. Jiang, *J. Power Sources* **2015**, *282*, 1.
[63] Z. J. Fan, J. Yan, T. Wei, G. Q. Ning, L. J. Zhi, J. C. Liu, D. X. Cao, G. L. Wang, F. Wei, *ACS Nano* **2011**, *5*, 2787.
[64] S. L. Jiang, Z. P. Zhang, N. Zhang, Y. H. Huan, Y. Gong, M. X. Sun, J. P. Shi, C. Y. Xie, P. F. Yang, Q. Y. Fang, H. Li, L. M. Tong, D. Xie, L. Gu, P. R. Liu, Y. F. Zhang, *Nano Res.* **2018**, *11*, 1787.
[65] Y. Mi, L. Y. Wen, R. Xu, Z. J. Wang, D. W. Cao, Y. G. Fang, Y. Lei, *Adv. Energy Mater.* **2016**, *6*, 1501496.
[66] L. Y. Wen, M. Zhou, C. L. Wang, Y. Mi, Y. Lei, *Adv. Energy Mater.* **2016**, *6*, 1600468.
[67] M. B. E. Griffiths, P. J. Pallister, D. J. Mandia, S. T. Barry, *Chem. Mater.* **2016**, *28*, 44.
[68] A. C. Kozen, C. F. Lin, A. J. Pearse, M. A. Schroeder, X. G. Han, L. B. Hu, S. B. Lee, G. W. Rubloff, M. Noked, *ACS Nano* **2015**, *9*, 5884.
[69] F. Yu, L. Du, G. Zhang, F. Su, W. Wang, S. Sun, *Adv. Funct. Mater.* **2020**, *30*, 1906890.
[70] N. P. Dasgupta, X. B. Meng, J. W. Elam, A. B. F. Martinson, *Acc. Chem. Res.* **2015**, *48*, 341.
[71] W. Xiong, Q. Guo, Z. Guo, H. Li, R. Zhao, Q. Chen, Z. W. Liu, X. W. Wang, *J. Mater. Chem. A* **2018**, *6*, 4297.
[72] X. Meng, Y. C. Byun, H. S. Kim, J. S. Lee, A. T. Lucero, L. X. Cheng, J. Kim, *Materials* **2016**, *9*, 1007.
[73] J. Kumar, P. Kichambare, A. K. Rai, R. Bhattacharya, S. Rodrigues, G. Subramanyam, *J. Power Sources* **2016**, *301*, 194.
[74] R. Xu, X. D. Wang, L. Song, W. Liu, A. Ji, F. H. Yang, J. M. Li, *Opt. Express* **2012**, *20*, 5061.
[75] Y. Lei, S. K. Yang, M. H. Wu, G. Wilde, *Chem. Soc. Rev.* **2011**, *40*, 1247.
[76] Z. J. Wang, D. W. Cao, R. Xu, S. C. Qu, Z. G. Wang, Y. Lei, *Nano Energy* **2016**, *19*, 328.
[77] H. Masuda, K. Fukuda, *Science* **1995**, *268*, 1466.
[78] Y. Lei, W. P. Cai, G. Wilde, *Prog. Mater. Sci.* **2007**, *52*, 465.
[79] H. Asoh, K. Nishio, M. Nakao, A. Yokoo, T. Tamamura, H. Masuda, *J. Vac. Sci. Technol. B: Microelectron. Nanometer Struct.* **2001**, *19*, 569.
[80] L. Wen, R. Xu, Y. Mi, Y. Lei, *Nat. Nanotechnol.* **2017**, *12*, 244.
[81] F. Han, G. Meng, F. Zhou, L. Song, X. Li, X. Hu, X. Zhu, B. Wu, B. Wei, *Sci. Adv.* **2015**, *1*, e1500605.
[82] Q. Fu, Z. B. Zhan, J. X. Dou, X. Z. Zheng, R. Xu, M. H. Wu, Y. Lei, *ACS Appl. Mater. Interfaces* **2015**, *7*, 13322.
[83] L. J. Zheng, D. C. Yang, R. Chang, C. W. Wang, G. X. Zhang, S. H. Sun, *Nanoscale* **2017**, *9*, 8918.
[84] S. Tarish, A. Al-Haddad, R. Xu, D. W. Cao, Z. J. Wang, S. C. Qu, G. Nabi, Y. Lei, *J. Mater. Chem. C* **2016**, *4*, 1369.
[85] Y. Xu, M. Zhou, C. L. Zhang, C. L. Wang, L. Y. Liang, Y. G. Fang, M. H. Wu, L. Cheng, Y. Lei, *Nano Energy* **2017**, *38*, 304.
[86] Y. Yu, X. J. Wu, M. Zhao, Q. Ma, J. Chen, B. Chen, M. Sindoro, J. Yang, S. Han, Q. Lu, H. Zhang, *Angew. Chem., Int. Ed.* **2017**, *56*, 578.
[87] Z. Zhan, F. Grote, Z. Wang, R. Xu, Y. Lei, *Adv. Energy Mater.* **2015**, *5*, 1501654.
[88] Z. B. Zhan, R. Xu, X. Z. Zheng, Q. Fu, M. H. Wu, Y. Lei, *Nanotechnology* **2016**, *27*, 445301.
[89] L. Y. Wen, Z. J. Wang, Y. Mi, R. Xu, S. H. Yu, Y. Lei, *Small* **2015**, *11*, 3408.
[90] S. P. Xu, H. P. Zhao, Y. Xu, R. Xu, Y. Lei, *ACS Appl. Mater. Interfaces* **2018**, *10*, 13895.
[91] R. Xu, H. P. Zhao, H. L. Jin, Z. J. Wang, Z. L. Zhang, S. P. Xu, Z. Q. Zeng, S. Wang, Y. Lei, *Nano Energy* **2019**, *58*, 543.
[92] R. Xu, L. Wen, Z. Wang, H. Zhao, S. Xu, Y. Mi, Y. Xu, M. Sommerfeld, Y. Fang, Y. Lei, *ACS Nano* **2017**, *11*, 7382.

[93] X. T. Wang, C. Liow, D. P. Qi, B. W. Zhu, W. R. Leow, H. Wang, C. Xue, X. D. Chen, S. Z. Li, *Adv. Mater.* **2014**, *26*, 3506.
[94] T. Ozel, G. R. Bourret, C. A. Mirkin, *Nat. Nanotechnol.* **2015**, *10*, 319.
[95] G. H. Chan, J. Zhao, E. M. Hicks, G. C. Schatz, R. P. Van Duyne, *Nano Lett.* **2007**, *7*, 1947.
[96] Y. Li, T. Sasaki, Y. Shimizu, N. Koshizaki, *J. Am. Chem. Soc.* **2008**, *130*, 14755.
[97] X. Zhang, E. M. Hicks, J. Zhao, G. C. Schatz, R. P. Van Duyne, *Nano Lett.* **2005**, *5*, 1503.
[98] G. Tian, D. Chen, H. Fan, P. Li, Z. Fan, M. Qin, M. Zeng, J. Dai, X. Gao, J.-M. Liu, *ACS Appl. Mater. Interfaces* **2017**, *9*, 37219.
[99] S. P. Xu, Y. Xu, H. P. Zhao, R. Xu, Y. Lei, *ACS Appl. Mater. Interfaces* **2018**, *10*, 29092.
[100] L. Cao, J. Qi, Q. Wu, Z. Li, R. Wang, J. Chen, Y. Lu, W. Zhao, J. Yao, X. Yu, *Nanoscale Res. Lett.* **2019**, *14*, 388.
[101] S. Kasani, P. Zheng, N. Wu, *J. Phys. Chem. C* **2018**, *122*, 13443.
[102] J. Li, S. K. Cushing, P. Zheng, F. Meng, D. Chu, N. Wu, *Nat. Commun.* **2013**, *4*, 2651.
[103] S. L. Cheng, H. C. Lin, Y. H. Huang, S. C. Yang, *RSC Adv.* **2017**, *7*, 23935.
[104] M. Zhou, Y. Xu, C. Wang, Q. Li, J. Xiang, L. Liang, M. Wu, H. Zhao, Y. Lei, *Nano Energy* **2017**, *31*, 514.
[105] M. Zhou, Y. Xu, J. X. Xiang, C. L. Wang, L. Y. Liang, L. Y. Wen, Y. G. Fang, Y. Mi, Y. Lei, *Adv. Energy Mater.* **2016**, *6*, 1600448.
[106] M. Zhou, H. B. Wu, J. Bao, L. Liang, X. W. Lou, Y. Xie, *Angew. Chem., Int. Ed.* **2013**, *52*, 8579.
[107] Z. Pu, I. S. Amiinu, R. Cheng, P. Wang, C. Zhang, S. Mu, W. Zhao, F. Su, G. Zhang, S. Liao, S. Sun, *Nano-Micro Lett.* **2020**, *12*, 21.
[108] Z. Pu, T. Liu, W. Zhao, X. Shi, Y. Liu, G. Zhang, W. Hu, S. Sun, S. Liao, *ACS Appl. Mater. Interfaces* **2020**, *12*, 11737.
[109] M. Wu, Q. Wei, G. Zhang, J. Qiao, M. Wu, J. Zhang, Q. Gong, S. Sun, *Adv. Energy Mater.* **2018**, *8*, 1801836.
[110] M. Wu, G. Zhang, N. Chen, W. Chen, J. Qiao, S. Sun, *Energy Storage Mater.* **2020**, *24*, 272.
[111] M. Wu, G. Zhang, J. Qiao, N. Chen, W. Chen, S. Sun, *Nano Energy* **2019**, *61*, 86.
[112] M. Wu, G. Zhang, M. Wu, J. Prakash, S. Sun, *Energy Storage Mater.* **2019**, *21*, 253.
[113] S. Sun, G. Zhang, X. Sun, M. Cai, M. Ruthkosky, *J. Nanotechnol.* **2012**, *2012*, 389505.
[114] X. Tong, J. Zhang, G. Zhang, Q. Wei, R. Chenitz, J. P. Claverie, S. Sun, *Chem. Mater.* **2017**, *29*, 9579.
[115] Q. Wei, M. Cherif, G. Zhang, A. Almesrati, J. Chen, M. Wu, N. Komba, Y. Hu, T. Regier, T.-K. Sham, F. Vidal, S. Sun, *Nano Energy* **2019**, *62*, 700.
[116] Q. Wei, Y. Fu, G. Zhang, S. Sun, *Curr. Opin. Electrochem.* **2017**, *4*, 45.
[117] Z. W. Seh, J. Kibsgaard, C. F. Dickens, I. Chorkendorff, J. K. Nørskov, T. F. Jaramillo, *Science* **2017**, *355*, eaad4998.
[118] C. Wang, W. Chen, D. Yuan, S. Qian, D. Cai, J. Jiang, S. Zhang, *Nano Energy* **2020**, *69*, 104453.
[119] L. Du, S. Lou, G. Chen, G. Zhang, F. Kong, Z. Qian, C. Du, Y. Gao, S. Sun, G. Yin, *J. Power Sources* **2019**, *433*, 126690.
[120] Z. Chen, G. Zhang, J. Prakash, Y. Zheng, S. Sun, *Adv. Energy Mater.* **2019**, *9*, 1900889.
[121] H. Yang, Y. w. Hu, J. j. Chen, M. S. Balogun, P. p. Fang, S. Zhang, J. Chen, Y. Tong, *Adv. Energy Mater.* **2019**, *9*, 1901396.
[122] L. Du, Y. Y. Shao, J. M. Sun, G. P. Yin, C. Y. Du, Y. Wang, *Catal. Sci. Technol.* **2018**, *8*, 3216.
[123] Y. Zhao, B. P. Setzler, J. Wang, J. Nash, T. Wang, B. Xu, Y. Yan, *Joule* **2019**, *3*, 2472.
[124] L. Liu, D. Li, H. Zhao, A. Dimitrova, L. Li, Y. Fang, S. Krischok, W. Shi, Y. Lei, *Appl. Catal., B* **2019**, *244*, 87.
[125] Q. Jia, K. Caldwell, K. Strickland, J. M. Ziegelbauer, Z. Liu, Z. Yu, D. E. Ramaker, S. Mukerjee, *ACS Catal.* **2015**, *5*, 176.
[126] M. Li, Z. Zhao, T. Cheng, A. Fortunelli, C. Y. Chen, R. Yu, Q. Zhang, L. Gu, B. V. Merinov, Z. Lin, E. Zhu, T. Yu, Q. Jia, J. Guo, L. Zhang, W. A. Goddard, Y. Huang, X. Duan, *Science* **2016**, *354*, 1414.
[127] Y. Liu, L. Du, F. Kong, G. Han, Y. Gao, C. Du, P. Zuo, G. Yin, *ACS Sustainable Chem. Eng.* **2020**, *8*, 1295.
[128] Y. Takasu, N. Ohashi, X. G. Zhang, Y. Murakami, H. Minagawa, S. Sato, K. Yahikozawa, *Electrochim. Acta* **1996**, *41*, 2595.
[129] K. Yu, D. J. Groom, X. Wang, Z. Yang, M. Gummalla, S. C. Ball, D. J. Myers, P. J. Ferreira, *Chem. Mater.* **2014**, *26*, 5540.
[130] E. F. Holby, W. Sheng, Y. Shao-Horn, D. Morgan, *Energy Environ. Sci.* **2009**, *2*, 865.
[131] L. Du, F. P. Kong, G. Y. Chen, C. Y. Du, Y. Z. Gao, G. P. Yin, *Chin. J. Catal.* **2016**, *37*, 1025.
[132] Z. Zeng, R. Xu, H. Zhao, H. Zhang, L. Liu, S. Xu, Y. Lei, *Mater. Today Nano* **2018**, *3*, 54.
[133] J. Park, J. C. Hwang, G. G. Kim, J. U. Park, *InfoMat* **2020**, *2*, 33.
[134] M. Gong, Z. Deng, D. Xiao, L. Han, T. Zhao, Y. Lu, T. Shen, X. Liu, R. Lin, T. Huang, G. Zhou, H. Xin, D. Wang, *ACS Catal.* **2019**, *9*, 4488.
[135] R. Borup, *Fuel Cell Performance and Durability Consortium, US DOE 2018 Annual Merit Review Proc.* **2018**, https://www.hydrogen.energy.gov/pdfs/review18/fc135_borup_2018_o.pdf (accessed: June 2018).
[136] Y. P. Zuo, L. Wu, K. Cai, T. T. Li, W. M. Yin, D. Li, N. Li, J. W. Liu, H. Y. Han, *ACS Appl. Mater. Interfaces* **2015**, *7*, 17725.
[137] C. Wang, Y. Hou, J. Kim, S. Sun, *Angew. Chem., Int. Ed.* **2007**, *46*, 6333.
[138] M. Luo, Z. Zhao, Y. Zhang, Y. Sun, Y. Xing, F. Lv, Y. Yang, X. Zhang, S. Hwang, Y. Qin, J. Y. Ma, F. Lin, D. Su, G. Lu, S. Guo, *Nature* **2019**, *574*, 81.
[139] S. Park, Y. Shao, H. Wan, P. C. Rieke, V. V. Viswanathan, S. A. Towne, L. V. Saraf, J. Liu, Y. Lin, Y. Wang, *Electrochem. Commun.* **2011**, *13*, 258.
[140] S. Zhao, Y. Wang, J. Dong, C.-T. He, H. Yin, P. An, K. Zhao, X. Zhang, C. Gao, L. Zhang, J. Lv, J. Wang, J. Zhang, A. M. Khattak, N. A. Khan, Z. Wei, J. Zhang, S. Liu, H. Zhao, Z. Tang, *Nat. Energy* **2016**, *1*, 16184.
[141] L. Du, Y. Y. Shao, J. M. Sun, G. P. Yin, J. Liu, Y. Wang, *Nano Energy* **2016**, *29*, 314.
[142] W. Sun, L. Du, C. Du, Y. Gao, G. Yin, *Appl. Surf. Sci.* **2019**, *485*, 41.
[143] S. Guo, S. Dong, E. Wang, *ACS Nano* **2010**, *4*, 547.
[144] M. A. Hoque, F. M. Hassan, D. Higgins, J.-Y. Choi, M. Pritzker, S. Knights, S. Ye, Z. Chen, *Adv. Mater.* **2015**, *27*, 1229.
[145] J. Park, Y. J. Sa, H. Baik, T. Kwon, S. H. Joo, K. Lee, *ACS Nano* **2017**, *11*, 5500.
[146] L. Xu, Z. Luo, Z. Fan, S. Yu, J. Chen, Y. Liao, C. Xue, *Chem. - Eur. J.* **2015**, *21*, 8691.
[147] S. Zhao, H. Yin, L. Du, G. Yin, Z. Tang, S. Liu, *J. Mater. Chem. A* **2014**, *2*, 3719.
[148] S. Chen, Z. Niu, C. Xie, M. Gao, M. Lai, M. Li, P. Yang, *ACS Nano* **2018**, *12*, 8697.
[149] C. Chen, Y. Kang, Z. Huo, Z. Zhu, W. Huang, H. L. Xin, J. D. Snyder, D. Li, J. A. Herron, M. Mavrikakis, M. Chi, K. L. More, Y. Li, N. M. Markovic, G. A. Somorjai, P. Yang, V. R. Stamenkovic, *Science* **2014**, *343*, 1339.
[150] L. Du, C. Du, G. Chen, F. Kong, G. Yin, Y. Wang, *ACS Appl. Mater. Interfaces* **2016**, *8*, 15250.
[151] N. M. Markovic, H. A. Gasteiger, P. N. Ross, *J. Phys. Chem.* **1995**, *99*, 3411.
[152] N. Markovic, H. Gasteiger, P. N. Ross, *J. Electrochem. Soc.* **1997**, *144*, 1591.
[153] L. Du, S. Zhang, G. Chen, G. Yin, C. Du, Q. Tan, Y. Sun, Y. Qu, Y. Gao, *ACS Appl. Mater. Interfaces* **2014**, *6*, 14043.
[154] T. S. Ahmadi, Z. L. Wang, T. C. Green, A. Henglein, M. A. El-Sayed, *Science* **1996**, *272*, 1924.

[155] N. Tian, Z. Y. Zhou, S. G. Sun, Y. Ding, Z. L. Wang, *Science* **2007**, *316*, 732.
[156] J. Xiao, S. Liu, N. Tian, Z. Y. Zhou, H. X. Liu, B. B. Xu, S. G. Sun, *J. Am. Chem. Soc.* **2013**, *135*, 18754.
[157] Y. Qin, X. Zhang, X. Dai, H. Sun, Y. Yang, X. Li, Q. Shi, D. Gao, H. Wang, N.-F. Yu, S.-G. Sun, *Small* **2016**, *12*, 524.
[158] J. Li, S. Sharma, X. Liu, Y.-T. Pan, J. S. Spendelow, M. Chi, Y. Jia, P. Zhang, D. A. Cullen, Z. Xi, H. Lin, Z. Yin, B. Shen, M. Muzzio, C. Yu, Y. S. Kim, A. A. Peterson, K. L. More, H. Zhu, S. Sun, *Joule* **2019**, *3*, 124.
[159] Z. Xia, S. Guo, *Chem. Soc. Rev.* **2019**, *48*, 3265.
[160] V. R. Stamenkovic, B. Fowler, B. S. Mun, G. Wang, P. N. Ross, C. A. Lucas, N. M. Markovic, *Science* **2007**, *315*, 493.
[161] F. Kong, Z. Ren, M. Norouzi Banis, L. Du, X. Zhou, G. Chen, L. Zhang, J. Li, S. Wang, M. Li, K. Doyle-Davis, Y. Ma, R. Li, A. P. Young, L. Yang, M. Markiewicz, Y. Tong, G. Yin, C. Du, J. Luo, X. Sun, *ACS Catal.* **2020**, *10*, 4205.
[162] G. Chen, K. A. Kuttiyiel, M. Li, D. Su, L. Du, C. Du, Y. Gao, W. Fei, G. Yin, K. Sasaki, R. R. Adzic, *J. Mater. Chem. A* **2018**, *6*, 20725.
[163] X. Ji, P. Gao, L. Zhang, X. Wang, F. Wang, H. Zhu, J. Yu, *ChemElectroChem* **2019**, *6*, 3065.
[164] D. Liu, X. Li, S. Chen, H. Yan, C. Wang, C. Wu, Y. A. Haleem, S. Duan, J. Lu, B. Ge, P. M. Ajayan, Y. Luo, J. Jiang, L. Song, *Nat. Energy* **2019**, *4*, 512.
[165] S. Sun, G. Zhang, N. Gauquelin, N. Chen, J. Zhou, S. Yang, W. Chen, X. Meng, D. Geng, M. N. Banis, R. Li, S. Ye, S. Knights, G. A. Botton, T.-K. Sham, X. Sun, *Sci. Rep.* **2013**, *3*, 1775.
[166] J. Liu, M. Jiao, L. Lu, H. M. Barkholtz, Y. Li, Y. Wang, L. Jiang, Z. Wu, D.-j. Liu, L. Zhuang, C. Ma, J. Zeng, B. Zhang, D. Su, P. Song, W. Xing, W. Xu, Y. Wang, Z. Jiang, G. Sun, *Nat. Commun.* **2017**, *8*, 15938.
[167] Z. Geng, Y. Liu, X. Kong, P. Li, K. Li, Z. Liu, J. Du, M. Shu, R. Si, J. Zeng, *Adv. Mater.* **2018**, *30*, 1803498.
[168] W. Sun, L. Du, Q. Tan, J. Zhou, Y. Hu, C. Du, Y. Gao, G. Yin, *ACS Appl. Mater. Interfaces* **2019**, *11*, 41258.
[169] D. Wang, L. Xiao, P. Yang, Z. Xu, X. Lu, L. Du, O. Levin, L. Ge, X. Pan, J. Zhang, M. An, *J. Mater. Chem. A* **2019**, *7*, 11007.
[170] E. Proietti, F. Jaouen, M. Lefevre, N. Larouche, J. Tian, J. Herranz, J. P. Dodelet, *Nat. Commun.* **2011**, *2*, 416.
[171] M. Lefevre, E. Proietti, F. Jaouen, J. P. Dodelet, *Science* **2009**, *324*, 71.
[172] G. Zhang, R. Chenitz, M. Lefèvre, S. Sun, J.-P. Dodelet, *Nano Energy* **2016**, *29*, 111.
[173] H. T. Chung, D. A. Cullen, D. Higgins, B. T. Sneed, E. F. Holby, K. L. More, P. Zelenay, *Science* **2017**, *357*, 479.
[174] H. Yang, Q. Lin, C. Zhang, X. Yu, Z. Cheng, G. Li, Q. Hu, X. Ren, Q. Zhang, J. Liu, C. He, *Nat. Commun.* **2020**, *11*, 593.
[175] L. Du, L. Xing, G. Zhang, S. Sun, *Carbon* **2019**, *156*, 77.
[176] F. Kong, M. Norouzi Banis, L. Du, L. Zhang, L. Zhang, J. Li, K. Doyle-Davis, J. Liang, Q. Liu, X. Yang, R. Li, C. Du, G. Yin, X. Sun, *J. Mater. Chem. A* **2019**, *7*, 24830.
[177] Z. Su, J. Liu, M. Li, Y. Zhu, S. Qian, M. Weng, J. Zheng, Y. Zhong, F. Pan, S. Zhang, *Electrochem. Energy Rev.* **2020**, *3*, 286.
[178] S. Sun, F. Jaouen, J.-P. Dodelet, *Adv. Mater.* **2008**, *20*, 3900.
[179] S. Guo, D. Li, H. Zhu, S. Zhang, N. M. Markovic, V. R. Stamenkovic, S. Sun, *Angew. Chem., Int. Ed.* **2013**, *52*, 3465.
[180] W. Hong, C. Shang, J. Wang, E. Wang, *Energy Environ. Sci.* **2015**, *8*, 2910.
[181] H. B. Lee, S. H. Baeck, T. F. Jaramillo, S. F. Bent, *Nano Lett.* **2013**, *13*, 457.
[182] S. M. Alia, B. S. Pivovar, Y. Yan, *J. Am. Chem. Soc.* **2013**, *135*, 13473.
[183] G. Zhang, S. Sun, M. Cai, Y. Zhang, R. Li, X. Sun, *Sci. Rep.* **2013**, *3*, 1526.
[184] C. W. Xu, H. Wang, P. K. Shen, S. P. Jiang, *Adv. Mater.* **2007**, *19*, 4256.
[185] D. F. van der Vliet, C. Wang, D. Tripkovic, D. Strmcnik, X. F. Zhang, M. K. Debe, R. T. Atanasoski, N. M. Markovic, V. R. Stamenkovic, *Nat. Mater.* **2012**, *11*, 1051.
[186] S. Sun, G. Zhang, Y. Zhong, H. Liu, R. Li, X. Zhou, X. Sun, *Chem. Commun.* **2009**, *45*, 7048.
[187] S. Sun, D. Yang, G. Zhang, E. Sacher, J.-P. Dodelet, *Chem. Mater.* **2007**, *19*, 6376.
[188] S. Sun, G. Zhang, D. Geng, Y. Chen, M. N. Banis, R. Li, M. Cai, X. Sun, *Chem. - Eur. J.* **2010**, *16*, 829.
[189] J. Lai, F. Lin, Y. Tang, P. Zhou, Y. Chao, Y. Zhang, S. Guo, *Adv. Energy Mater.* **2019**, *9*, 1800684.
[190] N. Han, Y. Wang, H. Yang, J. Deng, J. Wu, Y. Li, Y. Li, *Nat. Commun.* **2018**, *9*, 1320.
[191] D. Voiry, R. Fullon, J. Yang, E. S. C. de Carvalho Castro, R. Kappera, I. Bozkurt, D. Kaplan, M. J. Lagos, P. E. Batson, G. Gupta, A. D. Mohite, L. Dong, D. Er, V. B. Shenoy, T. Asefa, M. Chhowalla, *Nat. Mater.* **2016**, *15*, 1003.
[192] F. Kong, S. Liu, J. Li, L. Du, M. N. Banis, L. Zhang, G. Chen, K. Doyle-Davis, J. Liang, S. Wang, F. Zhao, R. Li, C. Du, G. Yin, Z. Zhao, X. Sun, *Nano Energy* **2019**, *64*, 103890.
[193] L. Zhang, L. T. Roling, X. Wang, M. Vara, M. Chi, J. Liu, S. I. Choi, J. Park, J. A. Herron, Z. Xie, M. Mavrikakis, Y. Xia, *Science* **2015**, *349*, 412.
[194] S. Yoo, S. Cho, D. Kim, S. Ih, S. Lee, L. Zhang, H. Li, J. Y. Lee, L. Liu, S. Park, *Nanoscale* **2019**, *11*, 2840.
[195] J. Wang, Z. Huang, W. Liu, C. Chang, H. Tang, Z. Li, W. Chen, C. Jia, T. Yao, S. Wei, Y. Wu, Y. Li, *J. Am. Chem. Soc.* **2017**, *139*, 17281.
[196] L. Shang, H. Yu, X. Huang, T. Bian, R. Shi, Y. Zhao, G. I. Waterhouse, L. Z. Wu, C. H. Tung, T. Zhang, *Adv. Mater.* **2016**, *28*, 1668.
[197] H. Zhou, F. Yu, Y. Huang, J. Sun, Z. Zhu, R. J. Nielsen, R. He, J. Bao, W. A. Goddard III, S. Chen, Z. Ren, *Nat. Commun.* **2016**, *7*, 12765.
[198] Q. Wei, X. Yang, G. Zhang, D. Wang, L. Zuin, D. Banham, L. Yang, S. Ye, Y. Wang, M. Mohamedi, S. Sun, *Appl. Catal., B* **2018**, *237*, 85.
[199] Q. Wei, G. Zhang, X. Yang, Y. Fu, G. Yang, N. Chen, W. Chen, S. Sun, *J. Mater. Chem. A* **2018**, *6*, 4605.
[200] X. Yang, Y. Wang, G. Zhang, L. Du, L. Yang, M. Markiewicz, J.-y. Choi, C. Régis, S. Sun, *Appl. Catal., B* **2020**, *264*, 118523.
[201] R. Wang, J. Yan, M. Zu, S. Yang, X. Cai, Q. Gao, Y. Fang, S. Zhang, S. Zhang, *Electrochim. Acta* **2018**, *279*, 74.
[202] Y. Mi, L. Wen, Z. Wang, D. Cao, R. Xu, Y. Fang, Y. Zhou, Y. Lei, *Nano Energy* **2016**, *30*, 109.
[203] D. Li, H. Zhao, L. Li, B. Mao, M. Chen, H. Shen, W. Shi, D. Jiang, Y. Lei, *Adv. Funct. Mater.* **2018**, *28*, 1806284.
[204] S. Zhang, H. Zhao, D. Jiang, R. John, *Anal. Chim. Acta* **2004**, *514*, 89.
[205] Y. Han, S. Zhang, H. Zhao, W. Wen, H. Zhang, H. Wang, F. Peng, *Langmuir* **2010**, *26*, 6033.
[206] D. Chi, S. D. Lu, R. Xu, K. Liu, D. W. Cao, L. Y. Wen, Y. Mi, Z. J. Wang, Y. Lei, S. C. Qu, Z. G. Wang, *Nanoscale* **2015**, *7*, 15251.
[207] Y. Yan, M. Han, A. Konkin, T. Koppe, D. Wang, T. Andreu, G. Chen, U. Vetter, J. R. Morante, P. Schaaf, *J. Mater. Chem. A* **2014**, *2*, 12708.
[208] G. Wang, H. Wang, Y. Ling, Y. Tang, X. Yang, R. C. Fitzmorris, C. Wang, J. Z. Zhang, Y. Li, *Nano Lett.* **2011**, *11*, 3026.
[209] J. H. Park, S. Kim, A. J. Bard, *Nano Lett.* **2006**, *6*, 24.
[210] R. Wang, S. Chen, Y. H. Ng, Q. Gao, S. Yang, S. Zhang, F. Peng, Y. Fang, S. Zhang, *Chem. Eng. J.* **2019**, *362*, 658.
[211] X. She, J. Wu, H. Xu, J. Zhong, Y. Wang, Y. Song, K. Nie, Y. Liu, Y. Yang, M.-T. F. Rodrigues, R. Vajtai, J. Lou, D. Du, H. Li, P. M. Ajayan, *Adv. Energy Mater.* **2017**, *7*, 1700025.
[212] M. Zhou, J. Bao, Y. Xu, J. Zhang, J. Xie, M. Guan, C. Wang, L. Wen, Y. Lei, Y. Xie, *ACS Nano* **2014**, *8*, 7088.
[213] S. C. Warren, E. Thimsen, *Energy Environ. Sci.* **2012**, *5*, 5133.
[214] H. J. Kim, S. H. Lee, A. A. Upadhye, I. Ro, M. I. Tejedor-Tejedor, M. A. Anderson, W. B. Kim, G. W. Huber, *ACS Nano* **2014**, *8*, 10756.
[215] Z. Zhan, R. Xu, Y. Mi, H. Zhao, Y. Lei, *ACS Nano* **2015**, *9*, 4583.

[216] Z. Wang, D. Cao, L. Wen, R. Xu, M. Obergfell, Y. Mi, Z. Zhan, N. Nasori, J. Demsar, Y. Lei, *Nat. Commun.* **2016**, *7*, 10348.
[217] L. Wen, R. Xu, C. Cui, W. Tang, Y. Mi, X. Lu, Z. Zeng, S. L. Suib, P. X. Gao, Y. Lei, *Nano Lett.* **2018**, *18*, 4914.
[218] Y. Sun, N. Liu, Y. Cui, *Nat. Energy* **2016**, *1*, 16071.
[219] N. Mahmood, T. Tang, Y. Hou, *Adv. Energy Mater.* **2016**, *6*, 1600374.
[220] F. Cheng, J. Liang, Z. Tao, J. Chen, *Adv. Mater.* **2011**, *23*, 1695.
[221] H. K. Liu, G. X. Wang, Z. Guo, J. Wang, K. Konstantinov, *J. Nanosci. Nanotechnol.* **2006**, *6*, 1.
[222] J. Mei, T. Liao, Z. Sun, *J. Energy Chem.* **2018**, *27*, 117.
[223] Z. Q. Duan, Y. T. Liu, X. M. Xie, X. Y. Ye, X. D. Zhu, *Chem. - Asian J.* **2016**, *11*, 828.
[224] N. S. Hieu, J. C. Lim, J. K. Lee, *Microelectron. Eng.* **2012**, *89*, 138.
[225] G. Xu, B. Ding, P. Nie, L. Shen, H. Dou, X. Zhang, *ACS Appl. Mater. Interfaces* **2014**, *6*, 194.
[226] D. Li, L. Chen, T. Wang, L.-Z. Fan, *ACS Appl. Mater. Interfaces* **2018**, *10*, 7069.
[227] X. Lai, J. E. Halpert, D. Wang, *Energy Environ. Sci.* **2012**, *5*, 5604.
[228] G.-Y. Zhao, H.-L. Li, *Microporous Mesoporous Mater.* **2008**, *110*, 590.
[229] W. Xue, Q.-B. Yan, G. Xu, L. Suo, Y. Chen, C. Wang, C.-A. Wang, J. Li, *Nano Energy* **2017**, *38*, 12.
[230] Q. Chen, Y. Zhao, X. Huang, N. Chen, L. Qu, *J. Mater. Chem. A* **2015**, *3*, 6761.
[231] E. Pomerantseva, F. Bonaccorso, X. Feng, Y. Cui, Y. Gogotsi, *Science* **2019**, *366*, eaan8285.
[232] H. Wang, Q. Gao, L. Jiang, *Small* **2011**, *7*, 2454.
[233] G. Xu, B. Ding, L. Shen, P. Nie, J. Han, X. Zhang, *J. Mater. Chem. A* **2013**, *1*, 4490.
[234] M. Yu, W. Qiu, F. Wang, T. Zhai, P. Fang, X. Lu, Y. Tong, *J. Mater. Chem. A* **2015**, *3*, 15792.
[235] J. Yang, W. Liu, H. Niu, K. Cheng, K. Ye, K. Zhu, G. Wang, D. Cao, J. Yan, *Nano Res.* **2018**, *11*, 4744.
[236] F. Xia, S. B. Kim, H. Cheng, J. M. Lee, T. Song, Y. Huang, J. A. Rogers, U. Paik, W. I. Park, *Nano Lett.* **2013**, *13*, 3340.
[237] K. Yan, H.-W. Lee, T. Gao, G. Zheng, H. Yao, H. Wang, Z. Lu, Y. Zhou, Z. Liang, Z. Liu, *Nano Lett.* **2014**, *14*, 6016.
[238] T. Jin, Q. Han, Y. Wang, L. Jiao, *Small* **2018**, *14*, 1703086.
[239] R. Mas-Balleste, C. Gomez-Navarro, J. Gomez-Herrero, F. Zamora, *Nanoscale* **2011**, *3*, 20.
[240] J. Xie, J. Wang, H. R. Lee, K. Yan, Y. Li, F. Shi, W. Huang, A. Pei, G. Chen, R. Subbaraman, *Sci. Adv.* **2018**, *4*, eaat5168.
[241] A. Magasinski, P. Dixon, B. Hertzberg, A. Kvit, J. Ayala, G. Yushin, *Nat. Mater.* **2010**, *9*, 353.
[242] P.-Y. Yang, S.-P. Ju, Z.-M. Lai, J.-Y. Hsieh, J.-S. Lin, *RSC Adv.* **2016**, *6*, 105713.
[243] S. J. An, J. Li, C. Daniel, D. Mohanty, S. Nagpure, D. L. Wood, *Carbon* **2016**, *105*, 52.
[244] S. Ramesh, K. Karuppasamy, H.-S. Kim, H. S. Kim, J.-H. Kim, *Sci. Rep.* **2018**, *8*, 16543.
[245] O. Riedel, A. Düttmann, S. Dühnen, J. Kolny-Olesiak, C. Gutsche, J. Parisi, M. Winter, M. Knipper, T. Placke, *ACS Appl. Nano Mater.* **2019**, *2*, 3577.
[246] T. Song, L. Hu, U. Paik, *J. Phys. Chem. Lett.* **2014**, *5*, 720.
[247] S. R. Kwon, J. Harris, T. Zhou, D. Loufakis, J. G. Boyd, J. L. Lutkenhaus, *ACS Nano* **2017**, *11*, 6682.
[248] M. Singh, J. Kaiser, H. Hahn, *J. Electrochem. Soc.* **2015**, *162*, A1196.
[249] Z. Sun, T. Liao, L. Kou, *Sci. China Mater.* **2017**, *60*, 1.
[250] B. Wang, X. Li, T. Qiu, B. Luo, J. Ning, J. Li, X. Zhang, M. Liang, L. Zhi, *Nano Lett.* **2013**, *13*, 5578.
[251] J. Zhu, D. Deng, *Chem. Eng. Sci.* **2016**, *154*, 54.
[252] Q. Li, J. Chen, L. Fan, X. Kong, Y. Lu, *Green Energy Environ.* **2016**, *1*, 18.
[253] H. Liu, X. Liu, W. Li, X. Guo, Y. Wang, G. Wang, D. Zhao, *Adv. Energy Mater.* **2017**, *7*, 1700283.
[254] M. Obrovac, V. Chevrier, *Chem. Rev.* **2014**, *114*, 11444.
[255] M. R. Palacin, *Chem. Soc. Rev.* **2009**, *38*, 2565.
[256] R. Marom, S. F. Amalraj, N. Leifer, D. Jacob, D. Aurbach, *J. Mater. Chem.* **2011**, *21*, 9938.
[257] C. de las Casas, W. Li, *J. Power Sources* **2012**, *208*, 74.
[258] I. Lahiri, W. Choi, *Crit. Rev. Solid State Mater. Sci.* **2013**, *38*, 128.
[259] B. J. Landi, M. J. Ganter, C. D. Cress, R. A. DiLeo, R. P. Raffaelle, *Energy Environ. Sci.* **2009**, *2*, 638.
[260] M. Liang, L. Zhi, *J. Mater. Chem.* **2009**, *19*, 5871.
[261] M. Liu, P. Zhang, Z. Qu, Y. Yan, C. Lai, T. Liu, S. Zhang, *Nat. Commun.* **2019**, *10*, 3917.
[262] X. Gu, S. Zhang, Y. Hou, *Chin. J. Chem.* **2016**, *34*, 13.
[263] J. Ji, J. Liu, L. Lai, X. Zhao, Y. Zhen, J. Lin, Y. Zhu, H. Ji, L. L. Zhang, R. S. Ruoff, *ACS Nano* **2015**, *9*, 8609.
[264] C. Zhang, N. Mahmood, H. Yin, F. Liu, Y. Hou, *Adv. Mater.* **2013**, *25*, 4932.
[265] Y. Xu, C. Zhang, M. Zhou, Q. Fu, C. Zhao, M. Wu, Y. Lei, *Nat. Commun.* **2018**, *9*, 1720.
[266] J. Wu, Z. Pan, Y. Zhang, B. Wang, H. Peng, *J. Mater. Chem. A* **2018**, *6*, 12932.
[267] Q. Wei, Y. Fu, G. Zhang, Y. Wang, X. Wang, M. Mohamedi, S. Sun, *RSC Adv.* **2016**, *6*, 84149.
[268] S. Li, J. Qiu, C. Lai, M. Ling, H. Zhao, S. Zhang, *Nano Energy* **2015**, *12*, 224.
[269] X. Gu, C. Lai, F. Liu, W. Yang, Y. Hou, S. Zhang, *J. Mater. Chem. A* **2015**, *3*, 9502.
[270] X. Gu, C.-j. Tong, C. Lai, J. Qiu, X. Huang, W. Yang, B. Wen, L.-m. Liu, Y. Hou, S. Zhang, *J. Mater. Chem. A* **2015**, *3*, 16670.
[271] D. Adekoya, X. Gu, M. Rudge, W. Wen, C. Lai, M. Hankel, S. Zhang, *Adv. Funct. Mater.* **2018**, *28*, 1803972.
[272] L. Liang, Y. Xu, Y. Li, H. Dong, M. Zhou, H. Zhao, U. Kaiser, Y. Lei, *J. Mater. Chem. A* **2017**, *5*, 1749.
[273] L. Liang, Y. Xu, L. Wen, Y. Li, M. Zhou, C. Wang, H. Zhao, U. Kaiser, Y. Lei, *Nano Res.* **2017**, *10*, 3189.
[274] J. Qiu, S. Li, X. Su, Y. Wang, L. Xu, S. Yuan, H. Li, S. Zhang, *Chem. Eng. J.* **2017**, *320*, 300.
[275] H. Jin, H. Lu, W. Wu, S. Chen, T. Liu, X. Bi, W. Xie, X. Chen, K. Yang, J. Li, A. Liu, Y. Lei, J. Wang, S. Wang, J. Lu, *Nano Energy* **2020**, *70*, 104569.
[276] C. Yan, H. Zhao, J. Li, H. Jin, L. Liu, W. Wu, J. Wang, Y. Lei, S. Wang, *Small* **2020**, *16*, 1907141.
[277] Y. Zhang, B. Liu, T. Borjigin, S. Xia, X. Yang, S. Sun, H. Guo, *J. Power Sources* **2020**, *450*, 227696.
[278] Y. Wang, J. Han, X. Gu, S. Dimitrijev, Y. Hou, S. Zhang, *J. Mater. Chem. A* **2017**, *5*, 18737.
[279] L. Xu, Y. Tian, T. Liu, H. Li, J. Qiu, S. Li, H. Li, S. Yuan, S. Zhang, *Green Energy Environ.* **2018**, *3*, 156.
[280] J. Liu, Y. Li, H. Fan, Z. Zhu, J. Jiang, R. Ding, Y. Hu, X. Huang, *Chem. Mater.* **2010**, *22*, 212.
[281] J. S. Chen, T. Zhu, X. H. Yang, H. G. Yang, X. W. Lou, *J. Am. Chem. Soc.* **2010**, *132*, 13162.
[282] M. V. Reddy, T. Yu, C. H. Sow, Z. X. Shen, C. T. Lim, G. V. Subba Rao, B. V. R. Chowdari, *Adv. Funct. Mater.* **2007**, *17*, 2792.
[283] B. Koo, H. Xiong, M. D. Slater, V. B. Prakapenka, M. Balasubramanian, P. Podsiadlo, C. S. Johnson, T. Rajh, E. V. Shevchenko, *Nano Lett.* **2012**, *12*, 2429.
[284] X. W. Lou, D. Deng, J. Y. Lee, J. Feng, L. A. Archer, *Adv. Mater.* **2008**, *20*, 258.
[285] X. W. Lou, D. Deng, J. Y. Lee, L. A. Archer, *J. Mater. Chem.* **2008**, *18*, 4397.
[286] L. Tian, H. Zou, J. Fu, X. Yang, Y. Wang, H. Guo, X. Fu, C. Liang, M. Wu, P. K. Shen, Q. Gao, *Adv. Funct. Mater.* **2010**, *20*, 617.
[287] F. Zhan, B. Geng, Y. Guo, *Chem. - Eur. J.* **2009**, *15*, 6169.
[288] X. Wang, X.-L. Wu, Y.-G. Guo, Y. Zhong, X. Cao, Y. Ma, J. Yao, *Adv. Funct. Mater.* **2010**, *20*, 1680.
[289] X. Wang, L. Yu, X.-L. Wu, F. Yuan, Y.-G. Guo, Y. Ma, J. Yao, *J. Phys. Chem. C* **2009**, *113*, 15553.

[290] Y. Xu, M. Zhou, L. Wen, C. Wang, H. Zhao, Y. Mi, L. Liang, Q. Fu, M. Wu, Y. Lei, *Chem. Mater.* **2015**, *27*, 4274.
[291] L. Liang, Y. Xu, C. Wang, L. Wen, Y. Fang, Y. Mi, M. Zhou, H. Zhao, Y. Lei, *Energy Environ. Sci.* **2015**, *8*, 2954.
[292] C. Wang, L. Zhang, M. Al-Mamun, Y. Dou, P. Liu, D. Su, G. Wang, S. Zhang, D. Wang, H. Zhao, *Adv. Energy Mater.* **2019**, *9*, 1900909.
[293] Y. Fu, Q. Wei, X. Wang, G. Zhang, H. Shu, X. Yang, A. C. Tavares, S. Sun, *RSC Adv.* **2016**, *6*, 16624.
[294] Y. Yang, Q. Fu, H. Zhao, Y. Mi, W. Li, Y. Dong, M. Wu, Y. Lei, *J. Alloys Compd.* **2018**, *769*, 257.
[295] P. Zhang, J. Qiu, Z. Zheng, G. Liu, M. Ling, W. Martens, H. Wang, H. Zhao, S. Zhang, *Electrochim. Acta* **2013**, *104*, 41.
[296] D. Cai, D. Li, S. Wang, X. Zhu, W. Yang, S. Zhang, H. Wang, *J. Alloys Compd.* **2013**, *561*, 54.
[297] Y. Fu, Q. Wei, B. Lu, X. Wang, S. Sun, *J. Alloys Compd.* **2016**, *684*, 419.
[298] Y. Huang, H. Yang, T. Xiong, D. Adekoya, W. Qiu, Z. Wang, S. Zhang, M. S. Balogun, *Energy Storage Mater.* **2020**, *25*, 41.
[299] Y. Xu, M. Zhou, X. Wang, C. Wang, L. Liang, F. Grote, M. Wu, Y. Mi, Y. Lei, *Angew. Chem., Int. Ed.* **2015**, *54*, 8768.
[300] X. Gu, C.-j. Tong, B. Wen, L.-m. Liu, C. Lai, S. Zhang, *Electrochim. Acta* **2016**, *196*, 369.
[301] Y. Fu, Q. Wei, X. Wang, H. Shu, X. Yang, S. Sun, *J. Mater. Chem. A* **2015**, *3*, 13807.
[302] K. C. Klavetter, J. Pedro de Souza, A. Heller, C. B. Mullins, *J. Mater. Chem. A* **2015**, *3*, 5829.
[303] H.-K. Seong, M.-H. Kim, H.-J. Choi, Y.-J. Choi, J.-G. Park, *Metals Mater. Int.* **2008**, *14*, 477.
[304] M.-H. Park, M. G. Kim, J. Joo, K. Kim, J. Kim, S. Ahn, Y. Cui, J. Cho, *Nano Lett.* **2009**, *9*, 3844.
[305] Y. Zhao, X. Liu, H. Li, T. Zhai, H. Zhou, *Chem. Commun.* **2012**, *48*, 5079.
[306] X. Huang, J. Yang, S. Mao, J. Chang, P. B. Hallac, C. R. Fell, B. Metz, J. Jiang, P. T. Hurley, J. Chen, *Adv. Mater.* **2014**, *26*, 4326.
[307] P. Castrucci, M. Diociaiuti, C. M. Tank, S. Casciardi, F. Tombolini, M. Scarselli, M. De Crescenzi, V. L. Mathe, S. V. Bhoraskar, *Nanoscale* **2012**, *4*, 5195.
[308] Y. Yao, M. T. McDowell, I. Ryu, H. Wu, N. Liu, L. Hu, W. D. Nix, Y. Cui, *Nano Lett.* **2011**, *11*, 2949.
[309] S. Chen, Z. Chen, X. Xu, C. Cao, M. Xia, Y. Luo, *Small* **2018**, *14*, 1703361.
[310] S. R. Gowda, V. Pushparaj, S. Herle, G. Girishkumar, J. G. Gordon, H. Gullapalli, X. Zhan, P. M. Ajayan, A. L. M. Reddy, *Nano Lett.* **2012**, *12*, 6060.
[311] X. Zuo, J. Zhu, P. Müller-Buschbaum, Y.-J. Cheng, *Nano Energy* **2017**, *31*, 113.
[312] T. Liu, Q. Chu, C. Yan, S. Zhang, Z. Lin, J. Lu, *Adv. Energy Mater.* **2019**, *9*, 1802645.
[313] C. Wang, H. Wu, Z. Chen, M. T. McDowell, Y. Cui, Z. Bao, *Nat. Chem.* **2013**, *5*, 1042.
[314] H. Wu, G. Zheng, N. Liu, T. J. Carney, Y. Yang, Y. Cui, *Nano Lett.* **2012**, *12*, 904.
[315] J. Wang, H. Tang, H. Wang, R. Yu, D. Wang, *Mater. Chem. Front.* **2017**, *1*, 414.
[316] L. Zhang, R. Rajagopalan, H. Guo, X. Hu, S. Dou, H. Liu, *Adv. Funct. Mater.* **2016**, *26*, 440.
[317] T. Yang, X. Tian, X. Li, K. Wang, Z. Liu, Q. Guo, Y. Song, *Chem. - Eur. J.* **2017**, *23*, 2165.
[318] M. Ko, S. Chae, S. Jeong, P. Oh, J. Cho, *ACS Nano* **2014**, *8*, 8591.
[319] T. H. Hwang, Y. M. Lee, B.-S. Kong, J.-S. Seo, J. W. Choi, *Nano Lett.* **2012**, *12*, 802.
[320] H.-C. Tao, L.-Z. Fan, X. Qu, *Electrochim. Acta* **2012**, *71*, 194.
[321] Z. Lu, T. Wong, T.-W. Ng, C. Wang, *RSC Adv.* **2014**, *4*, 2440.
[322] H. Tao, L.-Z. Fan, W.-L. Song, M. Wu, X. He, X. Qu, *Nanoscale* **2014**, *6*, 3138.
[323] N. Liu, Z. Lu, J. Zhao, M. T. McDowell, H.-W. Lee, W. Zhao, Y. Cui, *Nat. Nanotechnol.* **2014**, *9*, 187.
[324] L. Zhang, C. Wang, Y. Dou, N. Cheng, D. Cui, Y. Du, P. Liu, M. Al-Mamun, S. Zhang, H. Zhao, *Angew. Chem., Int. Ed.* **2019**, *58*, 8824.
[325] J. Zhang, G. Zhang, T. Zhou, S. Sun, *Adv. Funct. Mater.* **2020**, *30*, 1910000.
[326] L. Liu, H. Zhao, Y. Lei, *Small Methods* **2019**, *3*, 1800341.
[327] Y. Zhang, Z. Shang, M. Shen, S. P. Chowdhury, A. Ignaszak, S. Sun, Y. Ni, *ACS Sustainable Chem. Eng.* **2019**, *7*, 11175.
[328] K. H. An, W. S. Kim, Y. S. Park, J.-M. Moon, D. J. Bae, S. C. Lim, Y. S. Lee, Y. H. Lee, *Adv. Funct. Mater.* **2001**, *11*, 387.
[329] W. Lu, L. Qu, K. Henry, L. Dai, *J. Power Sources* **2009**, *189*, 1270.
[330] H. Jiang, T. Zhao, C. Li, J. Ma, *Chem. Commun.* **2011**, *47*, 8590.
[331] F. Du, D. Yu, L. Dai, S. Ganguli, V. Varshney, A. K. Roy, *Chem. Mater.* **2011**, *23*, 4810.
[332] B. G. Choi, M. Yang, W. H. Hong, J. W. Choi, Y. S. Huh, *ACS Nano* **2012**, *6*, 4020.
[333] D. Yu, K. Goh, H. Wang, L. Wei, W. Jiang, Q. Zhang, L. Dai, Y. Chen, *Nat. Nanotechnol.* **2014**, *9*, 555.
[334] Z. Fan, J. Yan, L. Zhi, Q. Zhang, T. Wei, J. Feng, M. Zhang, W. Qian, F. Wei, *Adv. Mater.* **2010**, *22*, 3723.
[335] J. Xu, K. Wang, S.-Z. Zu, B.-H. Han, Z. Wei, *ACS Nano* **2010**, *4*, 5019.
[336] Y. Gao, Y. Zhang, Y. Zhang, L. Xie, X. Li, F. Su, X. Wei, Z. Xu, C. Chen, R. Cai, *J. Energy Chem.* **2016**, *25*, 49.
[337] M. Zhi, S. Lee, N. Miller, N. H. Menzler, N. Wu, *Energy Environ. Sci.* **2012**, *5*, 7066.
[338] W. Li, X. Wang, Y. Hu, L. Sun, C. Gao, C. Zhang, H. Liu, M. Duan, *Nanoscale Res. Lett.* **2018**, *13*, 120.
[339] J. Zhao, Y. Cheng, X. Yan, D. Sun, F. Zhu, Q. Xue, *CrystEngComm* **2012**, *14*, 5879.
[340] H. Jiang, J. Ma, C. Li, *Chem. Commun.* **2012**, *48*, 4465.
[341] H. Zhao, C. Wang, R. Vellacheri, M. Zhou, Y. Xu, Q. Fu, M. Wu, F. Grote, Y. Lei, *Adv. Mater.* **2014**, *26*, 7654.
[342] F. Grote, Y. Lei, *Nano Energy* **2014**, *10*, 63.
[343] L. Wen, Y. Mi, C. Wang, Y. Fang, F. Grote, H. Zhao, M. Zhou, Y. Lei, *Small* **2014**, *10*, 3162.
[344] Z. Lei, L. Liu, H. Zhao, F. Liang, S. Chang, L. Li, Y. Zhang, Z. Lin, J. Kröger, Y. Lei, *Nat. Commun.* **2020**, *11*, 299.
[345] L. Du, L. Xing, G. Zhang, M. Dubois, S. Sun, *Small Methods* **2020**, *4*, 2000016.
[346] L. Osmieri, R. K. Ahluwalia, X. Wang, H. T. Chung, X. Yin, A. J. Kropf, J. Park, D. A. Cullen, K. L. More, P. Zelenay, D. J. Myers, K. C. Neyerlin, *Appl. Catal., B* **2019**, *257*, 117929.
[347] C. Wang, L. Luo, Y. Shao, *Microsc. Microanal.* **2018**, *24*, 1876.
[348] L. Huang, J.-Y. Sun, S.-H. Cao, M. Zhan, Z.-R. Ni, H.-J. Sun, Z. Chen, Z.-Y. Zhou, E. G. Sorte, Y. J. Tong, S.-G. Sun, *ACS Catal.* **2016**, *6*, 7686.
[349] H. L. Wu, L. A. Huff, A. A. Gewirth, *ACS Appl. Mater. Interfaces* **2015**, *7*, 1709.
[350] X. Liu, A. Wang, L. Li, T. Zhang, C.-Y. Mou, J.-F. Lee, *J. Catal.* **2011**, *278*, 288.
[351] C. Cremers, T. Jurzinsky, J. Meier, A. Schade, M. Branghofer, K. Pinkwart, J. Tübke, *J. Electrochem. Soc.* **2018**, *165*, F3307.
[352] L. Du, V. Prabhakaran, X. Xie, S. Park, Y. Wang, Y. Shao, *Adv. Mater.* **2020**, 1908232. https://doi.org/10.1002/adma.201908232.
[353] G. Zhang, X. Yang, M. Dubois, M. Herraiz, R. Chenitz, M. Lefèvre, M. Cherif, F. Vidal, V. Glibin, S. Sun, J.-P. Dodelet, *Energy Environ. Sci.* **2019**, *12*, 3015.
[354] L. Du, L. Luo, Z. Feng, M. Engelhard, X. Xie, B. Han, J. Sun, J. Zhang, G. Yin, C. Wang, Y. Wang, Y. Shao, *Nano Energy* **2017**, *39*, 245.
[355] R. Chenitz, U. I. Kramm, M. Lefèvre, V. Glibin, G. Zhang, S. Sun, J.-P. Dodelet, *Energy Environ. Sci.* **2018**, *11*, 365.
[356] V. P. Glibin, M. Cherif, F. Vidal, J.-P. Dodelet, G. Zhang, S. Sun, *J. Electrochem. Soc.* **2019**, *166*, F3277.
[357] J. Meng, H. Guo, C. Niu, Y. Zhao, L. Xu, Q. Li, L. Mai, *Joule* **2017**, *1*, 522.